

UNIVERSIDADE DE SÃO PAULO
INSTITUTO DE FÍSICA

Estimativa de dose nos pulmões para procedimentos de tomografia computadorizada

Juliana Cristina Martins

Orientador: Prof. Dr. Paulo Roberto Costa

Dissertação de mestrado apresentada ao Instituto
de Física para a obtenção do título de Mestre em
Ciências

Banca Examinadora:

Prof. Dr. Paulo Roberto Costa (IFUSP - orientador)

Prof. Dr. Vito Roberto Vanin (IFUSP)

Prof. Dr. Marcelo Baptista de Freitas (UNIFESP)

São Paulo

2015

FICHA CATALOGRÁFICA
Preparada pelo Serviço de Biblioteca e Informação
do Instituto de Física da Universidade de São Paulo

Martins, Juliana Cristina

Lung dose estimates for computed tomography procedures : Estimativa de dose nos pulmões para procedimentos de tomografia computadorizada. São Paulo, 2015.

Dissertação (Mestrado) – Universidade de São Paulo. Instituto de Física. Depto. de Física Nuclear.

Orientador: Prof. Dr. Paulo Roberto Costa

Área de Concentração: Física Médica

Unitermos: 1. Tomografia computadorizada por raios X; 2. Radiologia; 3. Física médica; 4. Dosimetria termoluminescente.

USP/IF/SBI-130/2015

UNIVERSITY OF SÃO PAULO
INSTITUTE OF PHYSICS

Lung dose estimates for computed tomography procedures

Juliana Cristina Martins

Advisor: Prof. Dr. Paulo Roberto Costa

Dissertation submitted to the Institute of Physics of
the University of São Paulo for the Master of
Science degree.

Examination Committee:

Prof. Dr. Paulo Roberto Costa (IFUSP - Advisor)

Prof. Dr. Vito Roberto Vanin (IFUSP)

Prof. Dr. Marcelo Baptista de Freitas (UNIFESP)

São Paulo

2015

To my parentes Rosane and Valdeir for supporting me with everything, especially love. For my fiancé Henrique who always stood by my side. To my friends for all the patience.

“Only one who devotes himself to a cause with his whole strength and soul can be a true master. For this reason mastery demands all of a person.”

Albert Einstein

ACKNOWLEDGMENTS

In the first place I want to thank God for giving me the strength and capacity to overcome challenges and go further.

I deeply thank my parents Rosane and Valdeir for all the love, support and comprehension during my entire life, especially when I decided to move to São Paulo.

I want to thank my beloved fiancé Henrique, for loving me in every moment of happiness and joy but mainly for loving me in each moment of difficulty.

I thank my brother Rafael for encouragement and partnership in the so desired times of relaxation.

I deeply thank my advisor Paulo for accepting me and for putting so much faith in me. I also thank Paulo for the understanding, patient and orientation.

I want to thank Dr. Elly Castellano and Prof. Dr. Michael McNitt-Gray for performing the Monte Carlo calculations used in the present project and by clarifications regarding the comparison of Monte Carlo and experimental results.

I want to thank prof. Beth, prof. Emico and prof. Ana Regina for all their kindness.

I specially thank Denise for all the times she helped me and for all the times she calmed me down in desperate times.

I want to thank Nancy for the numerous time she helped me with Riso measurements.

I want to thank Mr. Marcos Santos de Souza and all the workers from the mechanical workshop from the Institute of Physics for manufacturing the TLD holders with perfection.

I want to thank the secretariats from the Nuclear Physics Department for all their help during those years, specially Gilda for being always so kind and gentle.

I thank FAPESP for supporting me during two years under project 2013/09596-3.

I thank ICESP and InRad for allowing me to use their facilities in the development of my work.

I thank Daniel Vieira and Thamiris for the support during experimental measurements in the hospital, and for carrying Felipe everywhere with me. I also thank Daniel for the countless times he helped me with statistical problems.

I thank Josilene for her partnership in the amazing trips to Italy and Canada, for the adventures and for the laughs we shared. I also thank Josilene for answering numerous questions regarding radiation physics.

I thank Daniel Cruz for all the rides he gave me when it was already late to go home alone.

I thank Felisberto and Leandro for all the lunches and dinners at the IF university restaurant, for introducing me to good friends and for being always available to talk and to listen.

I thank my friends Leonardo, Júlio, Daniel, Bruna and Eduardo for the friendship, for the partnership, for the support and for the good moments we lived together thanks to Renatinha.

I want to thank Taisi, Juliana Peters, Mariana and Micaela for being the best family one can have outside home.

I want to thank Lucas, my friend since graduation, for welcoming me in São Paulo, for fixing the shower at my apartment and for all the other times he was available for helping me.

I deeply thank my dearest friends Simone, Amanda and Bárbara (and many others) for understanding my absence and for being always available for me.

CONTENTS

LIST OF FIGURES.....	XI
LIST OF TABLES	XV
ACRONYMS	XVII
ABSTRACT	XIX
RESUMO	XX
INTRODUCTION	19
1. THEORY	22
1.1. A BRIEF HISTORY OF CT	22
1.1.1. <i>The Seventies – from Head to Whole Body Scanning</i>	23
1.1.2. <i>The Eighties – Fast Scanning of Single Slices</i>	25
1.1.3. <i>The Nineties – Fast Volume Scanning</i>	25
1.1.4. <i>The 2000s – Diversity and Even Faster Volume Scanning</i>	26
1.1.5. <i>The 2010s – The decade of Dose Reduction</i>	26
1.2. COMPUTED TOMOGRAPHY SCANNERS.....	27
1.2.1. <i>X-ray Tube</i>	27
1.2.2. <i>Detectors</i>	29
1.2.3. <i>Filters</i>	30
1.2.4. <i>Gantry and Patient Couch</i>	31
1.2.5. <i>Generator</i>	33
1.3. CT ACQUISITION MODES.....	33
1.3.1. <i>Scan Projection Radiograph (SPR)</i>	34
1.3.2. <i>Axial CT</i>	35
1.3.3. <i>Spiral or Helical CT</i>	35
1.3.4. <i>Mustislice CT and Cone Beam CT</i>	37
1.4. IMAGING	39
1.4.1. <i>Hounsfield Unit</i>	45
1.5. CT DOSIMETRY.....	46
1.5.1. <i>Size Specific Dose Estimates (SSDE)</i>	48
1.5.2. <i>Estimation of Organ Dose Values</i>	51
1.6. TUBE CURRENT MODULATION (TCM)	54
1.7. THERMOLUMINESCENT DOSIMETRY	56
1.8. ANTHROPOMORPHIC RANDO PHANTOM.....	58
2. MATERIALS AND METHODS.....	60

2.1.	THERMOLUMINESCENT DOSIMETERS (TLD)	60
2.1.1.	TLD Data Reading	60
2.1.2.	TLD Group Selection	61
2.1.3.	Annealing	62
2.1.4.	TLD Holders	62
2.1.5.	TLD Calibration	64
2.2.	SELECTION OF CT SCANNING PROTOCOLS	66
2.3.	LUNG DOSE ESTIMATION	66
2.4.	EFFECTIVE DIAMETER	68
2.5.	PHANTOM IRRADIATION	70
2.5.1.	Total Body Protocol	71
2.5.2.	Scan Projection Radiograph (SPR)	73
2.5.3.	Thorax Protocols	74
	Constant Tube Current	74
	Tube current modulation (TCM)	75
3.	RESULTS	76
3.1.	TLD CALIBRATION	76
3.2.	SELECTION OF CT SCANNING PROTOCOLS	77
3.3.	EFFECTIVE DIAMETER	79
3.4.	ESTIMATION OF LUNG ABSORBED DOSE	80
3.4.1.	Total Body Protocol	80
3.4.2.	Scan Projection Radiograph (SPR)	80
3.4.3.	Thorax Protocols	81
	Constant Tube Current	81
	Tube current modulation (TCM)	82
4.	DISCUSSION	84
4.1.	SELECTION OF CT SCANNING PROTOCOLS	84
4.2.	ESTIMATION OF LUNG ABSORBED DOSE	85
4.2.1.	Total Body Protocol	85
4.2.2.	Scan Projection Radiographs	86
4.2.3.	Thorax Protocols	87
	Constant mA	87
	Tube current modulation	89
4.3.	COMPARISON TO IMPACT SPREADSHEETS	91
4.4.	CORRELATION BETWEEN ORGAN DOSE AND SSDE	92

5. CONCLUSIONS	95
REFERENCES	97
ANNEXX A - Conversion factors for SSDE determination.	107
ANNEXX B - Uncertainty estimation	109

LIST OF FIGURES

Figure 1 – Historical perspective of CT scanners evolution. (a). Head scanners, which scanned the patient by translation and rotation of the measurement system with a pencil beam or (b). a small fan beam; (c). The “3 rd generation”, featuring a rotating detector, has clearly outdistanced the (d). “4 th generation”, which utilizes stationary detector rings. (source: Kalender, 2011, adapted).	24
Figure 2 - Components of a typical X-ray tube. (source: Fosbinder; Orth, 2011, adapted).	27
Figure 3 - (a). Rotating anodes spread the heat produced over a circular track, as the high energy electrons strike its surface at the so-called focal spot, creating X-ray; (b). The anode disk is made of graphite, with tungsten-rhenium deposited in one face via chemical steam process. (source: Fosbinder; Orth, 2011, adapted).	28
Figure 4 – (a). Siemens’s Straton X-ray tube and (b). Its schematics, showing the anode directly attached to the tube envelope (source: Siemens Healthcare GmbH, 2015, adapted).	29
Figure 5 – Detector arrays in modern computed tomography, in a perspective and side view. The side view shows individual detector elements coupled to photodiodes that are layered on substrate electronics, which provide power to the detector system and receive the electronic signal from the photodetector. Opaque filters are pressed into spaces between detector elements to reduce detector cross talk, however the geometric efficiency is also reduced. CT detectors are much more expensive than those used in conventional radiography. (source: Bushberg; Seibert; Leidholdt Jr; Boone, 2011).	30
Figure 6 –Without the bow tie filter, the X-ray fluence is much higher at the periphery of the field than at the center (light-green profile), since at the peripheries the attenuation path through the patient is usually thinner. The bow-tie filter reduces the X-ray intensity at the peripheries due to its format, resulting in a more homogeneous photon fluence reaching the detection system (dark-green profile). This creates the opportunity to reduce dose to the patient with no loss of image quality. (source: Bushberg; Seibert; Leidholdt Jr; Boone, 2011, adapted).	31
Figure 7 – View of the gantry without its safety housing. The gantry weighs about 1,000-2,000 kg and rotates rapidly around the patient, comprising the X-ray system (X-ray tube, collimator and filters), the detector system, the high voltage generator and mechanical supports. (source: Ulzheimer; Flohr, 2009).	32
Figure 8 – Gantry and patient couch. The gantry rotates around x-y direction and the couch translates along the z direction. (source: : ImPACT 2001).	33
Figure 9 – (a). Anterior-posterior (AP) and (b). Lateral (LAT) scan projection radiographs of the adult anthropomorphic RANDO phantom (The Phantom Laboratory, Salem, NY) used in the present work.	34
Figure 10 – (a). Axial CT, also known as sequential CT and step-and-shot CT. X-ray beam is off while the patient is being translated between consecutive acquisitions; (b). Consecutive slices are scanned until the entire scanning length is covered. (source: Bushberg; Seibert; Leidholdt Jr; Boone, 2011, adapted).	35

Figure 11 – In spiral or helical CT scanning, the X-ray tube describes a helical trajectory around the patient’s body. There is an important relationship between the nominal collimated beam width (width of active detector arrays) and the table feed per rotation of the gantry, so-called pitch. (source: Bushberg; Seibert; Leidholdt Jr; Boone, 2011).....	36
Figure 12 – X-ray beam trajectories around the patient for different pitch values. $p < 1$ results in overscanning (top); for pitch $p = 1$ there is no overlap of the radiation beam path, and no uncovered regions; for pitch $p > 1$ some regions may be uncovered due to underscanning. (source: Hypermedia MS).	37
Figure 13 – A cross section of a CT scan is shown (see inset figure showing orientation). (a). Adjustment of slice thickness in single slice CT depends only of the X-ray beam width, defined by the pre-patient collimator; (b). In multiple detector array CT (MDCT) slice thickness and X-ray beam width are not related anymore. The detector array width (T) defines the minimum CT slice width, while the overall X-ray beam width ($\geq N.T$) is determined by the collimator; (c). Cone Beam CT systems (CBCT) are essentially MDCT systems that have a very large number of detector arrays. (source: Bushberg; Seibert; Leidholdt Jr; Boone, 2011, adapted).....	38
Figure 14 - The intensity I of radiation. Three different cases are illustrated, involving homogeneous and inhomogeneous objects, crossed by monoenergetic or polyenergetic X-ray beams. For inhomogeneous objects tomographic imaging is necessary to determine the distribution $\mu x, y$. (source: Kalender, 2011).	40
Figure 15 - Simple measurement setup. A collimated radiation source emits a pencil beam, and the detectors placed opposite register the intensity attenuated by the object. For a given angular position, the X-ray tube and detector translate linearly, and this setup rotates around and measures the attenuation for many different angular positions. This is the exact procedure in early CT scanners. (source: Kalender, 2011)	42
Figure 16 – Algebraic Reconstruction Techniques (ART) is the most easily comprehensive and was the most common approach to image reconstruction. The N^2 unknown values of an $N \times N$ image matrix can be determined by solving a system of linear equations. (source: Kalender, 2011a).	43
Figure 17 – Backprojection as image reconstruction method, with and without convolution. Backprojection without convolution leads to unsharp images. Convolution before backprojection, essentially as a high pass filtering, counteracts this unsharpening. (source: Kalender, 2011).....	44
Figure 18 – Different convolution kernels can influence image characteristics. (source: Kalender, 2011).	45
Figure 19 - PMMA cylindrical head phantom (16-cm diameter, front) or body phantom (32-cm diameter, back). The central and peripheral holes are also showed. (source: Costa, 2015).....	47
Figure 20 – Different approaches used by four different groups: (a). McCollough and collaborators performed physical dose measurements using a series of anthropomorphic tissue-equivalent phantoms; (b). Toth and Strauss used the two reference body and head PMMA phantoms and a third 10 cm diameter phantom; (c). McNitt-Gray and collaborators performed Monte Carlo dose calculations using anthropomorphic mathematical phantoms and (d). Boone and colleagues	

performed Monte Carlo dose calculations on mathematical cylinders with different diameters and compositions. (source: AAPM, 2011).	50
Figure 21 – The anteroposterior (AP) and lateral dimension (LAT), and the effective diameter. The effective diameter represents the diameter of the patient at a given location along the z-axis, assuming that the patient has a circular cross section. (source: AAPM, 2011 ⁴⁰).	51
Figure 22 – (a). Longitudinal AEC, with tube current modulation along the z-axis; (b). For Angular AEC, the tube current varies considering the different attenuations in the lateral and AP/PA projections; (c). Combined Longitudinal and Angular AEC. (source: MHRA, 2005).	56
Figure 23 – Different stages involved in the TL process. (a). Excitation of the TL material creating free electrons and holes; (b). Latency period characterized by a metastable concentration of electrons and holes captured at defects in the crystal; (c). Stimulation of the material with controlled heating, leading to recombination of electron-hole pairs and emission of light (TL). (source: Yuki-hara; McKeever, 2011, adapted).	57
Figure 24 – (a). The slices of the anthropomorphic adult RANDO phantom; (b). The phantom used in the present study, mounted. (source: The Phantom Laboratory, 2012).	59
Figure 25 – TL/OSL reader Risø (DTU Nutech. Inc., Rødkilde, Denmark) (left) and its Carousel with 48 stainless steel cups (right).	60
Figure 26 – An example of a TL curve for a LiF TLD (TLD-100, Harshaw Chemical Company, OH, USA). Dosimeter data from the Risø TL/OSL reader, presented to the user in counts per temperature in Celsius degree. The TL peak is around 250 °C.	61
Figure 27 – (a). The PMMA holder with 680 TLDs positioned to irradiation. (b). Theratron® Teletherapy (Best Theratronics Ltd., ON, Canada) containing a ⁶⁰ Co source.	62
Figure 28 – TLD holders (left) positioned next to TLDs and a scale; Technical draft in mm (right) of the Thermoluminescent dosimeter holder, specially designed to be used in this study.	63
Figure 29 – Lateral (LAT) and anteroposterior (AP) dimensions of the adult RANDO phantom, measured using JiveX®.	70
Figure 30 – Seven CT protocols used for phantom irradiation: one protocol of total body CT with double SPR, three thorax protocols with constant tube current, two protocols with tube current modulation and a double SPR of the thorax.	71
Figure 31 – Six groups of TLDs (in blue) distributed inside phantom slice 15 for irradiation with the total body protocol.	72
Figure 32 – Calibration curve for TLDs, relating TL values to Air Kerma. Intercept value was set zero and slope value is $2.00(5) \times 10^{-5}$ ($R^2 = 0.997$).	77
Figure 33 – Most frequent CT examinations at ICESP during 2012. CT of thorax represented almost 30% of all CT scans performed in that year.	78

Figure 34 - Most frequent CT examinations at InRad from 2012 - 2014. CT of thorax represented around 13 % of CT scans performed in the evaluated period, being the fourth most frequent CT procedure..... 78

Figure 35 - Linear fit performed with the results for rectal doses obtained from Mueller et al (red curve), and from the present study for lung doses (blue curve). The curves suggest a linear dependence between both organ doses estimated with TLDs, and SSDE estimated with patients' effective diameter and $CTDI_{vol}$ value displayed by the scanner. Linear fit was performed using the plotting and data analysis software Origin® (OriginLab Co., MA, USA). Fitting parameters are 1.004(12) for angular coefficient, $R^2 = 0.999$ (for rectal doses); and 1.331(37) for angular coefficient, $R^2 = 0.996$ (for lung doses). Linear coefficient was set zero in both cases. The estimated uncertainties for lung dose values are within 3 %. 94

Figure B1 - Scheme illustrating all the uncertainties used to the overall uncertainty for lung absorbed dose estimation 109

LIST OF TABLES

Table 1 - Major events along the history of computed tomography, showed chronologically.....	22
Table 2 – Comparison of performance characteristics of CT, from 1972 to 2010. The values considered are for high performance scanners.....	26
Table 3 – Lung mass fraction f_i distributed inside each slice i of the adult anthropomorphic RANDO phantom. The sum of slices 10 and 11 will be referred to as slice 11, and the sum of slices 19 and 20 will be called slice 20.....	59
Table 4 – Compounds of Nylon 6 and Polyoxymethylene, with corresponding mass fraction and effective atomic number.....	64
Table 5 – Correction and calibration factors for the 30 cc ionizing chamber.....	65
Table 6 – Lung tissue and air composition. These information were used at NIST database in order to calculate lung and air mass energy-absorption coefficients for lung and air.	68
Table 7 – Anteroposterior (AP) and lateral (LAT) dimensions of the adult RANDO phantom, measured virtually using the SPR scans and directly with the phantom slice. Five co-workers measured five different values for each quantity in order to estimate user-dependent uncertainties derived from JiveX®.....	70
Table 8 – TLD groups distributed inside the RANDO Phantom for a total body protocol, and corresponding lung total mass fraction.	72
Table 9 – Parameters for the phantom irradiation with a Total Body CT protocol. The values for $CTDI_{vol}$ and DLP displayed by the scanner are also shown.....	73
Table 10 - TLD groups distributed inside the RANDO Phantom for SPR and thorax protocols, and corresponding lung total mass fraction.	73
Table 11 - Parameters for the phantom irradiation with Standard, Low Dose and Ultra Low Dose CT protocols. The equipment-given values for $CTDI_{vol}$ and DLP are also shown.	74
Table 12 - Parameters for the phantom irradiation with Auto mA and Auto + Smart mA CT protocols. The equipment-given values for $CTDI_{vol}$ and DLP are also shown.....	75
Table 13 – Values of K_{AR} (mGy) and TL values, for TLD groups irradiated with different mAs with a radiation beam quality RQT 9.	76
Table 14 – Average value and standard deviation for a RANDO Phantom's anteroposterior (AP) and lateral (LAT) dimensions. Calculated values for the effective diameter (EF) are also shown.....	79
Table 15 – Lung absorbed dose and further dosimetric quantities for total body CT protocol.	80
Table 16 - Lung absorbed doses and further dosimetric quantities for all thorax protocols with constant tube current: "Standard", "Low Dose" and "Ultra Low Dose". Aiming to reduce patient absorbed dose without compromising image quality, "Low Dose" and "Ultra Low Dose" protocols	

were proposed by a team of radiologists. For the three protocols, the voltage value set for irradiation was 120 kV.	81
Table 17 - Lung absorbed doses and further dosimetric quantities for all thorax protocols with tube current modulation: “Auto mA”, which modulates the tube current only in longitudinal direction, and “Auto + Smart mA”, which combines longitudinal and angular modulations.	82
Table 18 – Summary of lung absorbed doses, and further dosimetric quantities, due to all 7 scan protocols investigated.....	83
Table 19 – Lung absorbed doses due to the Standard, Low Dose and Ultra Low Dose thorax CT protocols estimated by the present work (with TLD measurements) and by the methodology proposed by Huda et al.	89
Table 20 – Lung dose values estimated with TLDs and with Monte Carlo Simulations. The values simulated with Monte Carlo overestimate the lung absorbed dose, when compared to the experimental results obtained with TLDs. This can be due to discrepancies in CT scanner model, phantom model and scan range.	92
Table A1 - Conversion factors for SSDE, as a function of effective diameter for CTDIvol based on the use of 32-cm diameter body dosimetry PMMA phantom	107
Table A2 - Conversion factors for SSDE, as a function of effective diameter for CTDIvol based on the use of 16-cm diameter body dosimetry PMMA phantom	108

ACRONYMS

AAPM – American Association of Physicists in Medicine

AEC – Automatic Exposure Control

ALARA – As Low As Reasonably Achievable

AP – Anterior Posterior

ART – Algebraic Reconstruction Technique

CBCT – Cone Beam Computed Tomography

CT – Computed Tomography

CTDI - Computed Tomography Dose Index

CTN – Computed Tomography Number

DICOM – Digital Imaging and Communication in Medicine

DLP – Dose Length Product

EF – Effective Diameter

FBP – Filtered Back Projection

GE – General Electric

GSF – Gesellschaft für Strahlen und Umweltforschung mbH

HU – Hounsfield Unit

HVL – Half Value Layer

IC – Ionization Chamber

IR – Iterative Reconstruction

LAT – Lateral

LD – Low Dose

LDCT – Low Dose Computed Tomography

MC – Monte Carlo

MDCT – Multi Detector Computed Tomography

MSCT – Multi Slice Computed Tomography

NIST – National Institute of Standards and Technology

NRPB – National Radiation Protection Board

OLSD – Optically Stimulated Luminescence Dosimeters

PA – Posterior Anterior

PACS – Picture Archiving and Communication System

PET/CT – Positron Emission Tomography/ Computed Tomography

PMMA – Poly(methyl methacrylate) Acrylic

PMT – Photomultiplier Tube

RIS – Radiology Information System

SD – Standard Deviation

SPR – Scan Projection Radiograph

SSDE – Size Specific Dose Estimates

TCM – Tube Current Modulation

TLD – Thermoluminescent Dosimeters

ULD – Ultra Low Dose

ULDCT – Ultra Low Dose Computed Tomography

ABSTRACT

Since its development in 1970s the computer tomography (CT) technique have gone through major technological advances, becoming an important diagnostic tool in medicine. Consequently the role of CT in diagnostic imaging expanded rapidly, mainly due to improvements in image quality and speed of acquisition. The radiation dose imparted in patients undergoing CT scans has gained attention, leading the radiology community (radiologists, medical physicists and manufacturers) to work together towards dose estimation and optimization. New methodologies for patient's dosimetry have been proposed in the past decades, based specially on Monte Carlo calculations or experimental measurements with phantoms and dosimeters. In vivo methodologies are also under investigation. Current dose optimization strategies include mainly tube current reduction and/or tube current modulation. The present work proposes a methodology to experimentally estimate lung absorbed doses due to clinical CT protocols using an adult anthropomorphic phantom and Lithium Fluorite (LiF) thermoluminescent dosimeters (TLD). Seven clinical protocols were selected for phantom irradiation, based on their relevance regarding dose optimization and frequency in two major hospital's routine: the Institute of Radiology from the Medical Faculty from the University of São Paulo (*Instituto de Radiologia do Hospital das Clínicas da Faculdade de Medicina da Universidade de São Paulo – InRad*) and the Cancer Institute of the State of São Paulo Octávio Frias de Oliveira (*Instituto do Câncer do Estado de São Paulo Octávio Frias de Oliveira – ICESP*). Four thorax protocols for dose optimization were analyzed: "Auto mA", "Auto + Smart mA", "Low Dose" (LD) and "Ultra Low Dose" (ULD) thorax. The first two aforementioned protocols seek dose reduction by tube current modulation, while the last two propose a decrease on the constant tube current value. Values of 72.9(8) % and 91(1) % of lung dose reduction were achieved with LD and ULD protocols, respectively. "Auto mA" and "Auto + Smart mA" provided 16.8(1.3) % and 35.0(1.2) % of lung dose reduction, respectively. The results from all analyzed protocols are compatible with similar studies published in literature, demonstrating the efficiency of the methodology to lung absorbed dose estimation. Its applicability could be extended to different organs, different clinical CT protocols and pediatric phantoms. Moreover, comparison of lung absorbed doses and Size Specific Dose Estimates (SSDE) for the studied protocols exhibited a tendency of linear dependency. Results from similar studies demonstrate a similar behavior between rectal doses and SSDE, suggesting that organ absorbed doses and SSDE values may be linearly dependent, with organ-specific linear coefficients. Further investigation in organ doses is necessary to evaluate this assumption.

RESUMO

Desde o seu desenvolvimento na década de 1970 a tomografia computadorizada (TC) passou por grandes mudanças tecnológicas, tornando-se uma importante ferramenta diagnóstica para a medicina. Consequentemente o papel da TC em diagnóstico por imagem expandiu-se rapidamente, principalmente devido a melhorias na qualidade da imagem e tempo de aquisição. A dose de radiação recebida por pacientes devido a tais procedimentos vem ganhando atenção, levando a comunidade científica e os fabricantes a trabalharem juntos em direção a determinação e otimização de doses. Nas últimas décadas muitas metodologias para dosimetria em pacientes têm sido propostas, baseadas especialmente em cálculos utilizando a técnica Monte Carlo ou medições experimentais com objetos simuladores e dosímetros. A possibilidade de medições *in vivo* também está sendo investigada. Atualmente as principais técnicas para a otimização da dose incluem redução e/ou modulação da corrente anódica. O presente trabalho propõe uma metodologia experimental para estimativa de doses absorvidas pelos pulmões devido a protocolos clínicos de TC, usando um objeto simulador antropomórfico adulto e dosímetros termoluminescentes de Fluoreto de Lítio (LiF). Sete protocolos clínicos diferentes foram selecionados, com base em sua relevância com respeito à otimização de dose e frequência na rotina clínica de dois hospitais de grande porte: Instituto de Radiologia do Hospital das Clínicas da Faculdade de Medicina da Universidade de São Paulo (InRad) e Instituto do Câncer do Estado de São Paulo Octávio Frias de Oliveira (ICESP). Quatro protocolos de otimização de dose foram analisados: “Auto mA”, “Auto + Smart mA”, “Baixa Dose” (BD) e “Ultra Baixa Dose” (UBD). Os dois primeiros protocolos supracitados buscam redução de dose por meio de modulação da corrente anódica, enquanto os protocolos “BD” e “UBD” propõem a redução do valor da corrente anódica, mantendo-a constante. Os protocolos BD e UBD proporcionaram redução de dose de 72,7(8) % e 91(1) %, respectivamente; 16,8(1,3) % e 35,0(1,2) % de redução de dose foram obtidas com os protocolos “Auto mA” e “Auto + Smart mA”, respectivamente. As estimativas de dose para os protocolos analisados neste estudo são compatíveis com estudos similares publicados na literatura, demonstrando a eficiência da metodologia para o cálculo de doses absorvidas no pulmão. Sua aplicabilidade pode ser estendida a diferentes órgãos, diferentes protocolos de CT e diferentes tipos de objetos simuladores antropomórficos (pediátricos, por exemplo). Por fim, a comparação entre os valores de doses estimadas para os pulmões e valores de estimativas de doses dependentes do tamanho (*Size Specific Dose Estimates* – SSDE) demonstrou dependência linear entre as duas grandezas. Resultados de estudos similares exibiram comportamentos similares para doses no reto, sugerindo que doses absorvidas pelos uma órgãos podem ser linearmente dependente dos valores de SSDE, com coeficientes lineares específicos para cada órgão. Uma investigação mais aprofundada sobre doses em órgãos é necessária para avaliar essa hipótese.

INTRODUCTION

Computed Tomography (CT) is an important diagnostic tool in medicine, and has become a crucial imaging method in clinical routine¹. CT images are produced by passing X-rays through the body at a large number of angles, by rotating the X-ray tube around the patient; the transmission projection data is collected by a detector array placed opposite to the X-ray tube. A computer synthesizes the collected data points into tomographic images of the patient. The term tomography refers to a picture (*graph*) of a slice (*tomo*)².

CT was the first imaging technique to provide exclusively computed digital images of the inside of the human body, in a non-invasive way. It was also the first to provide images that were not biased by eventual superposition of distinct anatomical structures^{3,4} presenting an unobstructed view of detailed anatomy to the physician. Moreover, with this imaging technique it is possible to obtain a volumetric representation of the body by slices. Modern CT scanners can acquire 0.50 to 0.62 mm thick tomographic images from 50 cm length of the patient (i.e., 800 images) in 5 second, being able to reveal presence of cancer, ruptured disks, subdural hematomas, aneurysms and many other pathologies².

Since its development, in the 1970s, the role of CT in diagnostic radiology has rapidly expanded, mainly due to the speed of acquisition and the high-quality diagnostic images. According to surveys conducted in the United States, 3.6 million CT examinations were performed in 1980, just a few years after its inception⁵. In 1990, this number has increased to 13.3 million⁶ and in 2014 to 81.2 million, a value 7% higher than in 2013⁷. In 2001, it is estimated that CT accounted for over 13% of all diagnostic exams, contributing to approximately 30% of the American population's collective dose⁸. In 2006 such values have increased to 17% of all diagnostic exams, with 49% contribution to collective dose⁹.

Another example is the situation in Germany, where CT examinations increased from 4.2% of all radiological examinations in 1996¹⁰ to 7% in 2006¹¹, with contribution to collective effective dose increasing from 37.8% to 60% in this period. In a worldwide perspective, CT exams corresponded to only 7% of the medical procedures on 2007, but have contributed with 40% of the collected dose¹².

The prescription and use of CT in Brazil has also increased. In the Brazilian public health system (*Sistema Único de Saúde – SUS*) over 1.5 million CT scans were performed in 2008; this value increased to more than 3.6 million CT examinations in 2014¹³. Despite the continuous effort in dose reduction, it is yet the diagnostic modality using ionizing radiation that most contributes for the patient dose¹⁴.

The increase in the clinical use of CT have had several reasons, and among them is the improvement in CT performance during the 1990s with the introduction of fast spiral CT scanning and the development of multi-row detector technology¹⁵. Nowadays it is possible to perform high-resolution CT exams within a few seconds, offering excellent diagnostic capabilities and patient comfort. As a consequence of the increase in the prescription of CT examinations, doses received by patients due to this technique has gained attention. The radiation dose to individual radiosensitive organs is currently the preferred quantity to evaluate the risk or radiation exposure¹⁶⁻¹⁸. Therefore different methodologies have been proposed in the past decades.

The present work aims to develop a methodology to estimate lung absorbed doses due to CT clinical protocols, using Lithium Fluorite (LiF) thermoluminescent dosimeters (TLDs) and an adult anthropomorphic phantom. After evaluation on the quantity and frequency of CT scans performed in two major hospitals in São Paulo, seven different clinical protocols were selected, based on their relevance regarding frequency and dose optimization, including one total body protocol, five thorax CT protocols and one double scan projection radiograph (SPR). Size Specific Dose Estimates (SSDE) values were calculated for all protocols, except SPR, and their correlation with the estimated lung absorbed doses was investigated.

To properly describe the proposed methodology, the present work is divided in six chapters:

- Chapter 1 presents all the theoretical fundamentals on which the research was based;
- Chapter 2 describes all the instrumentation used in the data collection and analysis, the methodology for dose estimation and the parameters for phantom irradiation with the selected CT clinical protocols;

- Chapter 4 presents all the results obtained during this work, with the lung absorbed dose results presented separately for each kind of irradiation: total body protocol, SPR, and thorax protocols;
- Chapter 5 discuss the achieved results, by analyzing the dose estimates for each protocols and comparing them with similar published studies and with calculations based on Monte Carlo methods;
- Finally, chapter 6 presents the conclusions and suggestion for future investigations.

1. THEORY

1.1. A BRIEF HISTORY OF CT

X-ray CT is considered the most important innovation in radiology since the discovery of the X-rays themselves by Wilhelm Röntgen in 1896, for which he was awarded the first Nobel Prize for Physics in 1903. Since then, many researchers have dedicated their time in the development of imaging techniques using X-rays. In 1972 the first medical use of an X-ray CT scanner was announced, the EMI Mark I scanner. This equipment was available after the effort of Godfrey Newbold Hounsfield and Allan MacLeod Cormack, who were jointly awarded the Nobel Prize for Physiology and Medicine in 1979. Its origins, however, rely on unconnected pieces of research from many years before (Table 1)^{3,19}.

Table 1 - Major events along the history of computed tomography, showed chronologically.

Year	Major events throughout history of computed tomography
1895	W. C. Röntgen; X-ray discovery
1917	J. H. Radon; Mathematical solution for reconstruction from projections (Radon's Transform)
1920	W. Watson; synchronized rotation of object and film (radiotherapy)
1940	G. Frank; analog method of reconstruction
1945	S. Takahashi; experiments with manual and optical methods for back-projection
1963	A. M. Comarck; experimental CT scanner
1965	D. E. Kuhl and R. Q. Edwards; emission tomography using ^{131}I e ^{198}Au
1967	G. N. Hounsfield; first work on X-ray CT
1967	R. N. Bracewell and A. C. Riddle; studies on convolution and back-projection method of reconstruction from projections
1972	G. N. Hounsfield and A. M. Cormack; First clinical X-ray CT scan with EMI scanner
1974	Seventy CT scanners installed (head only)
1975	R. Ledley; total body CT scanner
1989	W. Kallender; Spiral CT
1991	Demonstration of Multislice CT

Since its development in 1970's CT technology has improved continuously, aiming to adapt to the demands on radiology. In addition to other necessities, such as improvement of image quality and costs reduction, the reduction of examination times appears to be the main goal to be achieved. Not only the time to acquire a single image needed to be reduced, but also the speed of a complete examination, which includes the image reconstruction time for example⁴. In four decades scan times reduced drastically, from up to nine days to fractions of seconds. Moreover, the image reconstruction processes are not just faster, but result in images with much better diagnostic quality, using 512 x 512 image matrices in contrast to 80 x 80 matrices used in early 70s.

Even though many authors separate the evolution of CT scanners in generations^{2,3} usually related to detection geometry of the equipment and system components, this type of assortment will not be adopted in the present work. Instead, the CT technology development will be classified according to Kallender⁴, who organized it by the pursued goal in each decade.

1.1.1. The Seventies – from Head to Whole Body Scanning

The first CT scanner was the Hounsfield's prototype (Figure 1a), often termed "first generation". In the first trials in 1969 using test objects, so-called phantoms, Hounsfield could perform a CT scan using isotope sources; the scan time required was nine days per image and 2.5 hours for image reconstruction. The X-ray source and detector translated over the phantom, obtaining one transmission profile (or "projection"), rotate in one-degree steps and translate again repeating the process. The X-ray beam was highly collimated and therefore known as pencil-beam.

With a small change in his experimental setup, by adding scanning detectors ("second generation"), the scan time dropped to only 5 minutes and the image reconstruction was carried out simultaneously (Figure 1b); total examination time reported was 35 minutes. Hounsfield could sample 180 projections in one degree steps with 160 data points each, i.e. 28,800 data points per scan, which was sufficient to calculate an image with 6,400 pixels (80 x 80 image matrix).

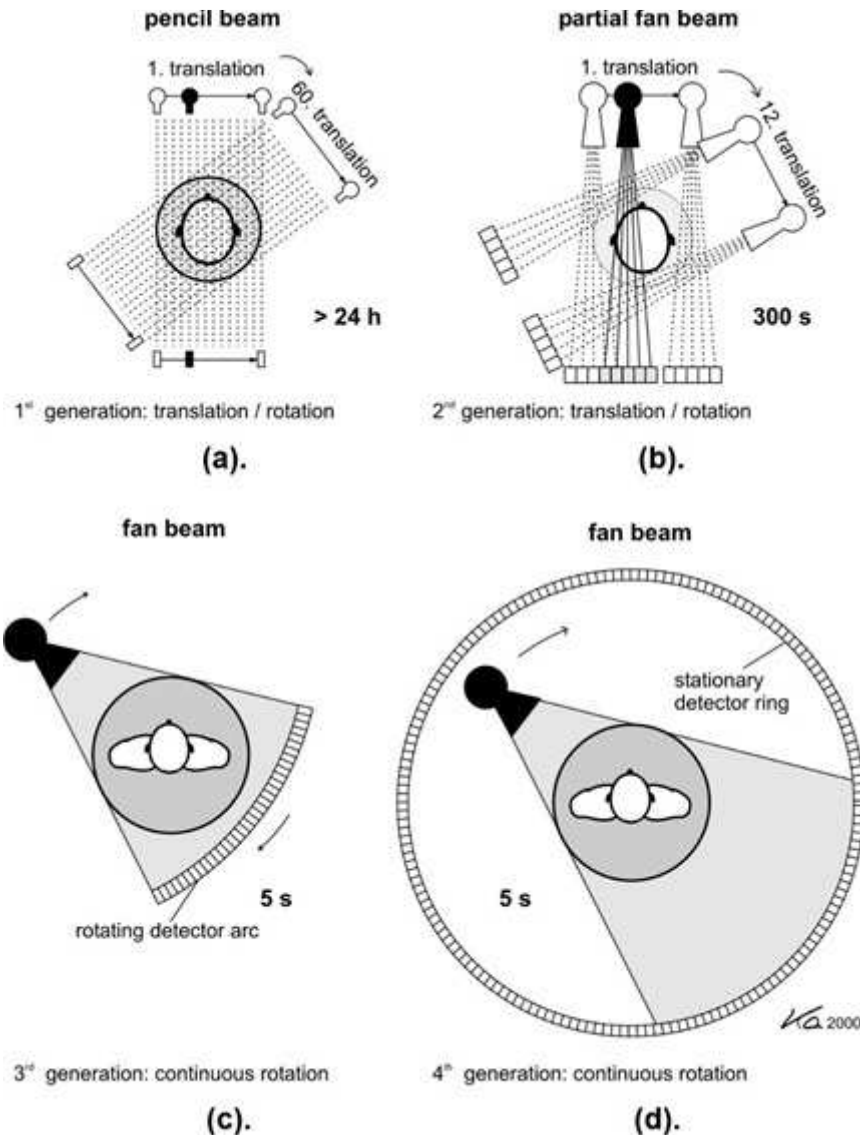


Figure 1 – Historical perspective of CT scanners evolution. (a). Head scanners, which scanned the patient by translation and rotation of the measurement system with a pencil beam or (b). a small fan beam; (c). The “3rd generation”, featuring a rotating detector, has clearly outdistanced the (d). “4th generation”, which utilizes stationary detector rings. (source: Kalender, 2011⁴, adapted).

Most translation-rotation scanners commercially available offered field for head measurements only, due to the narrow X-ray beam but especially due to long acquisition times that could not handle patient motion. Therefore, the technical goal was to reduce the scan time per image to 20 seconds, achieved with the introduction of the so-called fan-beam (Figure 1c). In this configuration, the fan-beam rotates 360° together with a large detector arc, obtaining a complete projection. X-ray source translation is not necessary anymore and the system now only rotates around the patient (“third generation”). The first whole body scanners with fan-beam became available in 1976. Later on, some manufacturers created a scanner with a ring-like

stationary detector encircling the patient (Figure 1d), so that only the X-ray tube rotated (“fourth generation”). Having so many detectors was not cost-effective, and the third-generation configuration has prevailed.

1.1.2. The Eighties – Fast Scanning of Single Slices

Due to electrical feeding of the X-ray tube, done with thick cables mounted on a spool, the third-generation system could not rotate fast and continuously. The system had to be rotated in one direction, stopped after a certain angle and then rotated to the opposite direction. In this process the cable was unwound in one direction and carefully wound up in the other, which was a major obstacle in reducing acquisition times⁴. This technique could allow scan times down to two seconds, but this was not fast enough anymore for some diagnostic needs.

From the many creative approaches presented in the eighties to lower even more the scan times, the possibility to continuously rotate conventional systems has proven to be the most promising one. This was achieved with the “slip ring technology”, introduced by Siemens Medical System and Toshiba Medical Systems in 1987. Slip rings are electric-mechanic conductor dispositive which provide energy and collect data via sliding contact between ring-shaped electrical conductors and sliding “brushes” distributed all over the rotation surface^{20,21}. This enabled the system to operate with continuous data acquisition. Not only scan times were reduced, but this technology also provided the basis for spiral CT, a technique largely used today.

1.1.3. The Nineties – Fast Volume Scanning

In 1990 there was only one scanner with spiral CT scan mode available (Siemens SOMATON PLUS). By 1992, all major CT manufacturers have announced scanners with slip ring technology and spiral CT capabilities. Since then an amazing technical development has been observed, increasing X-ray power, computer capabilities and further technical improvements, as the introduction of multi-slice CT (MSCT), also called multi-detector CT (MDCT), and cone-beam CT (CBCT).

With CBCT, the scan times could be reduced even more. In the year of 1998 the introduction of four-slice CT system provided scan times as low as 500 ms, meaning a reduction of volume scan times by a factor of 8 compared with the typical 1s scan time achievable with single-slice systems.

1.1.4. The 2000s – Diversity and Even Faster Volume Scanning

The trends shown in previous decade continued during the 2000s. With the introduction of wider cone beams, volume scans could be performed even faster. The development of new CT modalities, such as dual source CT and dual energy CT, also happened in this period.

Table 2 summarizes the development of some performance characteristics of CT in the course of time⁴. Contrast resolution appears to have reached a plateau already in 1980s, as could be expected according to physics, since efficient detector systems have been available at an early stage.

Table 2 – Comparison of performance characteristics of CT, from 1972 to 2010⁴. The values considered are for high performance scanners.

	1972	1980	1990	2000	2010
Rot. Time per 360°	300 s	5-10 s	1-2 s	0.33-0.5 s	0.27-0.35 s
Min. eff. scan time	300 s	3 s	0.7 s	0.2-0.3 s	0.075-0.2 s
Data per 360° scan	57.6 kB	0.2-1 MB	1-2 MB	5-20 MB	0.1-1 GB
Data per spiral scan	-	-	12-24 MB	0.1-1 GB	1-100 GB
Image matrixⁱ	80 x 80	256 x 256	512 x 512	512 x 512	512 x 512
Power	2 kW	10 kW	40 kW	60-100 kW	80-120 kW
Slice thickness	13 mm	2-10 mm	1-10 mm	0.5-1 mm	0.4-0.6 mm
Spatial resolution	3 Lp/cm	8-12 Lp/cm	10-15 Lp/cm	12-15 Lp/cm	12-25 Lp/cm
Contrast resolutionⁱⁱ	5 mm/5 HU/50 mGy	3 mm/3 HU/30 mGy	3 mm/3 HU/30 mGy	3 mm/3 HU/30 mGy	3 mm/3 HU/30 mGy

ⁱ Values refer to the calculated matrix.

ⁱⁱ Refers to the ability of an imaging procedure to depict very subtle differences in contrast².

1.1.5. The 2010s – The decade of Dose Reduction

Significant dose reduction and improvements on image quality can be expected for this decade⁴. In fact, dose reduction can be achieved by several ways, and modern CT scanners already include tools for lowering radiation doses, such as iterative reconstruction algorithms, tube current modulation systems and safety cut-offs to prevent excessive doses²². Iterative reconstruction (IR) techniques²³ can

generate images with significantly lower noise, therefore allowing reduced patient exposure²⁴. Tube current modulation (TCM) can lower the dose by up to 40 %²⁵. Moreover, some specific CT protocols for dose optimization have been proposed by subspecialty societies, like the Alliance for Radiation Safety in Pediatric Imaging, which is concerned with the dose for pediatric patients²⁶.

1.2. COMPUTED TOMOGRAPHY SCANNERS

CT scanners are composed, basically, by X-ray tube and detectors mounted in a mechanical rotating system, filters, patient couch, high voltage generator, computer system and a control panel.

1.2.1. X-ray Tube

X-ray tubes are composed by a cathode and an anode placed inside a vacuum glass enclosure that provides electrical insulation between both electrodes (Figure 2). In diagnostic medicine, X-ray tubes are designed in two types: stationary anode tubes for low power applications and rotating anode tubes for midrange and high performance applications²⁷.

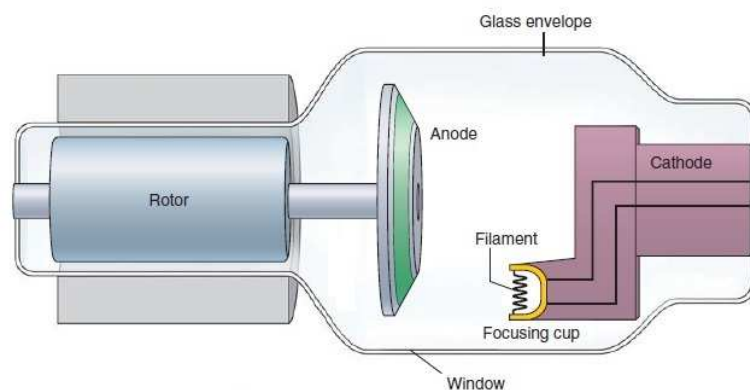


Figure 2 - Components of a typical X-ray tube. (source: Fosbinder; Orth, 2011²⁹, adapted).

The cathode is the negative electrode, comprised of tungsten filament or filaments, wound in a helix, and a focusing assembly. When energized, the cathode releases electrons by thermionic emission, which will flow to the anode when a tube voltage is applied between them².

The anode is a beveled metal target electrode maintained at a large positive potential difference relative to the cathode. Electrons produced by the cathode strike the anode surface depositing most of their energy as heat, with only a small fraction emitted as X-rays. Therefore, a large amount of heat is generated in the anode to achieve X-rays production in quantities necessary for acceptable image quality. To avoid heat damage, rotating anodes are used in modern CT scanners, as they spread the heat over a much larger area than stationary anodes, enabling much larger tube currents and exposition times² (Figure 3a).

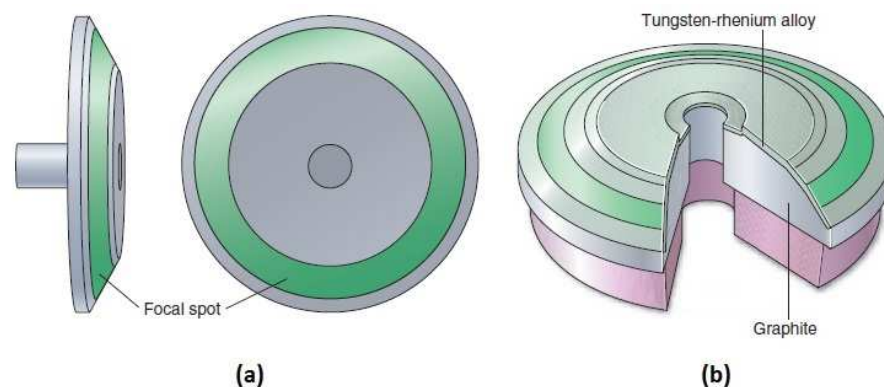


Figure 3 - (a). Rotating anodes spread the heat produced over a circular track, as the high energy electrons strike its surface at the so-called focal spot, creating X-ray; (b). The anode disk is made of graphite, with tungsten-rhenium deposited in one face via chemical steam process. (source: Fosbinder; Orth, 2011²⁹, adapted).

Rotating anodes are disks mounted on a rotor assembly supported by bearings in the X-ray tube insert. The disk is made of graphite, with tungsten or tungsten-rhenium alloy deposited in one face via chemical steam process (Figure 3b). Tungsten provides great bremsstrahlung production graphite increases the heat capacity in the disk by a factor of 10, in comparison to a disk made of pure tungsten and rhenium provides added resistance to surface damage². Therefore, disks manufactured with aforementioned specifications may be larger, though lighter, with higher heat capacity, and can rotate smoothly and faster, up to 10,000 rpm, enabling the use of high exposure parameters. Moreover, anodes lose heat by infrared radiation emission, transferring thermal energy to the tube insert, surrounding oil bath and tube housing. In some cases, sophisticated tube designs with externally mounted oil, air or water heat exchanges are employed².

The rotor base, made of copper and steel and covered with ceramic, increases the heat irradiation avoiding it to spread over other parts of the tube. Lifetime of

rotating tubes may vary from 10,000 to 40,000 hours depending on handling care and maintenance, in comparison to 1,000 hours lifetime of conventional radiology X-ray tubes².

To improve the efficiency of the X-ray tubes the heat capacity from the anodes must be increased. New technologies have been developed to this end, and one possibility is to get the anode disk itself in contact to the cooling medium. The Straton X-ray tube²⁷ (Siemens Medical Solutions, Erlangen, Germany) accomplished this objective with a new modern design, where the anode disk is now part of the tube housing which is entirely embedded in cooling fluid (Figure 4). The Straton tube has a radius of 60 mm and can reach rotating speed up to 150 Hz. The cooling time is drastically reduced, eliminating the need for a large heat storage capacity at the anode.

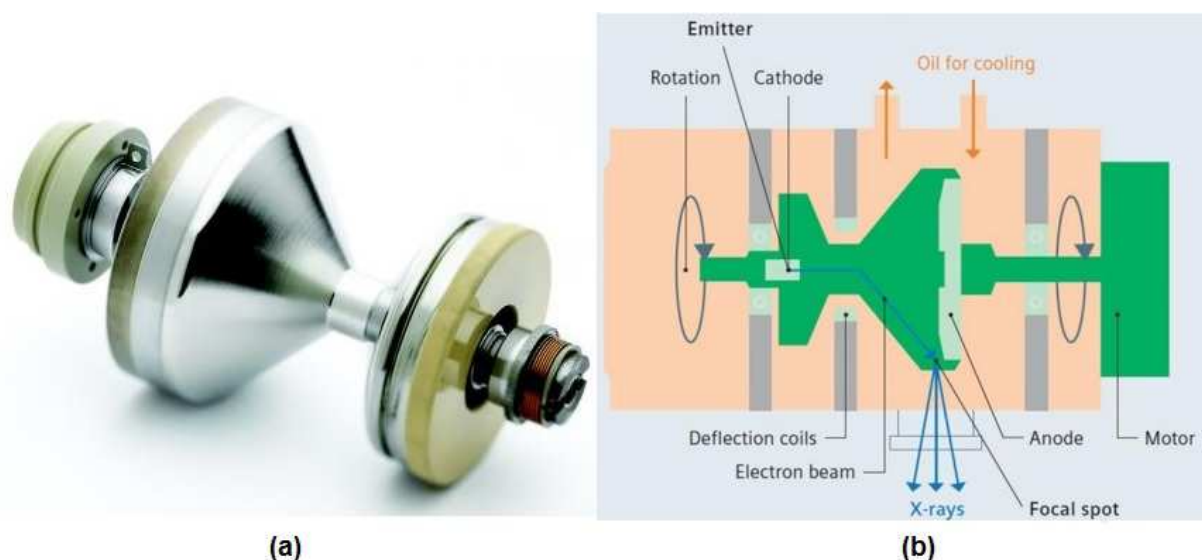


Figure 4 – (a). Siemens's Straton X-ray tube and (b). Its schematics, showing the anode directly attached to the tube envelope (source: Siemens Healthcare GmbH, 2015²⁸, adapted).

1.2.2. Detectors

All modern CT scanners use scintillators solids-state detectors connected to photodetectors². The interaction of X-rays with the scintillator results in emission of light, which is proportionally converted into an electrical signal by the photodetector. Scintillating materials can be in the form of crystals, such as cesium iodide or cadmium tungstate, and ceramic materials, such as gadolinium oxysulfate⁴. As

technical requirements, these detectors must have a fast temporal response and the electronic noise level should be significantly lower than the statistical fluctuations in X-ray intensities due to quantum noise, preferably lower than half the magnitude of the maximum expected quantum noise value⁴.

Absorption efficiency of such detectors for X-ray is very high due to their high density and high effective atomic number. However, to reduce optical cross talk between detectors (undesired detection of photons from adjacent areas) opaque filler is pressed into spaces between detector elements, decreasing the geometric efficiency² (Figure 5).

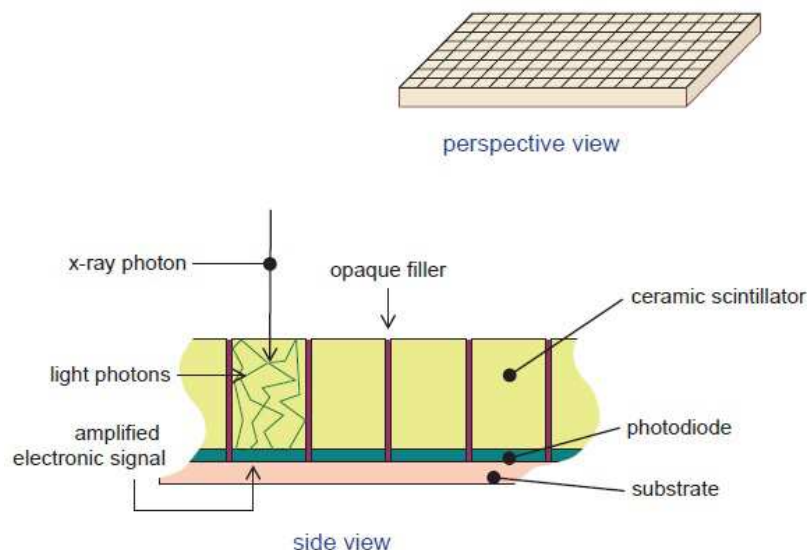


Figure 5 – Detector arrays in modern computed tomography, in a perspective and side view. The side view shows individual detector elements coupled to photodiodes that are layered on substrate electronics, which provide power to the detector system and receive the electronic signal from the photodetector. Opaque filters are pressed into spaces between detector elements to reduce detector cross talk, however the geometric efficiency is also reduced. CT detectors are much more expensive than those used in conventional radiography. (source: Bushberg; Seibert; Leidholdt Jr; Boone, 2011²).

Detector sizes vary from manufacturers, and are typically 1.0 x 15 mm and even thinner for MDCT; some have hybrid detector systems which combine to compound different detector sizes. Smaller detectors together with short decay times improve the spatial resolution.

1.2.3. Filters

Electrons produced at the cathode strike the anode and lose their kinetic energy, generating heat and X-ray photons in a polyenergetic (also called polychromatic) spectrum, the maximum X-ray energy being limited by the voltage

applied between the electrodes; this process is known as Bremsstrahlung radiation². This means that X-rays with energy ranging from 0 to 120 keV will be produced by an X-ray tube when a 120 kV voltage is applied on the electrodes, for example. Filtering is employed in CT to absorb low-energy rays, as they contribute strongly to the dose absorbed by the patient but weakly to the electronic signal in the detectors; this process is called beam hardening, and it results in a more penetrating radiation beam⁴.

Beam shaping filters, so-called bow-tie filters due to their shape, are widely used in CT machines to compensate the ellipsoidal shape of the human body. This kind of filter is positioned in front of the X-ray tube exit window before the patient, and reduces the intensity of the X-ray beam in the periphery of the field, where attenuation path through the patient is usually thinner (Figure 6)². As a result, photon fluence reaching the detector array is more homogeneous.

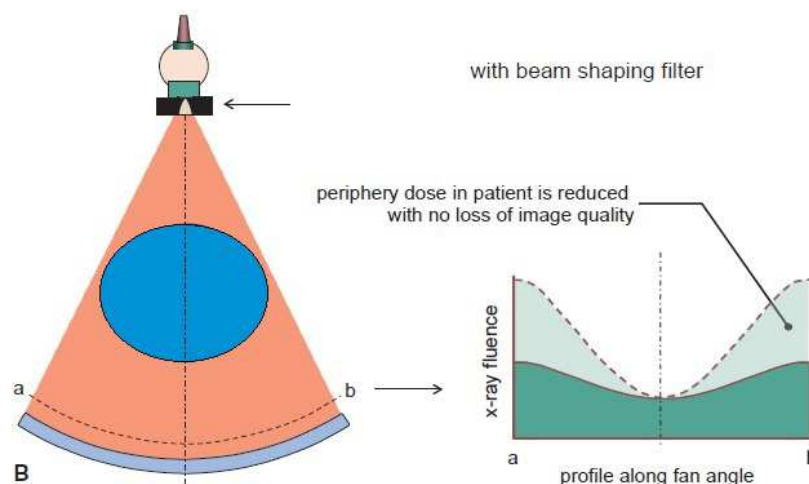


Figure 6 –Without the bow tie filter, the X-ray fluence is much higher at the periphery of the field than at the center (light-green profile), since at the peripheries the attenuation path through the patient is usually thinner. The bow-tie filter reduces the X-ray intensity at the peripheries due to its format, resulting in a more homogeneous photon fluence reaching the detection system (dark-green profile). This creates the opportunity to reduce dose to the patient with no loss of image quality. (source: Bushberg; Seibert; Leidholdt Jr; Boone, 2011², adapted).

1.2.4. Gantry and Patient Couch

The gantry is the main hardware structure of a CT scanner, containing the X-ray system (X-ray tube, collimator and filters), the detectors, the high voltage generators and mechanical supports (Figure 7). All of that weighs about 1,000-2,000kg and rotates rapidly around the patient, inside a large housing that surrounds

it and prevent mechanical injuries^{2,29}. It has an aperture of 50-80 cm for the patient to pass through it during the scan.

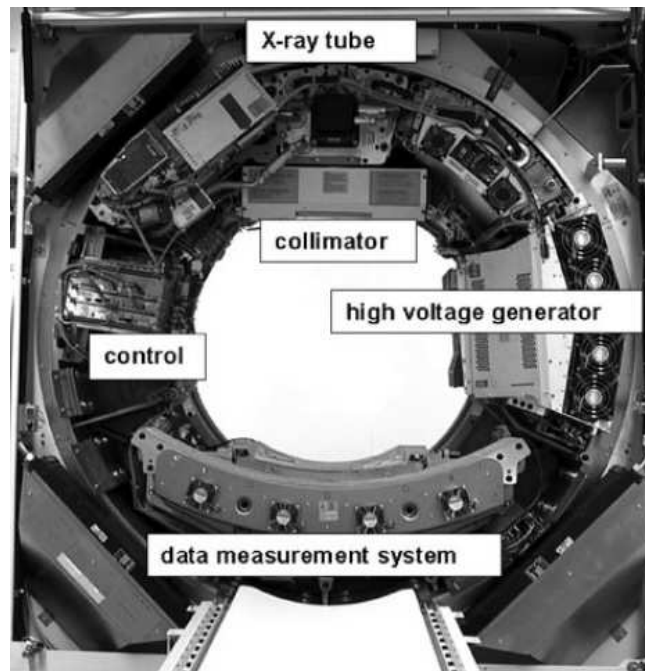


Figure 7 – View of the gantry without its safety housing. The gantry weighs about 1,000-2,000 kg and rotates rapidly around the patient, comprising the X-ray system (X-ray tube, collimator and filters), the detector system, the high voltage generator and mechanical supports. (source: Ulzheimer; Flohr, 2009²⁰).

The patient couch is an intrinsic component of CT scanners. It can be removed from and inserted into the bore of the gantry, it can be lowered down to allow the patient to comfortably get on it and can be move upwards again, according to necessity. A series of laser lights provide reference to allow proper positioning and alignment of the patient^{2,29}.

Couch alignment in the gantry follows the indications in Figure 8³⁰. The x-y plane is called axial plane, the x-z plane is the coronal plane and the y-z plane is the sagittal plane. The gantry rotates around x-y direction and the couch translates along the z direction.

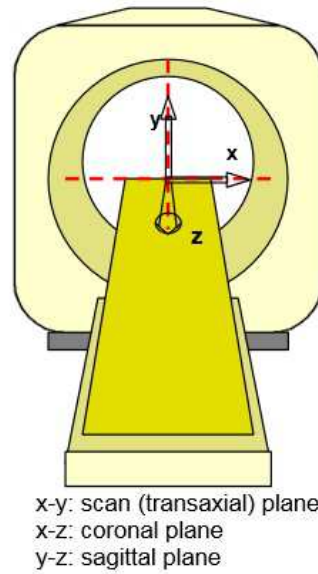


Figure 8 – Gantry and patient couch. The gantry rotates around x-y direction and the couch translates along the z direction. (source: : ImPACT 2001³⁰).

1.2.5. Generator

Two kinds of generators can be used in CT scanners: low frequency generators (60 Hz) and high frequency generators (3,000 Hz). Low frequency generators were too big, and therefore must be located outside the gantry in the CT room and connected to the X-ray tube by thick, flexible high voltage cables, preventing the tube to rotate continuously²⁹.

Low frequency generators are no longer in use. With the development of smaller high frequency systems, the generator could be installed inside the gantry with the X-ray tube, and continuous rotation around the patient became possible²⁹. The input voltage is connected to the circuit through slip rings, enabling spiral CT acquisitions.

1.3. CT ACQUISITION MODES

Computed tomography has evolved and nowadays it can be used for many different purposes. Aiming to better adapt to the variety of applications, many acquisition modes have been developed, as survey radiographs, axial, spiral and cone beam acquisition modes, which will be described in the present work. Further

examples on modes of acquisition are cardiac CT, dual energy CT, angiography and perfusion, among others^{2,4}.

1.3.1. Scan Projection Radiograph (SPR)

Scan projection radiograph (SPR) - also called survview, topogram, scout view, scanogram or localizer, depending on the vendor - is performed prior to the exam for orientation over patient anatomy and positioning. This digital radiograph image is acquired with stationary X-ray tube and detector arrays, and the patient is transported through the field of measurements at low speed. They are mostly taken in anterior-posterior (AP), posterior-anterior (PA) and lateral (LAT) projections^{2,4} (Figure 9).

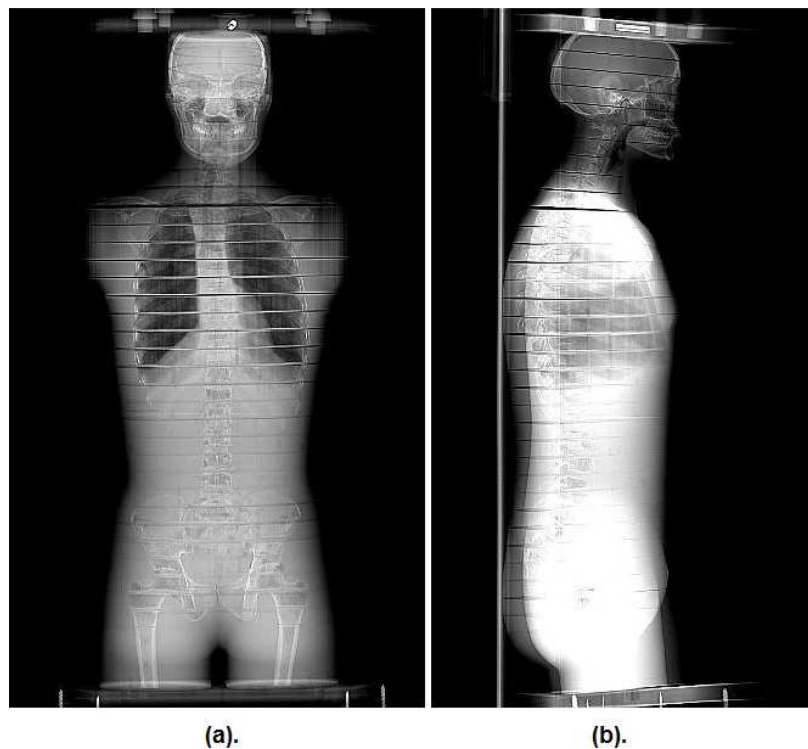


Figure 9 – (a). Anterior-posterior (AP) and (b). Lateral (LAT) scan projection radiographs of the adult anthropomorphic RANDO phantom (The Phantom Laboratory, Salem, NY) used in the present work.

With survey radiographs the CT technologist can select specific slices or scan regions and set all the parameters to be used for the exam. CT parameters include X-ray tube voltage (kV), anode current (mA), gantry rotation time (s), type of scan (spiral or axial), pitch, and detector configuration (single or mult-array) among others. Preset protocols are usually selected^{2,4}.

1.3.2. Axial CT

In the first two decades since its introduction as an imaging diagnostic tool, CT examinations consisted of single slices scanned sequentially. Axial CT, also known as sequential CT, is the combination of single slices acquisition with patient translation for a definite distance: one slice is scanned, the patient is translated, another slice is scanned and the procedure is repeated until the entire scanning length is covered. It is important to mention that X-ray is not produced during the couch translation, reason why it is also called step-and-shot mode of CT examination (Figure 10). Acquisition times are longer than spiral scans due to stop/start sequence^{2,4}.

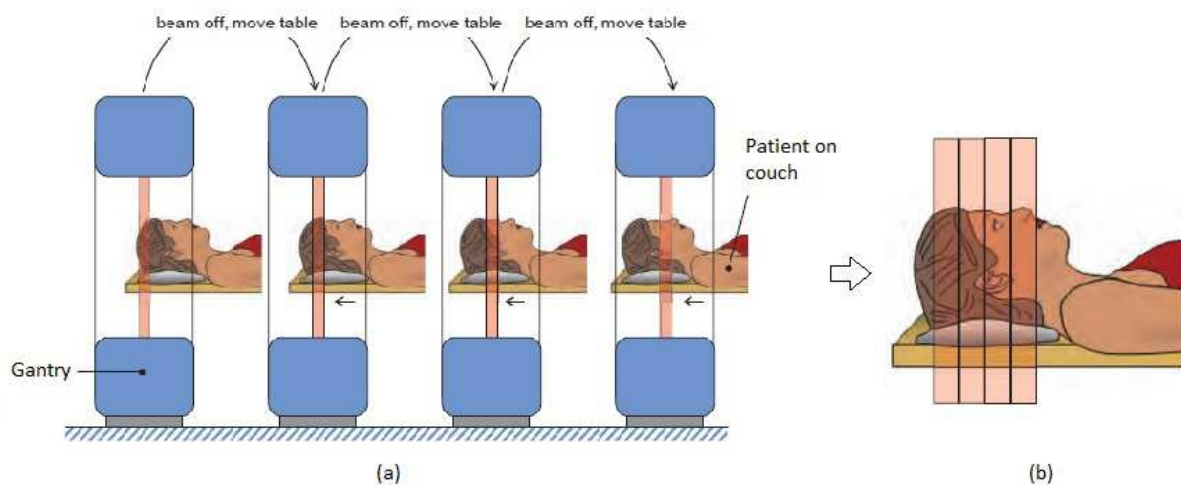


Figure 10 – (a). Axial CT, also known as sequential CT and step-and-shot CT. X-ray beam is off while the patient is being translated between consecutive acquisitions; (b). Consecutive slices are scanned until the entire scanning length is covered. (source: Bushberg; Seibert; Leidholdt Jr; Boone, 2011², adapted).

1.3.3. Spiral or Helical CT

During helical (also called spiral) scanning, the X-ray tube and the detectors rotate around the patient while the patient table moves at a constant speed along the z axis, creating a spiral exposure (Figure 11). As the scanning is now helical, the data has to be interpolated to reconstruct each planar section.

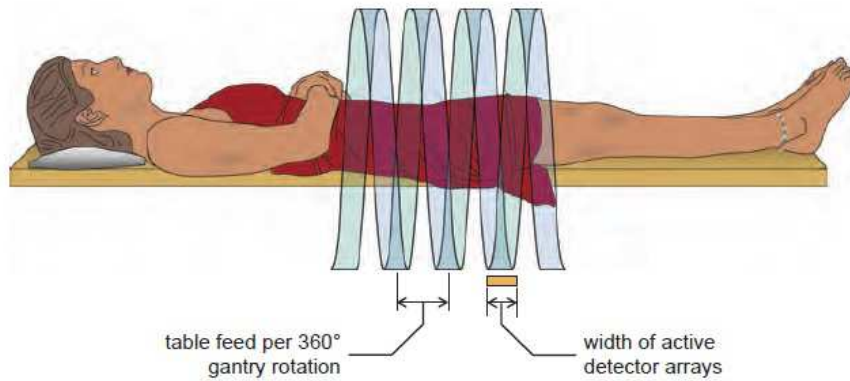


Figure 11 – In spiral or helical CT scanning, the X-ray tube describes a helical trajectory around the patient's body. There is an important relationship between the nominal collimated beam width (width of active detector arrays) and the table feed per rotation of the gantry, so-called pitch. (source: Bushberg; Seibert; Leidholdt Jr; Boone, 2011²).

The relative motion of the table per tube rotation is described by the dimensionless parameter pitch (p) in Equation (1)²:

$$p = \frac{d}{N \times T}, \quad (1)$$

where d is the table feed in mm, $N \times T$ is the nominal collimated beam width, N is the number of detector rows and T is the detector width in mm. This definition is appropriated for single slice ($N = 1$) as well as for multislice ($N > 1$) scans. For example, a 16-slice scan ($N = 16$) with detector width $T = 1.25$ mm and table feed $d = 5$ mm has a pitch of $p = 0.5$. Pitch $p = 1.0$ corresponds to contiguous axial CT (Figure 12, middle). For the same tube current-time product value, pitch $p < 1.0$ results in overscanning and hence higher radiation dose to the patient, but with improved image quality, compared to a scan performed with $p = 1.0$ (Figure 12, top), while pitch $p > 1.0$ represents underscanning and results in lower radiation dose² (Figure 12, bottom), but the resultant images may contain reconstruction artifacts.

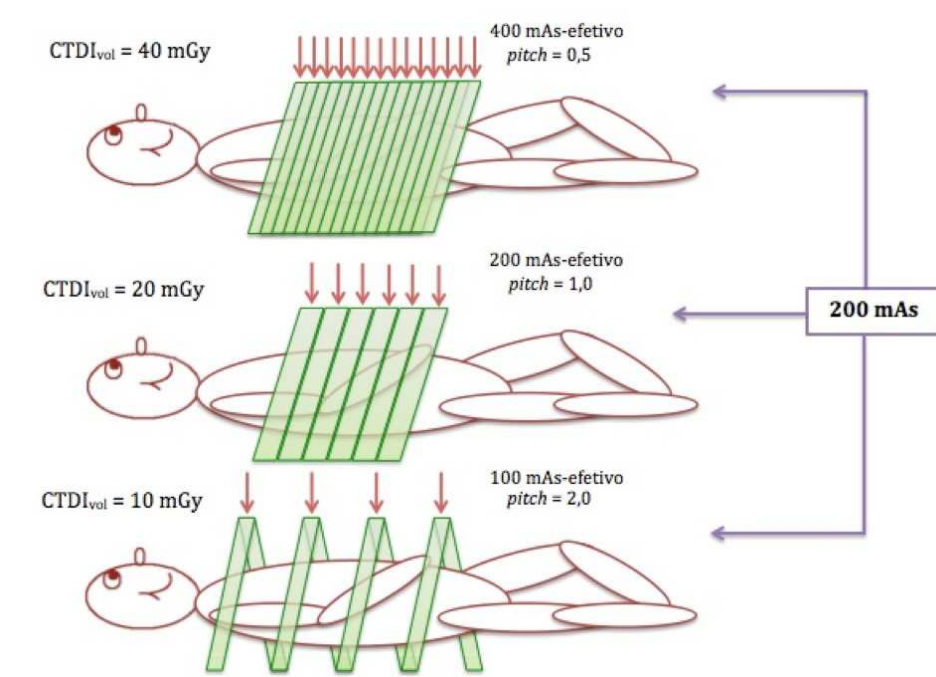


Figure 12 – X-ray beam trajectories around the patient for different pitch values. $p < 1$ results in overscanning (top); for pitch $p = 1$ there is no overlap of the radiation beam path, and no uncovered regions; for pitch $p > 1$ some regions may be uncovered due to underscanning. (source: Hypermedia MS³¹).

1.3.4. Multislice CT and Cone Beam CT

A multislice CT system (MSCT) is a scanner capable of measuring more than one slice simultaneously, based on multi-row detectors in the z direction⁴. MSCT, also called multidetector CT (MDCT), enabled larger volume coverage in shorter scan times in comparison to single detector systems. Therefore a given anatomic volume could be scanned within a given scan time²⁰. Moreover, MSCT systems are more efficient, as more radiation produced in the X-ray tube can be utilized.

Different slice thickness must be provided by CT detectors to adjust optimum scan speed, longitudinal resolution and image noise for each application. In single slice CT the slice thickness is determined only by pre-patient collimation of the X-ray beam (Figure 13a). Widening collimation, consequently increasing the slice thickness, means greater amount of radiation photons reaching the patient, however spatial and contrast resolution are reduced and scatter radiation on the patient increases the noise, which could compromise visualization of some structures in an exam^{2,4}.

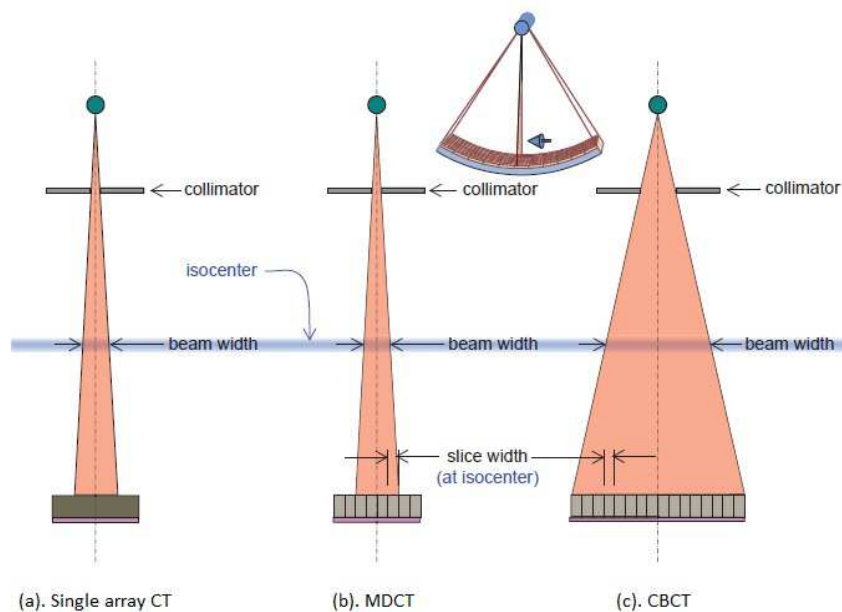


Figure 13 – A cross section of a CT scan is shown (see inset figure showing orientation). (a). Adjustment of slice thickness in single slice CT depends only of the X-ray beam width, defined by the pre-patient collimator; (b). In multiple detector array CT (MDCT) slice thickness and X-ray beam width are not related anymore. The detector array width (T) defines the minimum CT slice width, while the overall X-ray beam width ($\geq N.T$) is determined by the collimator; (c). Cone Beam CT systems (CBCT) are essentially MDCT systems that have a very large number of detector arrays. (source: Bushberg; Seibert; Leidholdt Jr; Boone, 2011², adapted).

For MSCT the number of slices scanned simultaneously are defined not only by pre-patient collimation but also by post-patient electronic combination of signals from the detector array⁴: the collimator adjusts only the overall beam width ($N.T$) and the slice width is governed by the width of the detector arrays (T) (Figure 13b). In a MSCT scanner each detector array has its own data channel and all detector array signals are recorded during a scan. With the introduction of MSCT it became possible to scan an entire detector array of 16 to 320 slices simultaneously, instead of one or only few slices, meaning the transition from fan beam to cone beam CT (CBCT)⁴ (Figure 13c). CBCT can be performed either in axial or in spiral acquisition modes.

Detector row sizes vary by manufacturers and CT models. A 64 slices scanner with detector arrays of 0.5 mm can use all the recorded data to reconstruct 64 x 0.5 mm slices, or 32 x 1.0 mm, 16 x 2.0 mm, 8 x 4.0 mm, etc. Opposite to single slice systems, which have only one long detector, wider slice thickness does not increase

noise nor decreases spatial resolution, as it has several solid state detectors combined to adjust the desired exam requirement².

1.4. IMAGING

CT aims to obtain information regarding the shape and localization of materials inside the body. To do so, it is necessary to measure spatial distribution of a physical quantity from different directions and to compute, with these data, images without superposition⁴.

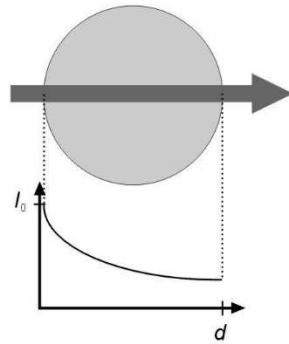
In the case of X-ray CT, as well as in conventional radiography, the relative distribution of X-ray intensity after crossing an object is recorded. However, for classical radiography only the gray value pattern is used to derive a diagnostic. For CT, not only the intensity I attenuated by the object is necessary, but also the primary intensity I_0 , in order to calculate the attenuation value for each ray from source to detector⁴.

In the case of a monoenergetic X-ray crossing a homogeneous object, attenuation can be described by Equation (2):

$$I = I_0 e^{-\mu \cdot d}, \quad (2)$$

where I is the attenuated intensity, I_0 the primary intensity, d is absorber thickness and μ is the material-dependent linear attenuation coefficient of this object. Figure 14 illustrates 3 different cases.

Case 1: homogeneous object, monochromatic radiation.

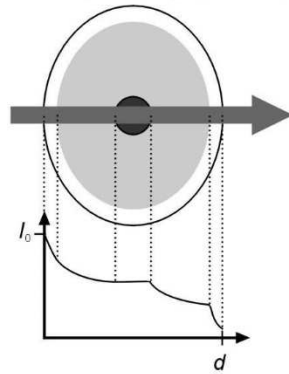


$$I = I_0 \cdot e^{-\mu \cdot d}$$

$$P = \ln \frac{I_0}{I} = \mu \cdot d$$

$$\mu = \frac{1}{d} \cdot \ln \frac{I_0}{I}$$

Case 2: inhomogeneous object, monochromatic radiation.

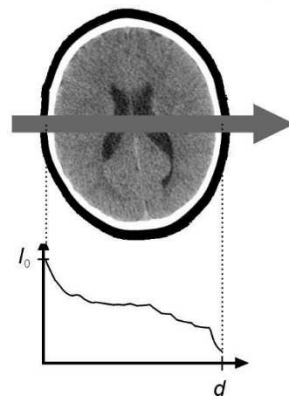


$$I = I_0 \cdot e^{-\mu_1 \cdot d_1 - \mu_2 \cdot d_2 - \mu_3 \cdot d_3 - \dots} = I_0 \cdot e^{-\left[\sum_{i=1}^n \mu_i d_i\right]} = I_0 \cdot e^{-\int_0^d \mu ds}$$

$$P = \ln \frac{I_0}{I} = \sum \mu_i d_i$$

$$\mu_i = ?$$

Case 3: inhomogeneous object, polychromatic radiation.



$$I = \int_0^{E_{\max}} I_0(E) \cdot e^{-\int_0^d \mu(E) ds} dE$$

$$P = \ln \frac{I_0}{I}$$

$$\mu(x, y) = ?$$

KA 2000

Figure 14 - The intensity I of radiation. Three different cases are illustrated, involving homogeneous and inhomogeneous objects, crossed by monoenergetic or polyenergetic X-ray beams. For inhomogeneous objects tomographic imaging is necessary to determine the distribution $\mu(x, y)$. (source: Kalender, 2011⁴).

Case 1 represents the simplest case to be considered, when a monoenergetic narrow beam penetrates a homogeneous object. The intensity fall off exponentially with absorber thickness, and the attenuation, defined as the natural logarithm of primary intensity to attenuated intensity, is simply the product of absorber thickness d and linear attenuation coefficient μ . For a known thickness value, μ can be easily calculated.

Case 2 represents a simple inhomogeneous object crossed by a monoenergetic narrow beam. The attenuation along the radiation path depends on the local linear attenuation coefficient's value μ_i . Summation over the path intervals have to be implemented, with small increments d_i , being expressed as the integral over μ along the total path. Measuring such line integrals is the goal of computed tomography. A two-dimensional distribution of an object characteristic can be determined exactly by an infinite number of linear integrals³², however with a finite number of measurements of the attenuation coefficient distribution $\mu(x,y)$ it is possible to compute an image with good approximation⁴. A single measurement, as in conventional radiography, does not allow the calculation of μ_i in case 2 or any $\mu(x,y)$ distribution.

However, the linear attenuation coefficient μ may depend strongly on energy, and this will influence the measurements in CT, as the X-ray beam is polychromatic. Case 3 represents a real situation: an inhomogeneous object and a polyenergetic beam. The attenuated and the primary intensities are energy dependent, and consequently the linear attenuation coefficient $\mu(E)$ will also depend on the energy. Therefore it is necessary to integrate all over the energy interval, and this is done automatically in modern CT systems⁴.

To compute an image in acceptable quality, applying Radon's theory³², it is necessary to record a sufficient high number of attenuation line integral values. Hence, measurements in multiple directions must be carried out, covering at least 180°, with data points narrowly spaced of each projection.

For simplicity, consider the measurement setup in Figure 15. The X-ray tube, with proper collimation, emits a pencil beam and the detector placed on the opposite side records the intensity, attenuated by the absorber. For a given angular position, the X-ray tube and detector translate linearly, while the intensity is measured either continuously or at single discrete points. It results in intensity profiles recorded for parallel rays. This entire setup rotates around and measures the attenuation profiles for a number of different angular positions⁴.

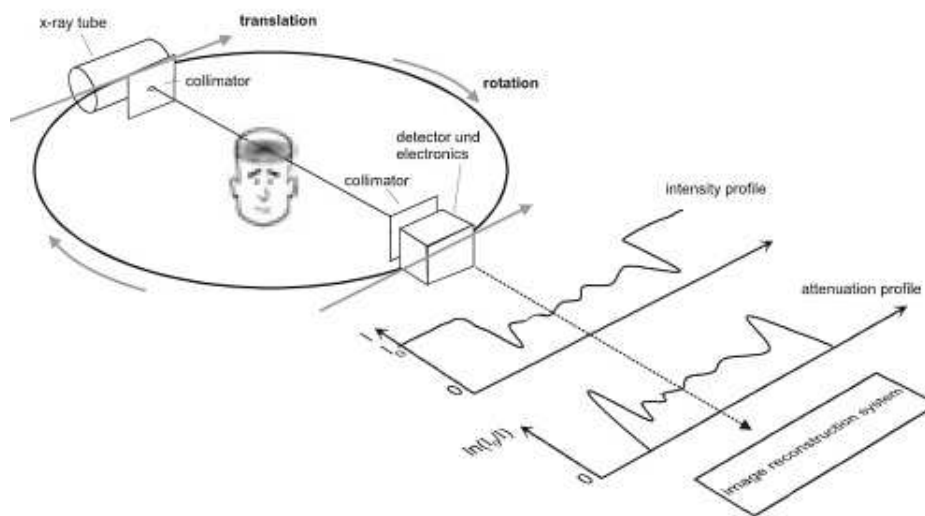


Figure 15 - Simple measurement setup. A collimated radiation source emits a pencil beam, and the detectors placed opposite register the intensity attenuated by the object. For a given angular position, the X-ray tube and detector translate linearly, and this setup rotates around and measures the attenuation for many different angular positions. This is the exact procedure in early CT scanners. (source: Kalender, 2011⁴)

By taking the natural logarithms of the ratio of primary and attenuated intensity, an attenuation profile is obtained, usually known as “projection”. Projections are successively measured for all angular positions. The complete set of projections is transferred to the data processing unit. This procedure was performed in the first clinical CT system, with 180 projections obtained in 1° intervals with 160 points per projection. Modern CT scanners measure typically cone beam geometry, 800-1,500 projections, with 600-1,200 data points per projection, covering 360°. The processing data system now has information about the set of projection values, also termed “Radon Transform”. The distribution of attenuation coefficient $\mu(x,y)$ is yet unknown, and its determination depends on an inverse mathematical transformation⁴.

In early CT systems, the Algebraic Reconstruction Technique (ART) was the most common approach to solve this problem. It considers a $N \times N$ matrix, with N^2 unknown values to be determined by solving N_x independent equations (the measured projections). This is only possible if N_x is equal or greater than N^2 . Then, for a 2×2 matrix, the simplest case of an image matrix, four equations (or projections) are necessary to obtain the $\mu(x,y)$ distribution, which can be easily solved; a 3×3 matrix with nine unknowns can also be easily solved (Figure 16)⁴.

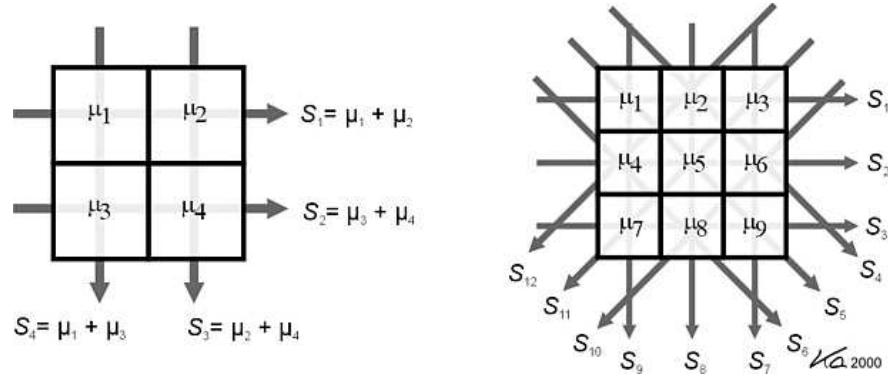


Figure 16 – Algebraic Reconstruction Techniques (ART) is the most easily comprehensible and was the most common approach to image reconstruction. The N^2 unknown values of an $N \times N$ image matrix can be determined by solving a system of linear equations. (source: Kalender, 20114).

Modern CT systems deal with much larger matrices, and the ART became impracticable due to unacceptably high computational time. Another approach is the backprojection, in which an empty matrix (a matrix with pixel values of 0) receives the collected values of each projection along the projection direction as a linear superposition. However this process leads to an unsharp image, as each projection value is added to all pixels along the direction of measurement. To avoid this problem, each projection is convolved with a mathematical function, the so-called convolution kernel (Figure 17). This approach is the most commonly used, and is known as filtered backprojection (FBP) as the convolution acts like high-pass filter (enhancing of high signal frequencies)⁴.

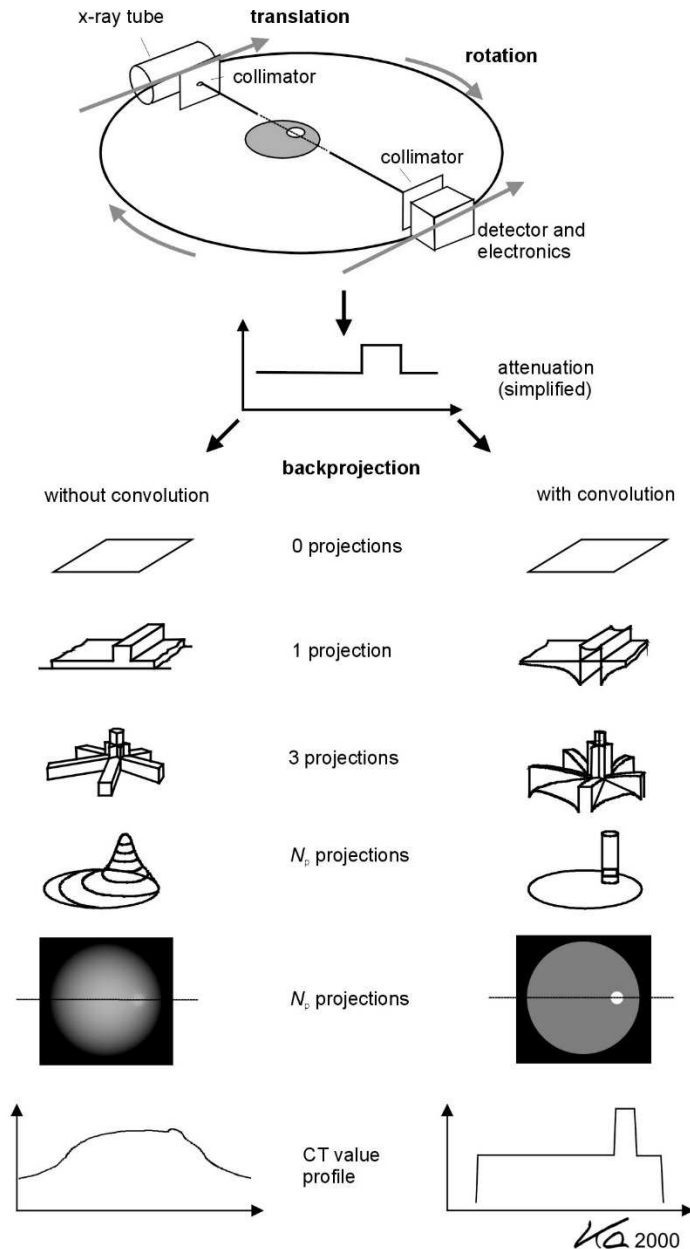


Figure 17 – Backprojection as image reconstruction method, with and without convolution. Backprojection without convolution leads to unsharp images. Convolution before backprojection, essentially as a high pass filtering, counteracts this unsharpening. (source: Kalender, 2011⁴).

Different convolution kernels can be applied to influence image characteristics, from soft or smoothing to sharp and edge enhancement (Figure 18). Smoothing convolution kernels are used for soft tissues visualization, and edge enhancement for high contrast images^{2,4}.

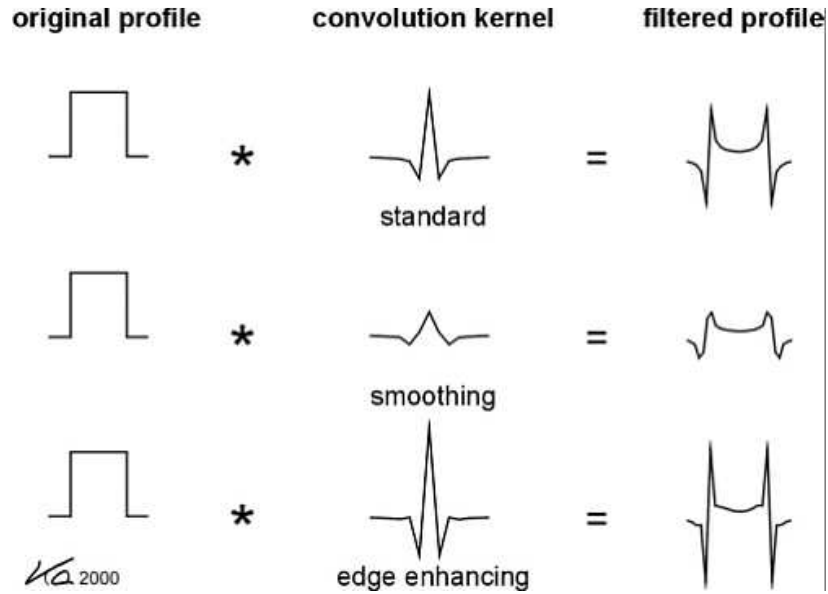


Figure 18 – Different convolution kernels can influence image characteristics. (source: Kalender, 2011⁴).

Another commonly used reconstruction method is the iterative method, which applies repeatedly a mathematical formula to provide closer approximation to the solution of a problem. A series of approximation that is successively closer to the required solution is obtained³³. The iterative method is highly susceptible on noise and the reconstruction times are much longer than FBP methods, being more suitable to PET/CT imaging². However, its application in modern CT equipment is expanding. Cone beam CT technology required the introduction of more sophisticated algorithms for image reconstruction^{34,35}.

1.4.1. Hounsfield Unit

The physical quantity measured by CT, $\mu(x,y)$, is not very descriptive and depends strongly on the spectral energy used. Therefore, a direct comparison of images obtained on different scanners with different voltages and filtrations would be limited⁴.

To overcome this problem, the computed attenuation coefficients for organs and tissues are displayed in values relative to the attenuation of water, so-called CT value or CT number (CTN). For an arbitrary tissue T , with linear attenuation coefficient μ_T the CT number is defined by Equation (3):

$$CTN = \frac{\mu_T - \mu_{water}}{\mu_{water}} \times 1,000, \quad (3)$$

where μ_{water} is the attenuation coefficient for water. In honor of the inventor of CT, CTN is specified in Hounsfield Units (HU). CTN has no upper limit, but for medical scanners they vary from -1000 HU for air until 3000 HU for dense bones⁴.

1.5. CT DOSIMETRY

Studies on development of dosimetric quantities for characterizing CT exposure were initiated in the USA with the introduction of the computed tomography dose index (CTDI)³⁶. CTDI was created to be an index reflecting the average absorbed dose in the central region of a cylindrical phantom, from a series of contiguous irradiation. The term “index” was intentionally included in the CTDI’s name to clearly specify that it is not a direct method for patient dose assessment^{2,37}. Since its introduction, many variations of the original CTDI concept have been proposed, such as CTDI₁₀₀, CTDI_w, CTDI_{vol} and DLP³⁸.

CTDI is measured using a pencil ionization chamber introduced in the central hole of a PMMA cylindrical head phantom (16-cm diameter) or body phantom (32-cm diameter) (Figure 19). It is calculated according to Equation (4),

$$CTDI = \frac{1}{N \cdot T} \int_{-\infty}^{+\infty} D(z) dz, \quad (4)$$

where N is the number of detector rows, T is the detectors width, $N \cdot T$ is the total collimation width and $D(z)$ is the dose profile along z axis.



Figure 19 - PMMA cylindrical head phantom (16-cm diameter, front) or body phantom (32-cm diameter, back). The central and peripheral holes are also showed. (source: Costa, 2015³⁹).

Currently, the measured and calculated quantity is the $CTDI_{100}$, which is the integration of the dose profile along 100 mm. The integration limits would be redefined to ± 50 mm, the reason why most common commercially available pencil type ionization chambers measure 100 mm. For scan lengths longer than 100 mm, $CTDI_{100}$ underestimates the accumulated dose³⁸.

$CTDI_{100}$ is calculated considering that the ionization chamber reading is not directly the integral of dose along z-axis, according to Equation (5),

$$CTDI_{100} = \frac{R_{IC} \times f_{calib} \text{ (mGy)} \times 100 \text{ (mm)}}{N \times T \text{ (mm)}}, \quad (5)$$

where the R_{IC} is the reading of the ionization chamber, the f_{calib} is a calibration factor for conversion of the reading into air kerma units (mGy in this case) and the value 100 is the length of the integral along z-axis in millimeters.

CTDI varies across the field of view (FOV). Another definition of CTDI is the weighted CTDI ($CTDI_w$), which takes into account inhomogeneity of CTDI across the phantom, and provides the average CTDI value¹⁵, defined by Equation (6),

$$CTDI_w = \frac{1}{3}CTDI_{100c} + \frac{2}{3}CTDI_{100p}, \quad (6)$$

where $CTDI_{100C}$ is the $CTDI_{100}$ measured at the center of the phantom and $CTDI_{100P}$ is $CTDI_{100}$ measured at its periphery.

All the previously described quantities do not involve spiral scanning. In order to adapt the metric to helical CT the pitch must be considered, once it defines the gaps or overlaps from the scanning path. The quantity that evaluates this feature from a scan protocol is the volume CTDI ($CTDI_{vol}$), given by Equation (7). For axial scans, pitch value is $p = 1$ and $CTDI_{vol}$ becomes $CTDI_w$.

$$CTDI_{vol} = \frac{CTDI_w}{pitch}. \quad (7)$$

Neither patient size and cross sections nor the length of the scanned volume are taken into account by this metric. To better represent the overall energy delivered by a given protocol, the Dose-Length Product (DLP) can be computed as defined by Equation (8), where L is the scan range³⁸.

$$DLP(mGy.cm) = CTDI_{vol}(mGy) \times L(cm) \quad (8)$$

All commercial scanners must provide $CTDI_{vol}$ and DLP prior to each CT exam, as an indicative of patient dose. The vendors calculated $CTDI_{vol}$ and DLP in standard body (32-cm diameter) and head phantoms (16-cm diameter) and the displayed values depend on the chosen protocol. In general, the head phantom is used to represent head scan protocols and the body phantom is used to represent body scan protocols. For pediatric CT body protocols, some manufacturers use the head phantom and others use the body phantom as the reference to calculate $CTDI_{vol}$ ⁴⁰.

These dosimetric quantities are well established and are widely used. The development on CT technology however have brought the necessity of new different metrics that could take into account the new features and characteristics of new CT scanners⁴¹⁻⁴⁵.

1.5.1. Size Specific Dose Estimates (SSDE)

The interest in patient dose is currently a matter of concern. The correlation between $CTDI_{vol}$ and DLP with patient dose is being questioned, as both of them are defined to a 16-cm diameter and 32-cm diameter reference phantoms and give information regarding scanner output only; patient doses however depend on both

patient size and scanner output⁴⁰. Moreover, patients usually have elliptical anatomy covering a large range of size.

The American Association of Physicists in Medicine (AAPM), through a task group formed by several researchers, has developed a new metric, called Size-Specific Dose Estimate (SSDE) which takes into account the patient's size⁴⁰. Conversion factors were developed to adequate the scanner-displayed $CTDI_{vol}$ to the measured or simulated patient dose. Four different approaches were adopted for evaluating these conversion factors: physical anthropomorphic phantoms, cylindrical PMMA phantoms, Monte Carlo voxelized phantoms and Monte Carlo mathematical cylinders (Figure 20). The conversion factors are based on the patient's/phantom's effective diameter (EF), Equation (9),

$$EF = \sqrt{LAT \times AP}, \quad (9)$$

where LAT is the lateral (side-to-side) dimension of the scanned body and AP is its anterior-posterior dimension. The effective diameter represents the diameter of a circle with area equal to patient cross section's area, at a given location along the z-axis (Figure 21).

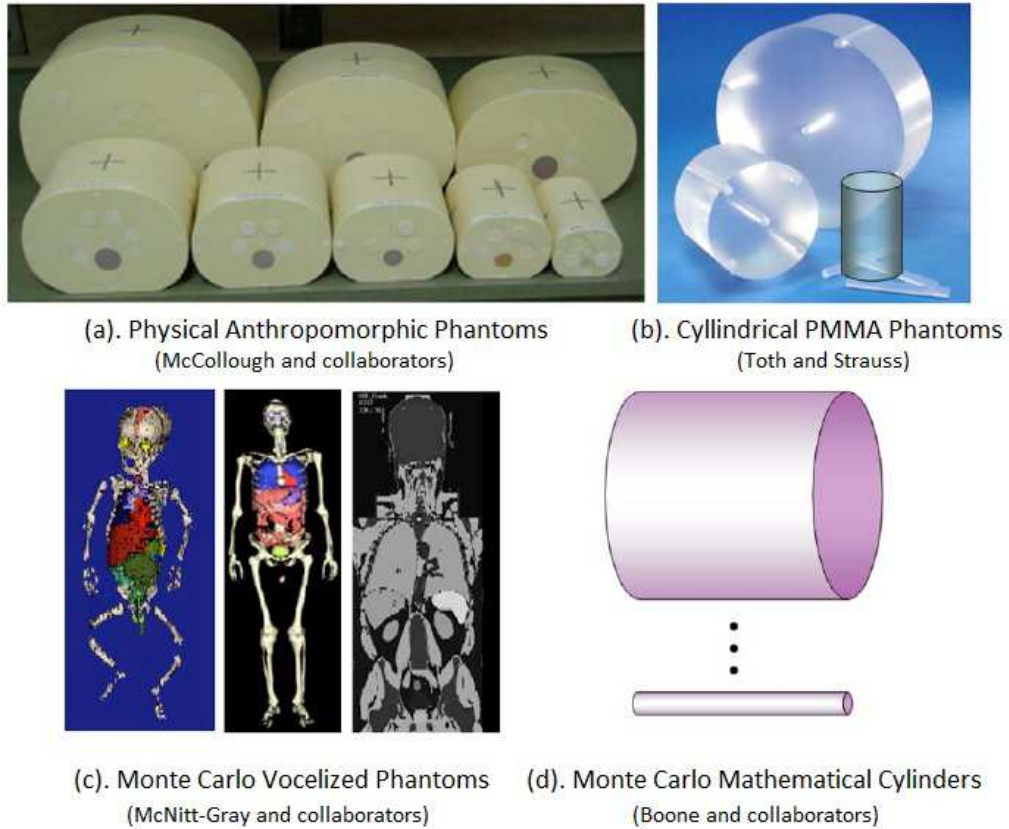


Figure 20 – Different approaches used by four different groups: (a). McCollough and collaborators⁴⁰ performed physical dose measurements using a series of anthropomorphic tissue-equivalent phantoms; (b). Toth and Strauss⁴⁰ used the two reference body and head PMMA phantoms and a third 10 cm diameter phantom; (c). McNitt-Gray and collaborators⁴⁰ performed Monte Carlo dose calculations using anthropomorphic mathematical phantoms and (d). Boone and colleagues⁴⁰ performed Monte Carlo dose calculations on mathematical cylinders with different diameters and compositions. (source: AAPM, 2011⁴⁰).

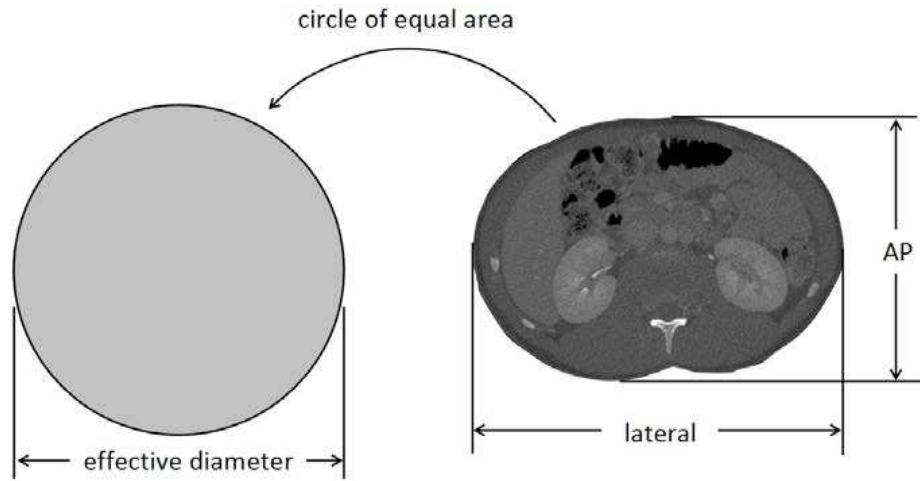


Figure 21 – The anteroposterior (AP) and lateral dimension (LAT), and the effective diameter. The effective diameter represents the diameter of the patient at a given location along the z-axis, assuming that the patient has a circular cross section. (source: AAPM, 2011⁴⁰).

The specific formula to calculate size specific dose estimate for a specific patient size is given by Equation (10) for the 32-cm diameter reference phantom and by Equation (11) for the 16-cm diameter reference phantom.

$$\text{size specific dose estimate} = SSDE = f_{EF}^{32} \times CTDI_{VOL}^{32}, \quad (10)$$

$$\text{size specific dose estimate} = SSDE = f_{EF}^{16} \times CTDI_{VOL}^{16}. \quad (11)$$

f_{EF}^{32} is the conversion factor for a $CTDI_{vol}$ calculated with the 32-cm diameter phantom and for a patient with a specific effective diameter EF, and f_{EF}^{16} is the conversion factor for 16-cm diameter phantom and patient effective diameter EF. Values of f_{EF}^{32} and f_{EF}^{16} are given in ANNEX A.

As an example, for a pediatric patient with $LAT = 12.3$ cm and $AP = 9.9$ cm the effective diameter is $EF = 11$ cm, with reported $CTDI_{vol}$ value of 5.40 mGy for a body reference phantom, the conversion factor is $f_{11}^{16} = 1.22^{40}$. Therefore the size specific dose estimate (SSDE) calculated for this patient is:

$$SSDE = 5.40 \text{ mGy} \times 1.22 = 6.59 \text{ mGy}. \quad (12)$$

1.5.2. Estimation of Organ Dose Values

Even though the CTDI metric and its variants are well established, it is not possible to simply convert any of them into patient absorbed dose. The phantoms

used for CTDI measurements do not represent a human body, neither regarding the geometry nor the material. Furthermore, organs are not taken into account.

To evaluate the risk of radiation exposure due to medical procedures, the radiation dose to individual radiosensitive organs is the preferred quantity to be determined⁴⁶⁻⁴⁸. Organ doses offer specific dose information from a CT examination and allow assessment of potential biological effects of radiation.

Estimation of organ absorbed dose is not a trivial task. Several methods for estimating organ absorbed doses have been introduced in the past decades, they are based in three general approaches: direct measurements with a variety of dosimeters, calculations based on Monte Carlo Methods and biological dosimetry based on blood samples⁴. Each method has its advantages and limitations.

Turner et al⁴⁹ conducted a study to investigate the feasibility of a technique to estimate scanner-independent organ doses, based on the CTDI_{vol} value reported by the scanner console. For that, they simulated four 64-slice scanners, one from each major vendor, including a LightSpeed VCT from GE, with similar configurations to one of the CT scanners used in the present work⁵⁰. The organ dose estimations were performed via Monte Carlo simulations using an adult female voxelized phantom submitted to full body helical scans. The CTDI_{vol} values displayed by the CT equipment may vary for different scanner models, even when similar protocols are performed. This holds true to organ dose estimates. In the case of lung, the results reported from Turner et al⁴⁹ showed that the values of absorbed doses have a coefficient of variation* of 31 %, when similar protocols are performed in similar CT scanner models. To take into account such variations, the authors evaluated the normalization of organ doses to the value of CTDI_{vol} displayed by the consoles. This led to absolute CTDI_{vol}-normalized organ-specific ($nD_{S,O}$) coefficients, which can be used to infer organ absorbed doses from the CTDI_{vol} value reported by any scanner. $nD_{S,O}$ variation for different scanner models is relatively smaller than for absorbed dose values: in the case of lungs, the coefficient of variation was reduced to 4.3 %.

Thorax CT examinations are subject of interest from many researchers⁵¹⁻⁵³ and different methodologies to estimate organ absorbed doses due to such protocols are being developed. Some investigators are interested in evaluating the dose due to

CT procedures for specific populations, such as Peng G. et al.⁵⁴, who performed a study based only in anthropomorphic chest phantom representing Chinese standard men.

Huda et al⁵⁵ proposed a methodology that considers Monte Carlo simulations and the CTDI_{vol} value reported by the scanner console to calculate organ absorbed doses for a 70 kg patient undergoing thorax CT examination. Similarly to Turner et al⁴⁹ study, organ-specific coefficients f_{organ} relating organ dose and CTDI_{vol} were calculated for each tube voltage. Scanners with 1, 4, 16 and 64 slices from two different vendors were analyzed, for X-ray tube voltages ranging from 80-140 kV. This methodology is useful since it relates directly the scanner console presented CTDI_{vol} with an estimation of the dose imparted to specific organs.

The dose imparted from CT examinations is currently a matter of concern especially due to the large number of CT procedures performed nowadays. CT examinations are usually performed using standard protocols available at the scanners. Such protocols could, in principle, be optimized for some situations, aiming dose reduction without compromising the image quality⁵⁶. Current dose optimization strategies include mainly tube current reduction and/or tube current modulation. The first strategy aims to optimize the dose by lowering the tube current to values that still allow diagnostic quality at specific situations. This practice for optimization has been proposed by several researchers⁵⁷.

Poletti et al⁵⁸ classifies abdominal “Low Dose Computed Tomography” (LDCT) as CT protocols with current-time product lower than 30 mAs and absorbed doses comparable to those of a conventional abdomen X-rays . A total of 125 patients with suspected renal colic were submitted to both abdominal LDCT (30 mAs) and standard CT (180 mAs). LDCT and standard CT were independently reviewed by two experienced radiologists for the characterization of renal and ureteral calculi and for indirect sign of renal colic. Their results show that LDCT provides a substantial dose reduction (50 %) and enables the correct diagnostic of renal colic in basis of direct and indirect signs. In addition, the inter-observer agreement was excellent when LDCT images were evaluated by the independent reviewers.

* Coefficient of variation is defined as the ratio of the standard deviation (SD) and the mean value (\bar{M}).

Nagatany Y. et al⁵⁹ studied LDCT and ultra low dose CT (ULDCT) protocols for detection of pulmonary nodules. A total of 83 patients underwent chest CT scans with different values of tube current (240, 120 and 20 mA), and their CT images were analyzed independently by five different radiologists with at least 10 years of experience. They demonstrated that, with the correct reconstruction algorithms, ULDCT protocols could have similar detection performance of solid nodules to LDCT.

Ultra low dose CT (ULDCT) was also studied by Widmann G. et al⁶⁰ for application in computer assisted planning and surgery of midfacial and orbital fractures. They analyzed several protocols with tube current reduction (35, 40, 15 and 10 mA) compared to standard CT protocol (100 mA). As a reference for absorbed dose they used the values of CTDI_{vol} and DLP given by the scanner. The image quality was analyzed by two different consultants (one radiologist and one craniomaxillofacial surgeon), and not all the ULDCT protocols were efficient for diagnostic.

Another option for dose optimization is by using tube current modulation. Modern CT scanners enable the use of tube current modulation through the Automatic Exposure Control (AEC) systems, which can operate with longitudinal and/or angular modulation. Many authors have reported dose reduction efficiency with AEC systems⁶¹⁻⁶³

Papadakis⁶³ published results of an investigation of dose reduction due to tube current modulation in five anthropomorphic phantoms simulating average individual as neonate, 1, 5 and 10-year old child, and adult. AEC was accomplished by means of the CARE Dose 4D implementation integrated in a Somatom Sensation 16 MDCT (Siemens, Erlangen, Germany). Papadakis⁶³ irradiated the phantoms in seven different anatomic regions with AEC protocols based on single AP SPR and single LAT SPR.

1.6. TUBE CURRENT MODULATION (TCM)

With the increase in CT usage, the dose received by patients undergoing such examinations became a matter of concern. In order to keep this radiation dose as low as reasonably achievable (ALARA) without compromising the diagnostic image quality, ongoing efforts toward technique optimization and dose reduction have been

observed, among them the introduction of Automatic Exposure Control (AEC), the use of noise-reduction algorithms and development of new reconstruction algorithms⁶⁴.

As the human body's cross section is significantly different from a circular shape, the attenuation paths of the X-ray beam in CT vary significantly for different angular X-ray tube position, so does the quantum noise. This can lead to a final CT image with inhomogeneous pixel patterns⁶⁵.

Tube Current Modulation (TCM) in CT aims to homogenize noise, by adjusting automatically the X-ray tube current, considering the size and attenuation of the body's region being scanned. These techniques are based on the fact that quantum noise is responsible for the image noise in the X-ray beam projections, and that noise is closely related to image quality⁴. Hence the tube current is modulated according to patient's anatomy to maintain a desired noise level along the entire scan length, with improved radiation dose efficiency^{65,66}.

Currently, two different techniques are used by AEC systems in CT: longitudinal AEC (current modulation along the z-axis) and angular AEC (current modulation in the x-y plane). Both techniques can be combined resulting in different performances in terms of dose savings⁶⁷.

In the longitudinal modulation, the tube current varies along the z-axis using the scan projection radiograph (SPR) as a reference of density and thickness of the imaging object⁶⁶. The system uses the anterior-posterior (AP) SPR or posterior-anterior (PA) SPR. For example, in CT scans covering thorax and abdomen, the system-selected mA value would be relatively low through the thorax region, as it is less attenuating due to the air filled lungs, and higher through the abdomen, which is denser⁶⁸ (Figure 22a).

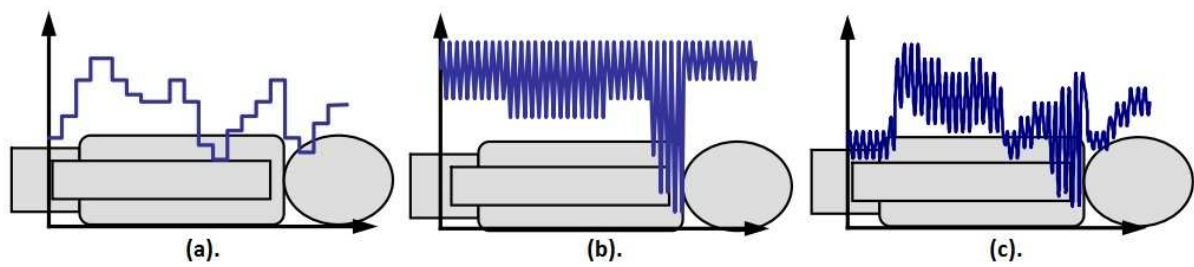


Figure 22 – (a). Longitudinal AEC, with tube current modulation along the z-axis; (b). For Angular AEC, the tube current varies considering the different attenuations in the lateral and AP/PA projections; (c). Combined Longitudinal and Angular AEC. (source: MHRA, 2005⁶⁸).

The angular modulation accounts for the difference in the attenuation between lateral (left-right) and AP/PA projections. The tube current modulation has consequently a sinusoidal behavior, as the X-ray beam attenuation length is much longer for the lateral projection than for the AP/PA, particularly in asymmetric regions of the body as the shoulders or pelvis (Figure 22b). For head scans, where the cross section is closer to circular, less modulation is necessary. Longitudinal and angular modulation modes can be combined to allow the scanner to have optimum exposure at each point during the scan acquisition⁶⁸ (Figure 22c).

1.7. THERMOLUMINESCENT DOSIMETRY

In simple terms, thermoluminescence (TL) is the thermally stimulated emission of light from a crystalline insulator or semiconductor that had previously been excited, typically by exposure to ionizing radiation⁶⁹.

To describe this process in detail, it is helpful to consider the electronic band structure. In the first stage (Figure 23a) the TL material is exposed to ionizing radiation resulting in excitations and ionizations, with electrons being promoted to the conduction band, leaving holes in the valence band. These electrons and holes may become trapped at defects in the crystal lattice, with energies in between the valence and conduction bands.

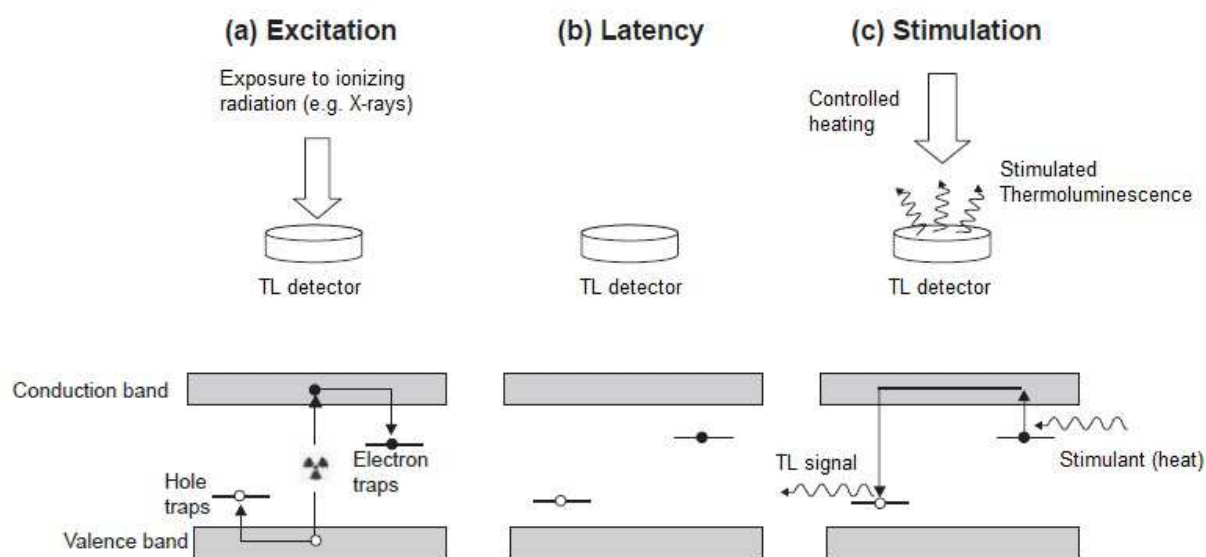


Figure 23 – Different stages involved in the TL process. (a). Excitation of the TL material creating free electrons and holes; (b). Latency period characterized by a metastable concentration of electrons and holes captured at defects in the crystal; (c). Stimulation of the material with controlled heating, leading to recombination of electron-hole pairs and emission of light (TL). (source: Yukihiro; McKeever, 2011⁷⁰, adapted).

After the excitation, the crystal is in a metastable state, characterized by electrons and holes trapped at defects in the crystal lattice (Figure 23b). These trapped electrons and holes can be released by heat, resulting in electron/hole recombination and excitation of luminescence centers in the crystal⁷⁰. When these excited luminescence center decay to the ground state, photons are emitted, and this is the thermoluminescence signal (Figure 23c), which is proportional to the energy deposited during the exposure to ionizing radiation.

Thermoluminescent dosimeters (TLDs) made of a large range of different materials have been used routinely in many dosimetric applications. For patient dosimetry, TLDs of Lithium Fluoride (LiF) are commonly applied. Its effective atomic number (8.14) is similar enough to the effective atomic number of human tissue (7.42) hence eliminating the need for corrections regarding energy dependency in the energy range of diagnostic X-rays⁶⁹.

1.8. ANTHROPOMORPHIC RANDO PHANTOM

Anthropomorphic phantoms constructed with tissue-equivalent materials are widely used to provide a physical representation of the human anatomy⁷¹. They were introduced in radiation protection in medicine aiming to mimic human tissue radiation absorption properties, such as electron density and effective atomic number variations³⁹.

The commercial anthropomorphic RANDO phantom (The Phantom Laboratory, NY, USA) simulates the anatomical characteristics of the Reference Man⁷². It consists of real human skeleton embedded in a soft tissue-equivalent material, with density 0.985 g/cm³ and with effective atomic number (Z_{eff}) of 7.30⁷³. The lungs, molded to fit the contours of the natural rib cage, are composed by a material with the same Z_{eff} as the soft tissue material (7.30), with a density that simulates the median respiratory stage (0.32 g/cm³)^{73,74}. The phantom consists of 36 sections (or slices), numbered from 0 to 35; sections 0 to 34 are 2.5 cm thick and section 35 is the pelvic floor with 9 cm approximately. In every slice, drilled holes enable the introduction of different types of dosimeters. In the present work thermoluminescent dosimeters are introduced in the RANDO phantom to estimate lung mean absorbed dose (Figure 24).



Figure 24 – (a). The slices of the anthropomorphic adult RANDO phantom; (b). The phantom used in the present study, mounted. (source: The Phantom Laboratory, 2012⁷⁴).

The lung distribution inside the phantom body is specified in terms of lung mass fraction f_i contained in each slice i , as showed in Table 3⁷⁵. Since the f_i contribution in slices 10 and 20 are very modest, for the estimation of mean slice absorbed dose their contribution can be added to the adjacent slices⁷⁶.

Table 3 – Lung mass fraction f_i distributed inside each slice i of the adult anthropomorphic RANDO phantom⁷⁵. The sum of slices 10 and 11 will be referred to as slice 11, and the sum of slices 19 and 20 will be called slice 20.

Slice i	f_i
11 (10 + 11)	0.06
12	0.09
13	0.11
14	0.14
15	0.14
16	0.13
17	0.13
18	0.11
20 (19 + 20)	0.09

2. MATERIALS AND METHODS

2.1. THERMOLUMINESCENT DOSIMETERS (TLD)

Lithium Fluoride (LiF) thermoluminescent dosimeters (TLD), in the format of 3 x 3 x 1 mm³ chips of LiF doped with Magnesium and Titanium (LiF: Mg, Ti) (TLD-100, Harshaw Chemical Company, OH, USA) were used in the present work.

2.1.1. TLD Data Reading

After irradiated, the TL's information need to be extracted from the dosimeters. A TL/OSL reader Risø model DA-20 (DTU Nutech. Inc., Rødkilde, Denmark) was used to read the information on the TLDs. This equipment has a sample carousel with 48 stainless steel cups that are individually heated according to a pre-set configuration (Figure 25). For the present work, the equipment was set to heat the dosimeters from 0 °C to 350 °C at a constant rate of 10 °C/s.



Figure 25 – TL/OSL reader Risø (DTU Nutech. Inc., Rødkilde, Denmark) (left) and its Carousel with 48 stainless steel cups (right).

A coupled photomultiplier tube (PMT), with a blue filter, captures the light emitted by the TLDs⁷⁷. The collected light signal is converted into a digital signal and is presented to the user as a plot of counts per temperature, called a TL curve (Figure 26). These data can be exported to ASCII files.

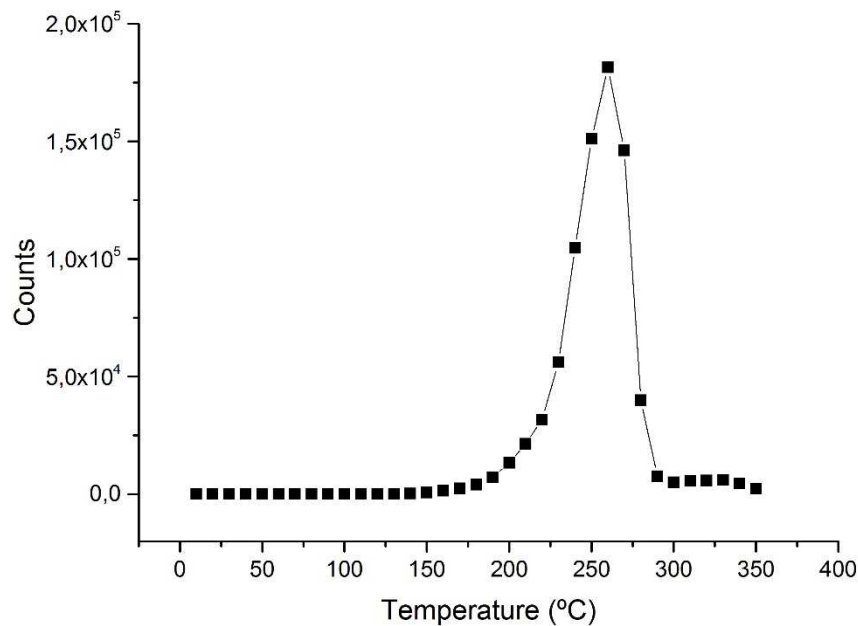


Figure 26 – An example of a TL curve for a LiF TLD (TLD-100, Harshaw Chemical Company, OH, USA). Dosimeter data from the Risø TL/OSL reader, presented to the user in counts per temperature in Celsius degree. The TL peak is around 250 °C.

Each TLD curve is numerically integrated using the plotting and data analysis software Origin® (OriginLab Co., MA, USA), converting the TLD curve signal into one single value correspondent to the area under the entire curve (Figure 26). This area is directly proportional to the energy deposited by the radiation in the dosimeter. This will be referred to as “TL value”.

2.1.2. TLD Group Selection

To evaluate the precision on dose response of a group of TLD it is necessary to determine the response variation when this group is irradiated with the same dose. 640 TLDs (TLD-100) were introduced in a PMMA holder drilled with 900 holes (30 x 30) (Figure 27a), so that the TLDs could be easily accommodated with a specific location. Then the PMMA holder was irradiated with 2.190 mGy using a ⁶⁰Co source (Figure 27b). The TLDs were read according to the methodology previously described.

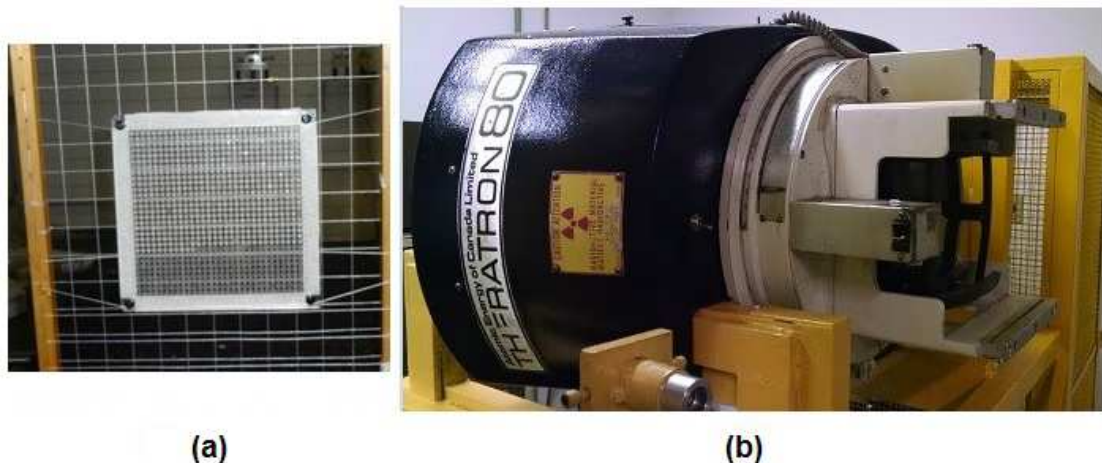


Figure 27 – (a). The PMMA holder with 680 TLDs positioned to irradiation. (b). Theratron® Teletherapy (Best Theratronics Ltd., ON, Canada) containing a ^{60}Co source.

The TLD response was evaluated by calculating the mean TL value and its standard deviation (SD). Dosimeters whose TL values were within the interval of one standard deviation (SD), mean value ± 1 SD, were selected. Using this criteria, 481 TLDs were selected to be used for all phantom irradiations performed in the present work. Coefficient of variation[†] for the selected group is approximately 6.5 %.

2.1.3. Annealing

To erasing any effects of previous irradiations, thermoluminescent materials need to undergo a thermal treatment, called annealing⁷⁸. Before each irradiation, the TLDs were placed inside an aluminum recipient and thermally treated, as follows⁷⁹:

- 60 minutes in a muffle kept at constant temperature of 400 °C;
- 10 minutes cooling at room temperature over a copper block;
- 120 minutes in a muffle kept at constant temperature of 100 °C;
- Cooling at room temperature.

2.1.4. TLD Holders

Dosimeter holders were specially designed for this project. The TLD holders were projected and manufactured at the Mechanical Workshop of the Institute of Physics from the University of São Paulo. The TLD holders were designed to fit the holes inside the RANDO phantom and to accommodate up to five TLD chips. Each

[†] Coefficient of variation is defined as the ratio of the standard deviation (SD) and the mean value (\bar{M}).

dosimeter holder can accommodate up to five TLD chips so that, when inserted in the phantom slice, the chips are placed in the midsection⁷³. The TLD holders and the technical draft are showed by are shower in Figure 28.

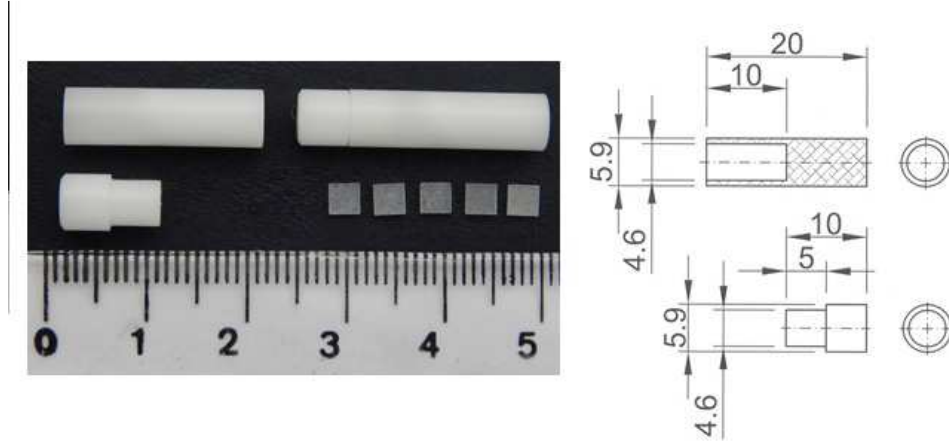


Figure 28 – TLD holders (left) positioned next to TLDs and a scale; Technical draft in mm (right) of the Thermoluminescent dosimeter holder, specially designed to be used in this study.

The material used to manufacture the TLD holders should have an effective atomic number similar to the effective atomic number of the RANDO phantom, Z_{eff} . Nylon 6 and Polyoxymethylene are materials that can be easily purchased, with reasonable price and good machining properties. To determine the most suitable material, the effective atomic number Z_{eff} of Nylon 6 and Polyoxymethylene were calculated, considering Equation (13)⁸⁰.

$$Z_{eff} = \sqrt[m]{a_1 Z_1^m + a_2 Z_2^m + \dots} \quad (13)$$

where a_i represents the fraction of the total number of electrons associated with each element, Z_i is the atomic number of each element, A_i is the atomic mass of each element and w_i is the mass fraction of each element that composes the material. a_i can be calculated with Equation (14):

$$a_i = w_i \frac{Z_i/A_i}{\sum w_i \frac{Z_i}{A_i}} \quad (14)$$

The composition of each material was obtained in the database from the National Institute of Standards and Technology (NIST)⁸¹, and is shown in Table 4. The same table also shows the respective values of Z_{eff} .

Table 4 – Compounds of Nylon 6 and Polyoxymethylene, with corresponding mass fraction and effective atomic number.

Nylon 6		Polyoxymethylene	
Z_i	w_i	Z_i	w_i
1 (H)	0.097976	1 (H)	0.067135
6 (C)	0.636856	6 (C)	0.400017
7 (N)	0.123779	8 (O)	0.532848
8 (O)	0.141389	-	-
$Z_{eff} = 6.21$		$Z_{eff} = 7.03$	

Polyoxymethylene has an effective atomic number (7.03) closer to the effective atomic number of the RANDO Phantom (7.30), when compared to Nylon 6. Therefore, the dosimeter holders were produced using Polyoxymethylene.

2.1.5. TLD Calibration

The TLDs were calibrated for X-ray beam quality RQT 9, which corresponds generally to the reference radiation quality for CT⁸², in order to correlate the TL information with the dosimetric quantity Air Kerma (K_{AIR}). Five groups of five TLDs were irradiated with an X-ray tube (MCN 421, Philips, Germany), for five different tube current-time product (mAs) values, at a distance correspondent to the patient-source distance for a CT scanner. Another group was used for measuring background radiation. A 30 cc ionization chamber (IC) (Cylinder Stem Ionization Chamber Type 23361, PTW, Freiburg, Germany) was positioned close to the TLD groups and the air kerma in every irradiation was registered to comparison with the TLDs readings. The TLDs were read following the methodology previously described, and the value for background radiation was subtracted from all 5 groups.

To convert the IC readings into K_{AIR} , some correction factors must be applied⁸², as follows in Equation (15):

$$K_{AIR} = M_Q \cdot N_{k,Q_0} \cdot k_{TP} \cdot k_{Q,Q_0}, \quad (15)$$

where M_Q is the IC reading (in Coulombs) for a X-ray beam quality Q , N_{k,Q_0} is the calibration coefficient given by the IC calibration report, k_{Q,Q_0} is the correction factor for a radiation beam quality Q regarding the calibration beam quality Q_0 , and k_{TP} is the correction factor for temperature and pressure. k_{TP} is given by⁸²:

$$k_{TP} = \left(\frac{273,2 + T}{273,2 + T_0} \right) \left(\frac{P_0}{P} \right), \quad (16)$$

where $T_0 = 20.0$ °C is the reference temperature and $P_0 = 101.3$ kPa is the reference pressure. $T = 25.2$ °C and $P = 93.5$ kPa were the temperature and pressure at the moment of irradiation, respectively. Therefore, $k_{TP} = 1.103(13)$. The uncertainties on temperature, pressure and N_{k,Q_0} values are based on the guidance on uncertainty levels achievable, proposed by the International Atomic Energy Agency⁸². This document illustrates the uncertainty estimations for different realistic scenarios. For the present work, scenario 1 was considered.

In the calibration laboratory, the IC was calibrated using a RQR 5 X-ray beam quality, which corresponds to radiation quality generally used in conventional radiology, and against RQA 5 beam, which corresponds to radiation condition after attenuation by a patient in conventional radiography⁸². Calibration factors are determined for different beam qualities, however the certificate of calibration gives no information regarding RQT beams.

The RQT 9 beam has a half value layer (HVL) of 8.4 mm of Aluminum (Al)⁸². To determine which RQR or RQA beam, for available calibration factors, best approximates an RQT 9 beam it is convenient to analyze their HVL values: the closer the HVL value, the closer are the effective beam energies and the better RQT 9 is approximated. RQA 7 is the most suitable radiation beam quality in these circumstances. Therefore $k_{Q,Q_0} = k_{RQA7,RQA5} = 1.01 \pm 0.05$. Table 5 summarizes all adopted correction factors.

Table 5 – Correction and calibration factors for the 30 cc ionizing chamber.

$N_{k,Q_0}(\text{Gy/C})$	k_{TP}	k_{Q,Q_0}
9.129×10^5	1.103	1,01

2.2. SELECTION OF CT SCANNING PROTOCOLS

The present project was developed in a partnership between the Group of Radiation Dosimetry and Medical Physics (*Grupo de Dosimetria das Radiações e Física Médica*) and two major public hospitals: Institute of Radiology from the Medical Faculty from the University of São Paulo (*Instituto de Radiologia do Hospital das Clínicas da Faculdade de Medicina da Universidade de São Paulo – InRad*) and the Cancer Institute of the State of São Paulo Octávio Frias de Oliveira (*Instituto do Câncer do Estado de São Paulo Octávio Frias de Oliveira – ICESP*)[‡]. All the CT scanners from both institutions are submitted regularly to a Quality Assurance program[§].

Absorbed lung doses for CT procedures performed in the aforementioned hospitals were estimated in the present work. As a first step, it was necessary to define the protocols to be studied and the starting point was to investigate the variety and frequency of all CT scan protocols performed in both institutions. This investigation was done by using information from the Picture Archiving and Communication System/Radiology Information System (PACS/RIS) from both hospitals. For ICESP information concerning the year of 2012 was available, while for InRad the PACS/RIS information from 2012 to 2014 was analyzed.

2.3. LUNG DOSE ESTIMATION

Each TLD irradiated was read by the TL/OSL reader Risø model DA-20 (DTU Nutech. Inc., Rødkilde, Denmark) following the methodology described previously, and the value for background radiation was subtracted from all groups.

In order to convert the information extracted from the TLDs, here referred to as “TL value”, to lung absorbed dose some calculations must be carried out. First, the TL value must be converted into K_{AIR} , using the calibration previously described. For each slice i a mean value of K_{AIR} (K_{AIR}^i) is calculated, as shown in Equation (17)⁸³,

[‡] Avaliação de doses ocupacionais, estimativa de doses em pacientes adultos e pediátricos e avaliação da eficiência de sistemas AEC em tomografia computadorizada. Protocolo de Pesquisa No. 018/14.

[§] Quality Assurance performed by the Quality Assurance Team from the Institute of Physics of the University of São Paulo.

where G is the total number of TLD groups in slice i and σ_n^2 is the variance of the TL values from TLDs in group n .

$$K_{AIR}^i = \frac{\sum_{n=1}^G (K_{AIR}^n / \sigma_n^2)}{\sum_{n=1}^G (1 / \sigma_n^2)}. \quad (17)$$

Then, K_{AIR}^i needs to be converted to lung average absorbed dose in the organ fraction present at slice i , D_i , according to⁸⁴:

$$D_i = K_{AIR}^i \frac{(\mu/\rho)_{Lung}^{en}}{(\mu/\rho)_{Air}^{en}}, \quad (18)$$

where $(\mu/\rho)_{Lung}^{en}$ and $(\mu/\rho)_{Air}^{en}$ are the mass energy-absorption coefficients for lung and air, respectively.

To calculate $(\mu/\rho)_{Lung}^{en}$ and $(\mu/\rho)_{Air}^{en}$, it is necessary to determine the effective energy (E_{eff}) of a radiation beam with quality RQT 9. E_{eff} of a polyenergetic beam is equivalent to the energy of a monoenergetic beam having the same half value layer (HVL)⁸⁰. The HVL for a radiation beam with energy E_{eff} can be defined as:

$$HVL = \frac{\ln 2}{\mu(E_{eff})}, \quad (19)$$

where μ is the linear attenuation coefficient. Rewriting Equation (19), considering the aluminum's density $(\rho)_{Al}$ leads to an expression for the mass energy-absorption coefficient:

$$\left(\frac{\mu}{\rho}\right)_{Al} = \frac{\ln 2}{(\rho)_{Al} \times HVL}, \quad (20)$$

The HVL for a beam with quality RQT 9 is $HVL_{RQT9} = 0.84\text{cm}$ of aluminum⁸². Therefore, it is possible to calculate the mass energy-absorption coefficient in aluminum for a beam with the effective energy of a RQT 9 beam, being $(\rho)_{Al} = 2.712\text{ g/cm}^3$:

$$\left(\frac{\mu}{\rho}\right)_{(E_{eff})_{Al}} = \frac{\ln 2}{2.712 \times 0.84} = 0.30 \frac{\text{cm}^2}{\text{g}}. \quad (21)$$

The National Institute of Standards and Technology (NIST, USA) provides information regarding mass attenuation coefficient for a variety of elements, mixtures and compounds⁸⁵. It is possible to determine the E_{eff} in Equation (21) by identifying in NIST's database the beam energy correspondent to the calculated mass attenuation coefficient in aluminum $(\mu/\rho) = 0.30 \text{ cm}^2/\text{g}$. Therefore, the effective energy for a RQT 9 beam is approximately 56.3 keV.

The mass attenuation coefficient for lung and air can be determined by using NIST database⁸⁵, considering a beam with energy of 56.3 keV and the composition of lung tissue and air⁸⁶ (Table 6). The obtained values are $(\mu/\rho)_{Lung}^{en} = 0.0363 \text{ cm}^2/\text{g}$ $(\mu/\rho)_{Air}^{en} = 0.0337 \text{ cm}^2/\text{g}$.

Table 6 – Lung tissue and air composition. These information were used at NIST database in order to calculate lung and air mass energy-absorption coefficients for lung and air.

Lung Tissue (ICRU 44)^{85,87}		Air (near sea level)⁸⁶	
Z	% (by weight)	Z	% (by weight)
1 (H)	0.103000	6 (C)	0.000124
6 (C)	0.105000	7 (N)	0.755268
7 (N)	0.031000	8 (O)	0.231781
8 (O)	0.749000	18 (Ar)	0.012827
11 (Na)	0.002000		
15 (P)	0.002000		
16 (S)	0.003000		
17 (Cl)	0.003000		
19 (K)	0.002000		

All the information necessary to obtain the lung average absorbed dose in the each lung slice is now available. Hence the mean absorbed dose for the entire lung can be estimated by summing up the contributions regarding each slice⁷⁵:

$$D = \sum f_i \times D_i \quad (22)$$

2.4. EFFECTIVE DIAMETER

With the increasing interest in patient dosimetry, new metrics that take into account patient size are being developed, as is the case of Size Specific Dose

Estimate (SSDE). The present work investigated whether the SSDE can be directly correlated to lung absorbed doses.

To calculate the SSDE for the studied protocols, it is necessary to measure the effective diameter of the RANDO phantom utilized in all irradiations. To determine the effective diameter, the AP and LAT dimensions of the patient must be known.

The LAT dimension can be assessed using electronic clippers on a standard AP SPR, which is acquired in most cases prior to a CT scan. In the same way, the AP dimension can be assessed using a LAT SPR. If such radiographs are not available, it is possible to measure these quantities with physical clippers⁴⁰. In the case of a RANDO phantom, such values can be measured in using a measuring tape and the correspondent phantom slice.

For this project, the AP and LAT dimensions were measured directly with the phantom slice and virtually using the SPR performed prior to the total body CT protocol. The armpit position of the phantom was chosen as a reference point. For the virtual assessment, AP and LAT dimensions were measured using the DICOM viewer software JiveX® (VISUS Technology Transfer GmbH, Germany) (Figure 29). The measurement tool at JiveX® is set manually. To estimate possible user-dependent uncertainties from JiveX®, five different co-workers measured AP and LAT dimensions, resulting in five different AP and LAT values. The average and the standard deviation (σ) were calculated (Table 7). For AP and LAT measurements performed directly with the phantom slice, the uncertainty corresponds to the smaller scale of the measuring instrument.

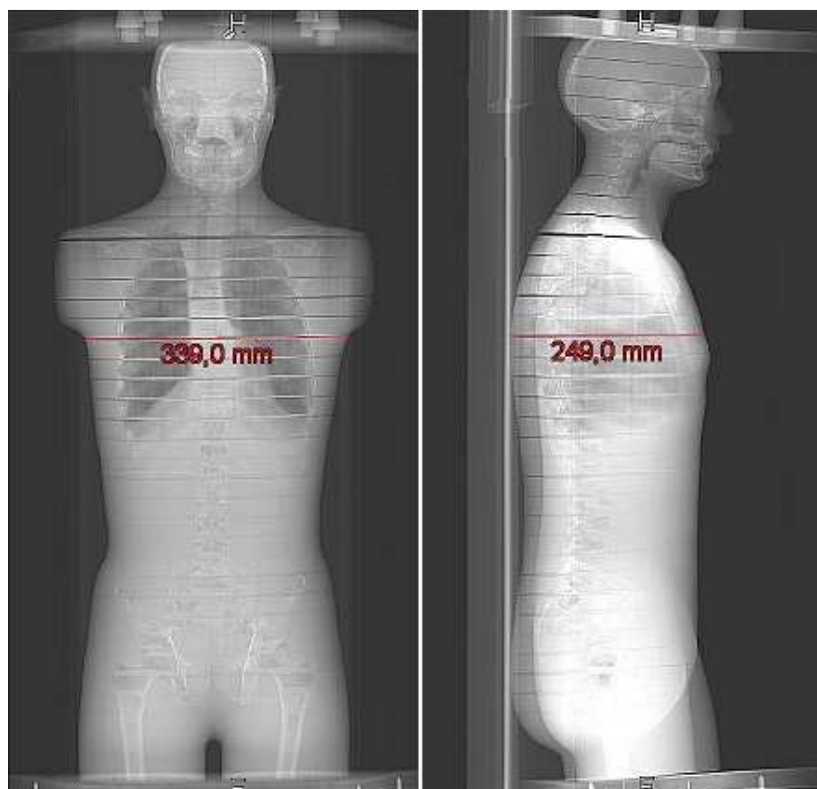


Figure 29 – Lateral (LAT) and anteroposterior (AP) dimensions of the adult RANDO phantom, measured using JiveX®.

Table 7 – Anteroposterior (AP) and lateral (LAT) dimensions of the adult RANDO phantom, measured virtually using the SPR scans and directly with the phantom slice. Five co-workers measured five different values for each quantity in order to estimate user-dependent uncertainties derived from JiveX®.

User	AP (cm)	LAT (cm)
1	24.90	33.82
2	24.77	33.86
3	24.87	34.00
4	24.88	33.91
5	24.90	33.90
Direct measurement	22.4(0.1)	34.5(0.1)

2.5. PHANTOM IRRADIATION

The phantom was irradiated using seven different protocols: one protocol for total body CT, three protocols for thorax CT with fixed mA, two protocols for thorax using AEC systems and one double SPR (AP and LAT). Figure 30 represents a scheme of the studied protocols. A Discovery PET/CT 690 scanner (GE Healthcare,

OH, USA) was used for the total body CT protocol^{**}; all the others irradiations were performed with a GE Discovery CT 750 HD (GE Healthcare, OH, USA).

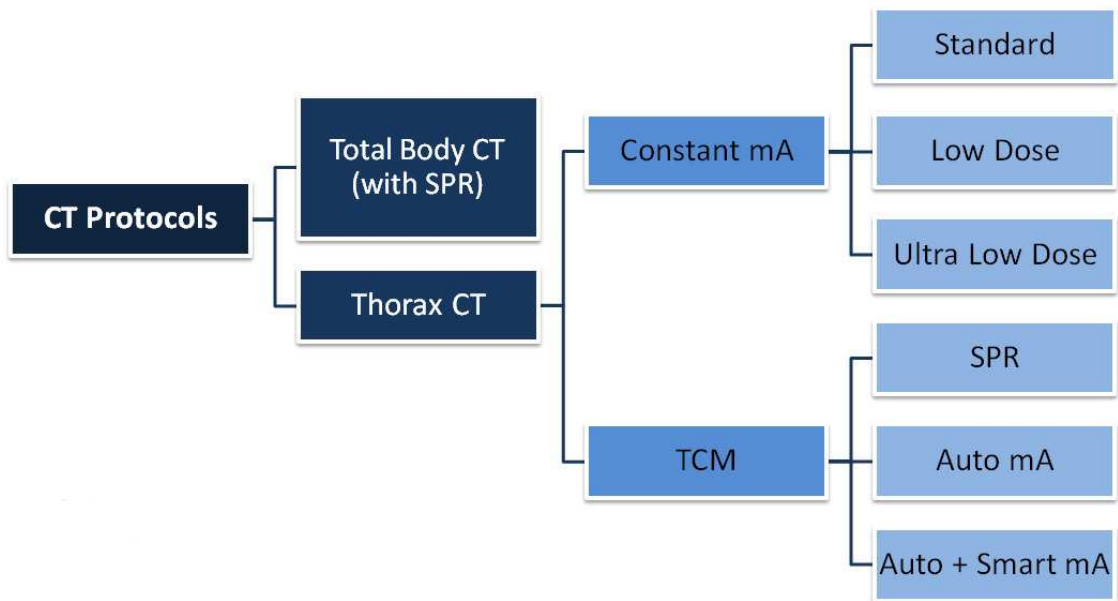


Figure 30 – Seven CT protocols used for phantom irradiation: one protocol of total body CT with double SPR, three thorax protocols with constant tube current, two protocols with tube current modulation and a double SPR of the thorax.

2.5.1. Total Body Protocol

The total body protocol was the first one performed, and it was essential to determine phantom positioning, as well as positioning of TLD holders inside it. With this irradiation it became possible to determine visually where and how the lung is distributed.

The lung is distributed inside the RANDO Phantom along slices 10 to 20, with different total mass fractions (f_i)⁷⁵. For mean dose calculations, the contribution of f_i from slices 10 and 20 can be added to adjacent slices (Table 3). Therefore, 14 groups of 5 LiF TLDs were inserted inside the phantom in positions correspondent to the lung distribution inside slices 11 to 19 (Table 8). By the time of this irradiation, only 15 TLD holders were ready to use, what justifies the small number of TLD groups. Slice 15 was chosen to receive 6 groups, as it is the slice with the greatest lung mass fraction, together with slice 14. One TLD group was employed to measure

^{**} The chosen protocols were clinical diagnostic CT protocols and not attenuation correction protocols used in PET/CT procedures.

background radiation, which was later subtracted from the signal obtained with all other TLD groups.

Table 8 – TLD groups distributed inside the RANDO Phantom for a total body protocol, and corresponding lung total mass fraction.

Slice i	f_i^{75}	# Groups
11	0.06	1
12	0.09	1
13	0.11	1
14	0.14	1
15	0.14	6
16	0.13	1
17	0.13	1
18	0.11	1
19	0.09	1

Figure 31 illustrates the distribution of six TLD groups inside phantom slice 15 for the total body irradiation.

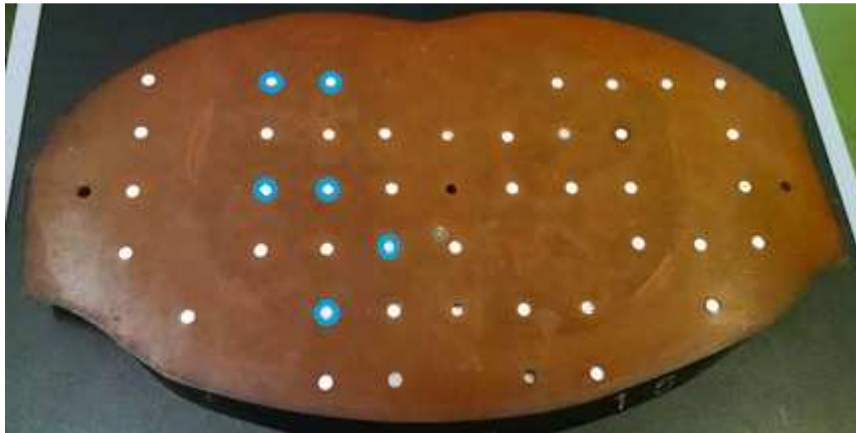


Figure 31 – Six groups of TLDs (in blue) distributed inside phantom slice 15 for irradiation with the total body protocol.

The phantom was positioned in the isocenter of a Discovery PET/CT 690 scanner (GE Healthcare, OH, USA). As many protocols utilize a scan projection radiograph (SPR), a double SPR (AP and LAT) was performed with 50mA and 120kV (Figure 9). The parameters used for total body protocol are listed in Table 9, as well as the $CTDI_{vol}$ and DLP values given by the scanner. The mAs is defined as product of the tube current (mA) and the tube rotation time (s), while mAs_{eff} is the mAs value divided by the pitch (p)⁶³.

Table 9 – Parameters for the phantom irradiation with a Total Body CT protocol. The values for CTDI_{vol} and DLP displayed by the scanner are also shown.

Voltage (kV)	120
Tube current (mA)	300
Tube current-time product (mAs)	300
Effective tube current-time product (mAs_{eff})	304.9
Rotation Time (s)	1
Pitch	0.984
Collimation (mm)	40
N x T	64 x 0.625
CTDI_{vol} (mGy)	25.17
DLP (mGy.cm)	2550.71
Scan Range L (cm)	101.3

2.5.2. Scan Projection Radiograph (SPR)

Aiming to estimate the radiation dose absorbed by the lungs during scan projection radiographs (SPR), forty groups of 3 TLDs were inserted inside the RANDO Phantom and irradiated in a GE Discovery CT 750 HD (GE Healthcare, OH, USA), for AP and LAT projections of the thorax. The groups were distributed according to lung positioning (Table 10); this configuration was also used for all thorax protocols. Background radiation was measured with one group of 3 TLDs and the corresponding TL value was discounted from the TL values correspondent to irradiated groups. Scanner parameters were 120 kV for tube voltage and 10 mA for tube current.

Table 10 - TLD groups distributed inside the RANDO Phantom for SPR and thorax protocols, and corresponding lung total mass fraction.

Slice i	f_i^{75}	# Groups
11	0.06	2
12	0.09	2
13	0.11	6
14	0.14	6
15	0.14	8
16	0.13	6
17	0.13	4
18	0.11	4
19	0.09	2

2.5.3. Thorax Protocols

Lung absorbed doses due to five different protocols for Thorax CT have been investigated: three protocols with constant tube current (mA) and two protocols using tube current modulation through AEC systems. For all five protocols the phantom was irradiated in a GE Discovery CT 750 HD (GE Healthcare, OH, USA).

Constant Tube Current

Three different protocols with constant tube current (mA) were investigated, here identified as “Standard”, “Low Dose” and “Ultra Low Dose”. The protocol “Standard” refers to the protocol typically used for thorax scans. The “Low Dose” and “Ultra Low Dose” are two new thorax protocols proposed by a team of radiologists from InRad which seek to reduce the dose received by the patient without compromising the image diagnostic quality. No SPR was performed prior to these irradiations.

Table 11 shows acquisition parameters for the three protocols. The phantom was irradiated from slice 9 to 24, hence covering entire lung region. Forty groups of 3 LiF TLDs were distributed inside the phantom according to Table 10; one group was selected to measure background radiation.

Table 11 - Parameters for the phantom irradiation with Standard, Low Dose and Ultra Low Dose CT protocols. The equipment-given values for CTDI_{vol} and DLP are also shown.

	Standard	Low Dose	Ultra Low Dose
Voltage (kV)	120	120	120
Tube current (mA)	300	120	40
Tube current-time product (mAs)	180	48	16
Effective tube current-time product (mAs_{eff})	130.9	34.9	11.6
Rotation Time (s)	0.6	0.4	0.4
Pitch	1.375	1.375	1.375
Collimation (mm)	40	40	40
N x T	64 x 0.625	64 x 0.625	64 x 0.625
CTDI_{vol} (mGy)	10.03	2.76	0.92
DLP (mGy.cm)	465.90	128.52	42.81
Scan Range L (cm)	46.5	46.6	46.5

Tube current modulation (TCM)

Two thorax irradiations were performed using scanner's AEC systems. For the first irradiation, "Auto mA" mode was selected, which is how GE denominates AEC with longitudinal tube current modulation. The second irradiation was performed in the "Auto + Smart mA" mode, the AEC with longitudinal and angular modulations combined. The angular modulation in GE scanners can only be selected in combination with the longitudinal modulation⁶⁷. For reference of the phantom's density and anatomy double scan projection radiographs (SPR), AP and LAT projections, were acquired.

Table 12 shows acquisition parameters for both protocols. The phantom was irradiated from slice 9 to 24, hence covering entire lung region. Forty groups of 3 LiF TLDs were distributed inside the phantom according to Table 10; one group was selected to measure background radiation.

Table 12 - Parameters for the phantom irradiation with Auto mA and Auto + Smart mA CT protocols. The equipment-given values for CTDI_{vol} and DLP are also shown.

	Auto mA	Auto + Smart mA
Voltage (kV)	120	120
Tube current (mA)	80 - 300	80 - 300
Tube current-time product (mAs)	48-180	48-180
Rotation Time (s)	0.6	0.6
Pitch	1.375	1.375
Collimation (mm)	40	40
N x T	64 x 0.625	64 x 0.625
CTDI_{vol} (mGy)	6.61	5.59
DLP (mGy.cm)	306.96	259.49
Scan Range L (cm)	46.4	46.4

3. RESULTS

This chapter is divided in four main topics, directly associated with the methodology described in Chapter 2: results concerning TLD calibration, selection of the CT scanning protocols to be used for phantom irradiation, phantom's effective diameter and estimation of lung absorbed doses. The uncertainties, represented by the values in parenthesis, were estimated according to the methodology described in ANNEX B. The confidence level considered is 68.3%

3.1. TLD CALIBRATION

Using the values given in Table 5 and Equation (15), it is possible to convert the IC readings into K_{AIR} . The K_{AIR} values were associated to the TL values for each 5 different irradiations (Table 13).

Table 13 – Values of K_{AIR} (mGy) and TL values, for TLD groups irradiated with different mAs with a radiation beam quality RQT 9.

TLD Group	1	2	3	4	5
Tube current-time product (mAs)	50	100	200	300	400
K_{AIR} (mGy)	1.4(1)	2.8(2)	5.7(4)	8.5(6)	11.4(8)
TL Value (10^5)	0.70(6)	1.4(4)	3.0(2)	4.1(3)	5.4(1)

Finally, a linear fit was performed using the data presented in Table 13 (Equation 23). It was used the plotting and data analysis software Origin 8® (OriginLab Co., MA, USA), relating TL Value to air kerma in mGy (Figure 32). Intercept value was set zero and slope value is $2.00(5) \times 10^{-5}$. This calibration will be used to convert all TLD information due to CT irradiation into air kerma.

$$K_{AIR} = 2.00 \times 10^{-5} \times (\text{TL Value}). \quad (23)$$

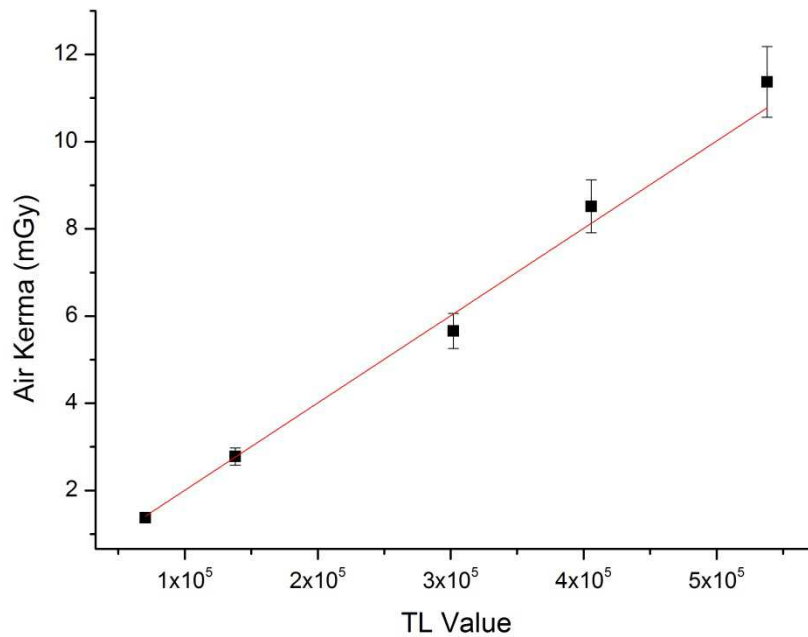


Figure 32 – Calibration curve for TLDs, relating TL values to Air Kerma. Intercept value was set zero and slope value is $2.00(5) \times 10^{-5}$ ($R^2 = 0.997$).

3.2. SELECTION OF CT SCANNING PROTOCOLS

Information from the Picture Archiving and Communication System/Radiology Information System (PACS/RIS) from both hospitals was used to verify that 65 different CT protocols are available at ICESP and 83 are available at InRad. During 2012, over 64,000 CT scanners were performed at ICESP for adult patients; for InRad this number exceeds 67,000. The five most frequent CT protocols at each institution were determined, and are shown in Figure 33 and Figure 34, respectively for ICESP and InRad.

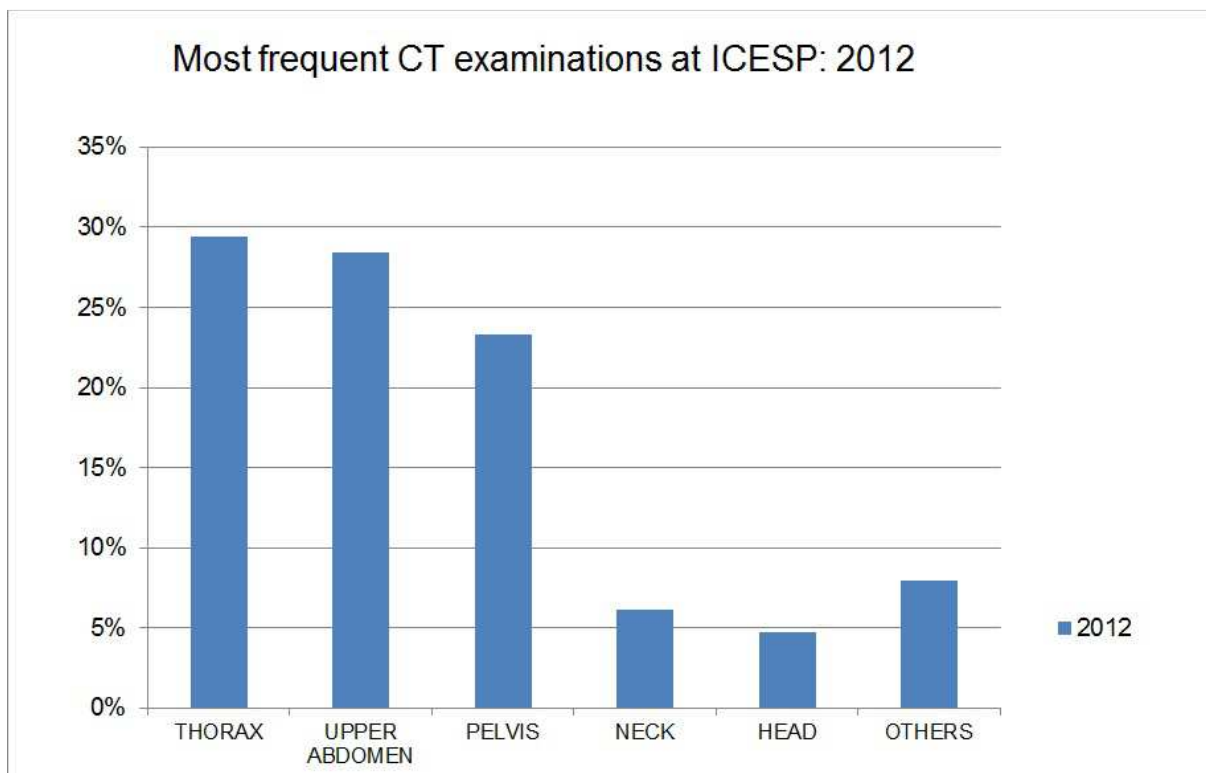


Figure 33 – Most frequent CT examinations at ICESP during 2012. CT of thorax represented almost 30% of all CT scans performed in that year.

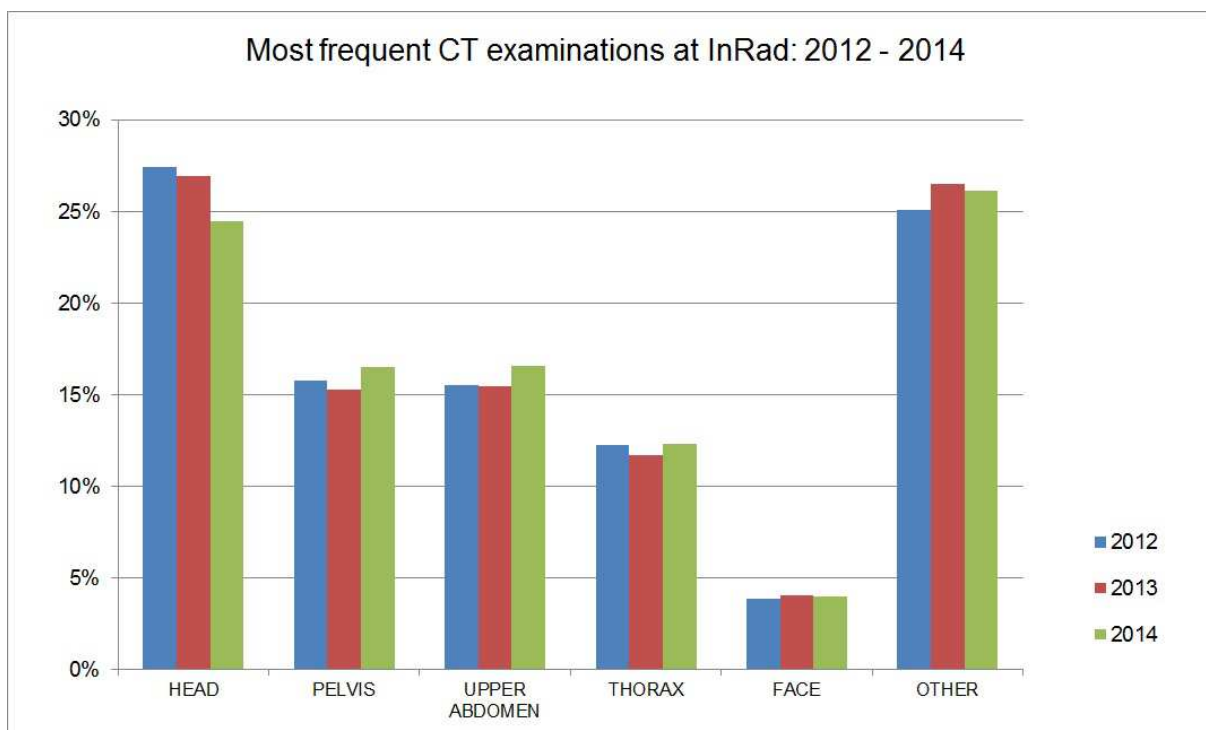


Figure 34 - Most frequent CT examinations at InRad from 2012 - 2014. CT of thorax represented around 13 % of CT scans performed in the evaluated period, being the fourth most frequent CT procedure.

As Figure 33 and Figure 34 show, Thorax CT protocol is among the top 5 examinations during the evaluated period for both hospitals. During Thorax CT scans the lungs are entirely irradiated. Therefore it is relevant to determine the dose absorbed by the lungs during Thorax CT examinations and, if possible, to propose optimized acquisition protocols that could lead to dose reduction maintaining clinical image quality.

Lung absorbed doses due to a total body CT protocol and a SPR protocol were also investigated in the present work. Total body irradiation was the first studied protocol, and it was essential to determine phantom positioning, as well as TLD location inside it. As SPR are widely performed in clinical procedures, it is relevant to estimate the radiation dose absorbed by the lungs during such procedures.

3.3.EFFECTIVE DIAMETER

From the information given in Table 7 the average values and standard deviation for AP and LAT dimensions of a RANDO Phantom are calculated and presented in Table 14.

Table 14 – Average value and standard deviation for a RANDO Phantom's anteroposterior (AP) and lateral (LAT) dimensions. Calculated values for the effective diameter (EF) are also shown.

Virtual Measurement	AP (cm)	LAT (cm)
Average (cm)	24.86	33.90
σ (cm)	0.05	0.07
EF	29.03(4)	
Direct measurement	AP (cm)	LAT (cm)
Average (cm)	22.4	34.5
σ (cm)	0.1	0.1
EF	27.8(1)	

Using Equation (9) and the average AP and LAT dimensions (Table 14) the effective diameter (EF) is then calculate to be $EF = 29.03(4)\text{cm}$ for the virtual measurement and $EF = 27.8(1)\text{cm}$ for the direct measurement. The conversion factor for $EF = 29\text{cm}$ is $f_{29}^{32} = 1.28^{40}$, while for $EF = 28\text{cm}$ is $f_{28}^{32} = 1.32^{40}$, considering the $CTDI_{vol}$ calculated for a 32 cm diameter PMMA phantom. As the difference between

the conversion factors are of only 3 %, the results considering the virtual assessment of the EF will be used in the present work.

3.4. ESTIMATION OF LUNG ABSORBED DOSE

Lung absorbed doses in the adult anthropomorphic phantom, irradiated with seven different CT protocols, were estimated by the methodology previously described.

3.4.1. Total Body Protocol

The total body protocol was the first protocol to be studied, and it was useful to determine phantom and TLD positioning. With 40 groups of TLDs distributed inside the lung region of a RANDO phantom, following the methodology described previously, the lung mean absorbed dose due to a double SPR followed by a total body CT scan was estimated, as well as further dosimetric quantities (dose/mAs, dose/mAs_{eff}, scanner-given CTDI_{vol}, DLP values and SSDE), presented in Table 15.

Table 15 – Lung absorbed dose and further dosimetric quantities for total body CT protocol.

Total Body Protocol	
CTDI_{vol} (mGy)	25.17
DLP (mGy.cm)	2550.72
Dose/mAs (mGy/mAs)	0.146(4)
Dose/mAs_{eff} (mGy/Aseff)	0.146(4)
Dose (mGy)	43.9(1.3)
SSDE (mGy)	32.29

3.4.2. Scan Projection Radiograph (SPR)

SPR are performed prior to the exam for orientation over patient anatomy and positioning. With the introduction of AEC systems, SPRs are being widely performed once they also serve as a reference of a patient's density and thickness for the AEC systems. Even though the imparted dose due to such irradiation is expected to be considerably smaller than for a CT procedure, it is relevant to estimate its value.

Forty groups of 3 TLDs were distributed inside the lung of the RANDO phantom and irradiated for AP and LAT projections of the thorax. The lung mean absorbed dose due to both SPR is estimated in 0.192(4) mGy. Other dosimetric quantities do not apply in the case of SPR acquisitions.

3.4.3. Thorax Protocols

Constant Tube Current

Three different Thorax protocols with constant tube current were investigated, here denominated “Standard”, “Low Dose” and “Ultra Low Dose”. The “Standard” protocol corresponds to the protocol typically performed at InRad for thorax scans. Aiming to reduce the absorbed dose without compromising image quality, the “Low Dose” and “Ultra Low Dose” protocols were proposed by a team of radiologists from InRad. Both proposed protocols seek to reduce the dose by reducing the scanner’s tube current, when compared to the value used for “Standard”: “Low Dose” sets a tube current value of 120 mA, while protocol “Ultra Low Dose” sets an even lower value of 40 mA. Estimation of lung absorbed doses for such protocols, as well as further dosimetric quantities, are presented in Table 16.

Table 16 - Lung absorbed doses and further dosimetric quantities for all thorax protocols with constant tube current: “Standard”, “Low Dose” and “Ultra Low Dose”. Aiming to reduce patient absorbed dose without compromising image quality, “Low Dose” and “Ultra Low Dose” protocols were proposed by a team of radiologists. For the three protocols, the voltage value set for irradiation was 120 kV.

	Standard	Low Dose	Ultra Low Dose
CTDI_{vol} (mGy)	10.03	2.76	0.92
DLP (mGy.cm)	465.90	128.52	42.81
Dose/mAs (mGy/mAs)	0.0794(9)	0.081(1)	0.078(1)
Dose/mAs_{eff} (mGy/mAs_{eff})	0.109(1)	0.111(1)	0.107(2)
Dose (mGy)	14.3(2)	3.88(5)	1.24(2)
SSDE (mGy)	12.87	3.54	1.18

As expected, the estimated lung absorbed dose is directly proportional to the mAs value set to each CT protocol⁸⁸.

Tube current modulation (TCM)

Two irradiations were performed using protocols with AEC mode on, applying longitudinal tube current modulation (“Auto mA”) and both longitudinal and angular modulation combined (“Auto + Smart mA”). The angular modulation in GE scanners can only be selected in combination with the longitudinal modulation⁶⁷. Table 17 presents lung absorbed doses due to both protocols, as well as further dosimetric quantities and the tube current range employed during the scan. Doses referable to double SPR acquisitions are accounted in the estimated values.

Table 17 - Lung absorbed doses and further dosimetric quantities for all thorax protocols with tube current modulation: “Auto mA”, which modulates the tube current only in longitudinal direction, and “Auto + Smart mA”, which combines longitudinal and angular modulations.

	Auto mA	Auto + Smart mA
CTDI_{vol} (mGy)	6.53	5.51
DLP (mGy.cm)	306.96	259.49
Dose (mGy)	11.9(1)	9.29(8)
SSDE (mGy)	8.38	7.07

Table 18 summarizes the estimated lung absorbed doses and further dosimetric quantities for all CT protocols investigated in the present work.

Table 18 – Summary of lung absorbed doses, and further dosimetric quantities, due to all 7 scan protocols investigated.

	Thorax - Constant tube current					Thorax -Tube Current Modulation/AEC	
	Total Body	SPR	Standard	Low Dose	Ultra Low Dose	Auto mA	Auto + Smart mA
Tube current (mA)	300	10	300	120	40	80-300	80-300
CTDIvol (mGy)	25.17	-	10.03	2.76	0.92	6.53	5.51
DLP (mGy.cm)	2550.72	-	465.90	128.52	42.81	306.96	259.49
Dose/mAs (mGy/mAs)	0.146(4)	-	0.0794(9)	0.081(1)	0.078(1)	-	-
Dose/mAseff (mGy/mAseff)	0.146(4)	-	0.109(1)	0.111(1)	0.107(2)	-	-
Dose (mGy)	43.9(13)	0.192(4)	14.3(2)	3.88(5)	1.24(2)	11.9(1)	9.29(8)
SSDE (mGy)	32.29	-	12.87	3.54	1.18	8.38	7.07

4. DISCUSSION

The present work proposes a methodology to determine lung absorbed doses in an anthropomorphic adult RANDO Phantom, with the use of thermoluminescent dosimeters, for seven different CT clinical protocols: one total body protocol, one SPR protocol, three thorax protocols with constant tube current and two thorax protocols with tube current modulation. Such protocols were selected after analysis of the data from the Picture Archiving and Communication System/Radiology Information System (PACS/RIS) from ICESP and InRad.

A correlation between the estimated lung absorbed dose values and SSDE, a recently proposed patient-specific metric, was investigated. Such correlation could enable practical lung dose estimation in clinical routine.

4.1. SELECTION OF CT SCANNING PROTOCOLS

Data evaluation from the PACS/RIS showed that 65 different protocols are available for CT examinations at ICESP, where over 64,000 CT scans were performed in adult patients in the year of 2012. Thorax CT protocols correspond to 29.4 % of the total number of CT examinations performed, being the most performed CT protocols during this period, followed by Upper Abdomen CT (28.5 %), Pelvis CT (23.3 %), Neck CT (6.2 %) and Head CT (4.7 %). A predominance of examinations in the Thorax-Abdomen-Pelvis area is observed. This can be justified by the fact that ICESP is a public institution designated to treat oncologic patients, and by the fact that the majority of the tumors are distributed in the aforementioned regions of the body^{89,90}.

At InRad 83 different CT protocols are available where over 67,600 CT examinations were performed in adult patients in 2012 and 2013. This value increased to 71,611 in 2014, a raise of approximately 6 %. For the same lapse of time, the most frequent CT protocol is Head CT (27.5 %, 27.0 % and 24.5 % in 2012, 2013 and 2014, respectively), followed by Pelvis CT, Upper Abdomen CT and finally Thorax CT. Thorax CT protocols corresponded to 12.3 % of the total adult CT examinations performed in 2012; a small decrease to 11.7 % was observed in 2014, with a subsequent increase to 12.4 % in 2014.

A significant amount of thorax CT examination was performed from 2012 to 2014 in both institutions. During such imaging procedures the lungs are entirely irradiated being therefore relevant to determine the absorbed dose by this organ during thorax CT examinations. This type of protocol was chosen to be the main subject of interest of the present study.

4.2. ESTIMATION OF LUNG ABSORBED DOSE

In the past decades many researchers have been investigating new methodologies to estimate organ doses⁹¹⁻⁹³. Some proposals are based on calculations using Monte Carlo methods, while others rely in experimental phantom or in vivo measurements with different dosimetric techniques. The present work describes a methodology to estimate lung absorbed doses for an anthropomorphic adult RANDO phantom submitted to seven different CT protocols, using LiF thermoluminescent dosimeters (TLD).

4.2.1. *Total Body Protocol*

As a first step the phantom was irradiated with a total body CT protocol, in a Discovery PET/CT 690 scanner (GE Healthcare, OH, USA) from the Cancer Institute of the State of São Paulo Octávio Frias de Oliveira (ICESP). The total body irradiation provided knowledge of correct placement of the phantom inside the CT scanner, as well as detailed information regarding the lung tissue distribution inside its anatomy. Such information was used to distribute uniformly the TLD holders inside the lung, serving as a guide to all further irradiations.

Although the total body and all the thorax protocols were set to operate at the same tube voltage (120 kV), the lung absorbed dose estimation for the total body protocol was at least 3 times higher than the value estimated for the thorax examinations. In the case of “Standard Thorax” even the tube current setting was the same (300 mA). This can be explained by the pitch values selected: for the total body protocol, a smaller pitch value was selected when compared to the thorax protocols. Besides, larger amount of scattered radiation is produced during the total body scan, as it was set to irradiate the phantom completely from slices 0 to 35, while for the thorax protocols the phantom was irradiated from slices 9 to 24.

Considering the methodology proposed by Turner et al⁴⁹, with $nD_{S,O}$ for the lungs being 1.77(8), and the CTDI_{vol} value of 25.17 mGy, reported by the scanner for the total body irradiation studied in the present work (Table 18), the lung absorbed dose is estimated to be 44.6(2.0) mGy, presenting an excellent agreement to the value of 43.9(1.3) mGy estimated with TLDs. Despite the differences in the CT scanner model and the phantom type, the lung absorbed dose value due to a total body protocol estimated by the present study is compatible to this similar study. The value of 43.9(1.3) mGy includes contribution from double SPR, performed prior to irradiation, but such contributions are significantly small, as will be discussed in the following section.

4.2.2. Scan Projection Radiographs

Scan projection radiographs (SPR), also called topogram, scout and surviw depending on the vendor, are performed prior to CT examinations. They provide information regarding patient's anatomy and positioning, being extremely useful for the radiologists and technologists to define the volume of diagnostic interest and to set the parameters to be used for the exam. This digital radiograph image, mostly taken in AP, PA and/or LAT projections, is acquired with stationary configuration of the X-ray tube and detector arrays, with the patient being transported through the radiation field.

With the advent of tube current modulation (TCM) systems, SPR became widely performed once TCM protocols use the resulting SPR images as a reference of patient's attenuation and thickness, in order to vary the tube current along the scanning direction.

Although SPR became an essential step prior to CT scans, there are not many published studies in the literature involving dosimetric aspects of the SPR scans. In the 1990s Mini et al⁹⁴ investigated the dose absorbed by several organs due to one single protocol of SPR and also due to standard thorax, abdomen and pelvis protocols performed at their institution. The results for the dose absorbed by the lungs due to a thorax SPR and thorax CT protocol are 0.18 mGy and 17.6 mGy respectively. Even though Mini et al⁹⁴ do not specify in which projection the SPR was taken and neither the scanner used, it was shown that the dose due to such procedure is relatively small, when compared to the other studied protocols.

In the present work the dose absorbed by the lungs due to a double SPR (LAT and AP) was estimated to be 0.192(4) mGy, which is in good agreement with the estimation from Mini et al⁹⁴. This estimation corresponds to about 1.3 % of the dose absorbed by the lungs due to a standard thorax protocol. This fraction increases to 4.9 % and 15 % when compared to the “Low Dose” and “Ultra Low Dose” thorax protocols. For “Auto mA” and “Auto + Smart mA” this contribution is 1.6 % and 2.1 %, respectively. Therefore SPR contributes with relatively low doses to the lungs, when compared to standard thorax protocols. For protocols aiming dose reduction its contribution may become significant.

4.2.3. *Thorax Protocols*

During 2012 and 2014 thorax CT protocols have been among the top five most performed CT examinations in both ICESP and InRad. For such clinical procedure the lungs are entirely irradiated. Moreover, the RANDO Phantom anatomic characteristics allow the lungs to be easily identified through CT images and even conventional chest radiographs. Five different thorax CT protocols were analyzed during the present work, regarding the dose imparted by the lungs.

Along with the estimation of lung absorbed doses due to the standard thorax CT protocol, performed at InRad, the dose due to two new thorax CT protocols are also estimated. Such protocols seek dose optimization by lowering the tube current to values that still allow diagnostic quality at specific situations.

Dose optimization can also be achieved by tube current modulation. In modern CT scanners, tube current modulation is enable via the Automatic Exposure Control (AEC) systems. For the equipment analyzed, a GE Discovery CT 750 HD (GE Healthcare, OH, USA), the available AEC modes are “Auto mA” and “Auto + Smart mA”. “Auto mA” utilizes only longitudinal modulation, while “Auto + Smart mA” combines longitudinal with angular modulation. The angular modulation at GE scanners can only be enabled associated with the longitudinal mode⁶⁷.

Constant mA

Three different protocols with constant tube current (mA) were selected to study. The “Standard” protocol corresponds to the protocol commonly used at InRad

for any thorax CT examination, while “Low Dose” and “Ultra Low Dose” are two new optimized protocols proposed by a team of radiologists who seek dose reduction by lowering the tube current value.

According to the National Lung Screening Trial Research Team from the U.S. Department of Health and Human Services, thorax low dose CT correspond to CT examinations with tube current-time product equal or lower than 40 mAs and effective dose of 1.5 mSv for the standard man⁹⁵. The current-time product value for the “Low Dose” protocol adopted in the present work is 48 mAs, very close to the aforementioned definition. The concept for thorax ultra low dose CT is not yet well established, but the goal is to acquire CT images with doses comparable to a thorax AP + LAT conventional radiography⁹⁶.

For the protocols analyzed in the present study the proposed reduction in the tube current-time product was of 73.3 % for the “Low Dose” thorax CT and 91.1 % for the “Ultra Low Dose”, in comparison to the standard protocol. The estimated lung doses also followed this pattern, being 72.9(8) % smaller for the “Low Dose” thorax CT and 91(1) % smaller for the “Ultra Low Dose”, again compared to the standard protocol (Table 16). As expected, the reduction in the mAs value leads to a proportional reduction in the imparted dose⁸⁸.

According to Table 16 the lung absorbed dose for the “Ultra Low Dose” protocol was estimated to be 1.24(2) mGy, a value more than 5 times greater than the estimated value of 0.24(11) mGy obtained by Freitas⁹⁷ for the double thorax AP + LAT radiography. Despite the undoubtedly significant dose reduction achieved with the proposed “Ultra Low Dose” protocol, it is not yet as low as the dose due to conventional AP + LAT X-ray of the thorax, pursued by the definition of thorax ULDCT⁹⁶. This can be explained by issues related to image quality, once the team of radiologists from InRad could no longer obtain a CT image with diagnostic quality with lower mAs values⁹⁸.

Although the scanners used in the present work are from different models than the scanner used by Huda et al⁵⁵, it is possible to compare the estimated organ doses resulted from both studies, due to similarities among the CT scanners and clinical protocols⁵⁰. In the case of lungs irradiated with a protocol set to operate in 120 kV, the coefficient for organ estimation proposed by Huda et al⁵⁵ is $f_{lung} = 1.50(6)$.

For the standard protocol, the value of dose per mAs_{eff} , $0.108(1) \text{ mGy/mAs}_{\text{eff}}$ is comparable to the $0.143(6) \text{ mGy/mAs}_{\text{eff}}$ reported by Huda et al⁵⁵. The dose/ mAs estimate from the standard protocol, $0.0803(9) \text{ mGy/mAs}$, is also comparable to value of 0.088 mGy/mAs reported by Sabarudin et al⁹⁹ for TLD measurements of thoracic CT. Moreover, the dose estimation obtained for the “Standard” thorax protocol is compatible with results published by other authors in literature¹⁰⁰.

In principle f_{lung} is valid for any thorax CT performed at any CT scan with tube current set to 120 kV for a 70 kg adult. Taking into account the CTDI_{vol} values from the protocols studied here, the lung absorbed doses may be estimated using the methodology from Huda et al⁵⁵. Table 19 shows the results.

Table 19 – Lung absorbed doses due to the Standard, Low Dose and Ultra Low Dose thorax CT protocols estimated by the present work (with TLD measurements) and by the methodology proposed by Huda et al⁵⁵.

	Standard	Low Dose	Ultra Low Dose
Dose by TLD measurements (mGy)	14.3(2)	3.88(5)	1.24(2)
CTDI_{vol} (mGy)	10.03	2.76	0.92
Dose by Huda et al ⁵⁵ (mGy)	15.0(6)	4.1(2)	1.38(6)
Relative Difference (%)	4.7(4.0)	5.4(4.8)	10.1(4.1)

With exception of the “Ultra Low Dose” protocol, the dose estimates from the present study are in excellent agreement with the estimation performed using the methodology from Huda et al⁵⁵.

Tube current modulation

AEC systems also provide dose reduction by adapting the tube current according to patient anatomy and attenuation properties. In the present study two different AEC modes were analyzed, regarding the dose imparted by the lungs: “Auto mA”, which corresponds to tube current modulation along the z axis of the patient (the longitudinal direction), and “Auto + Smart mA” which combines longitudinal with angular modulation. GE scanners only allow the angular modulation to be used when associated to the longitudinal mode⁶⁷.

For both AEC modes the tube current range was set to rely between 80 – 300 mA, and tube current-time product being 48 – 180 mAs, with tube voltage of 120 kV. For reference, the equipment used double SPR (LAT and AP).

From the results presented in Table 17, the dose reduction achieved with “Auto mA” mode was of 16.8(1.3) % compared to the “Standard” protocol with tube current fixed at 300 mA (180 mAs); the reduction was 35.0(1.2) % for the “Auto + Smart mA” mode. The contribution from the double SPR performed prior to irradiation are accounted in the dose values displayed by Table 17, however as shown in section 3.4.2. the dose contribution due to SPRs are relatively small.

Dose reduction achieved with the proposed protocols “Low Dose” and “Ultra Low Dose” thorax CT are more significant. This can be justified by the tube current range of 80 – 300 mA set to both AEC protocols: even though the scanner used tube current modulation, in some regions of the body the mA value could be as high as the value set for the “Standard” protocol, while for the “Low Dose” and “Ultra Low Dose” the maximum – and only – value available was 120 and 40 mA respectively. Moreover, the minimum value of 80 mA is higher than the value set for the “Ultra Low Dose” protocol. The range of tube current values, within which the systems may operate, is defined by the operator. The range of 80 – 300 mA, set in the present study, corresponds to the standard protocol commonly used at InRad for clinical protocols using TCM. In order to optimize the dose reduction achieved with tube current modulation, a comprehensive investigation on image quality with different tube current ranges for AEC shall be performed.

Another factor that may contribute for dose reduction with AEC system is the anatomic region to be scanned. Some regions of the phantom anatomy present more irregularities than others, such as the shoulders and the pelvis, where the inhomogeneity occurs due to both patient geometry and X-ray attenuation path. Dose reduction achieved with tube current modulation could be more efficient when applied to abdomen-pelvis protocols for example.

For chest CT examinations, Papadakis⁶³ reported dose reductions of 15.5(2.1) % and 15.0(1.0) % were reported for AP-based AEC and LAT-based AEC, respectively. Dose reduction was calculated as the percentage difference of the mean modulated and the preset tube current-product that is prescribed for standard fixed-mA head and body scan protocols. Despite the differences in CT scanner and protocol, the dose reduction of 16.8(1.3) % achieved with the “Auto mA” AEC mode in the present study is in good agreement with the results reported by Papadakis⁶³.

4.3. COMPARISON TO IMPACT SPREADSHEETS

The Monte Carlo simulation method has been reported as a reliable way to obtain accurate organ dose distributions within a human body due to CT scans. Phantoms with anthropomorphic characteristics can be fully simulated with Monte Carlo, as well as the peculiarities from different models of CT scanners^{92,101,102}. Moreover, graphical user interface-based softwares have been developed for Monte Carlo organ and effective dose estimations, such as CT-Expo¹⁰³ and ImPACT spreadsheets (ImPACT CT Patient Dosimetry Calculator)¹⁰⁴ among others. Those softwares are mostly based on two well established organ dose database: the National Radiation Protection Board (NRPB)¹⁰⁵ and the National Research Center for Environment and Health (*Gesellschaft für Strahlen und Umweltforschung mbH - GSF*)^{106,107}. The NRPB was based on a hermaphrodite adult stylized phantom while the GSF was based on male and female stylized phantoms, as well as two pediatric phantoms⁵³.

Lung absorbed doses were estimated using the ImPACT Spreadsheets. These estimations were performed by two collaborators: Prof. Dr. Michael McNitt-Gray (University of California, Los Angeles) and Dr. Isabel Ana Castellano (The Royal Marsden NHS Foundation Trust) for four studied protocols: Total body, Standard Thorax, Low Dose Thorax and Ultra Low Dose Thorax. The exact same parameters of the irradiation were used for the simulations, but the scan range could have been different due to different landmarks available in the hermaphrodite phantom. Protocols with tube current modulation are not available on this software. Estimations have been performed for a GE LightSpeed VCT scanner (GE Healthcare, X, USA), available in the spreadsheets. Although the scanner model is not the same as the one used to irradiate the RANDO phantom, comparisons of the experimentally estimated and simulated lung doses are possible due to similarities among the equipment.

Table 20 shows the results obtained with the ImPACT spreadsheets, as well as the dose estimated with TLDs. Lung dose values obtained by ImPACT spreadsheet are overestimated compared to those experimentally estimated with TLDs. The MC calculated value is around 2 % higher for the “Total Body” protocol. This difference increases for the thorax protocols, being around 25 %, 22 % and

27 % higher for the “Standard”, “Low Dose” and “Ultra Low Dose” protocols, respectively. Such behavior could be due to the different CT scanner used for simulation and/or the fact that the ImPACT spreadsheet’s organ dose calculations are based in a hermaphrodite phantom; differences on the scan range could also have contributed.

Table 20 – Lung dose values estimated with TLDs and with Monte Carlo Simulations. The values simulated with Monte Carlo overestimate the lung absorbed dose, when compared to the experimental results obtained with TLDs. This can be due to discrepancies in CT scanner model, phantom model and scan range.

	Total Body	Standard	Low Dose	Ultra Low Dose
Dose (mGy) – TLD	43.9(1.3)	14.3(2)	3.88(5)	1.24(2)
Dose (mGy) – ImPACT	45	19	5	1.7
Relative difference (%)	2	25	22	27

4.4. CORRELATION BETWEEN ORGAN DOSE AND SSDE

CTDI in its original formulation became inappropriate due to news technologies developed for CT. Therefore new metrics for CT dose quantification are being developed, as is the case of Size Specific Dose Estimates (SSDE)⁴⁰. SSDE associates the values of CTDI_{vol} according to patient’s size.

Efforts have been made to develop a methodology that allows direct estimation of organ doses from patients undergoing CT exams. For a more precise dose estimation, such methodologies must take into account patient size and anatomic characteristics subjected to the CT scan. It has been shown that dose estimation may be derived from new proposed size metrics, such as the effective diameter and water-equivalent diameter^{108,109}.

Mueller J. W. et al¹¹⁰ presented a method of measuring rectal radiation dose in vivo during CT colonography and compared the accuracy of SSDE relative to in vivo estimations. The dose from 10 volunteers were estimated with TLD capsules attached to rectal catheters. SSDE values were determined based on patients’ effective diameter and CTDI_{vol} value displayed by the scanner. The results imply that the rectal radiation dose absorbed by patients are closely related to SSDE values: SSDE accurately predicted the radiation dose delivered to the rectum within 10%

absolute error in eight of 10 patients. Analyzing the results from those eight patients suggests a linear dependency trend (Figure 35, red curve).

The same analysis may be performed for the results obtained for lung absorbed doses due to thorax and total body protocols from the present study (Figure 35, blue curve). To better estimate the total absorbed dose received by patients due to a clinical CT procedure, the contribution of the double SPR was added to the thorax protocols with constant tube current (“Standard”, “Low Dose” and “Ultra Low Dose”), once they were acquired without performing SPR.

A linear dependency trend may also be observed for the lung doses and the values of SSDE. Despite the same behavior of both curves, it is important to notice the difference in SSDE calculations: Mueller et al¹¹⁰ calculated the SSDE based on the effective diameter of different-sized patients and same CTDI_{vol} value displayed by the scanner, as all the patients were submitted to the same protocol; SSDE values from the present work were determined for one single effective diameter (RANDO phantom's) and CTDI_{vol} values correspondent to the six protocols considered.

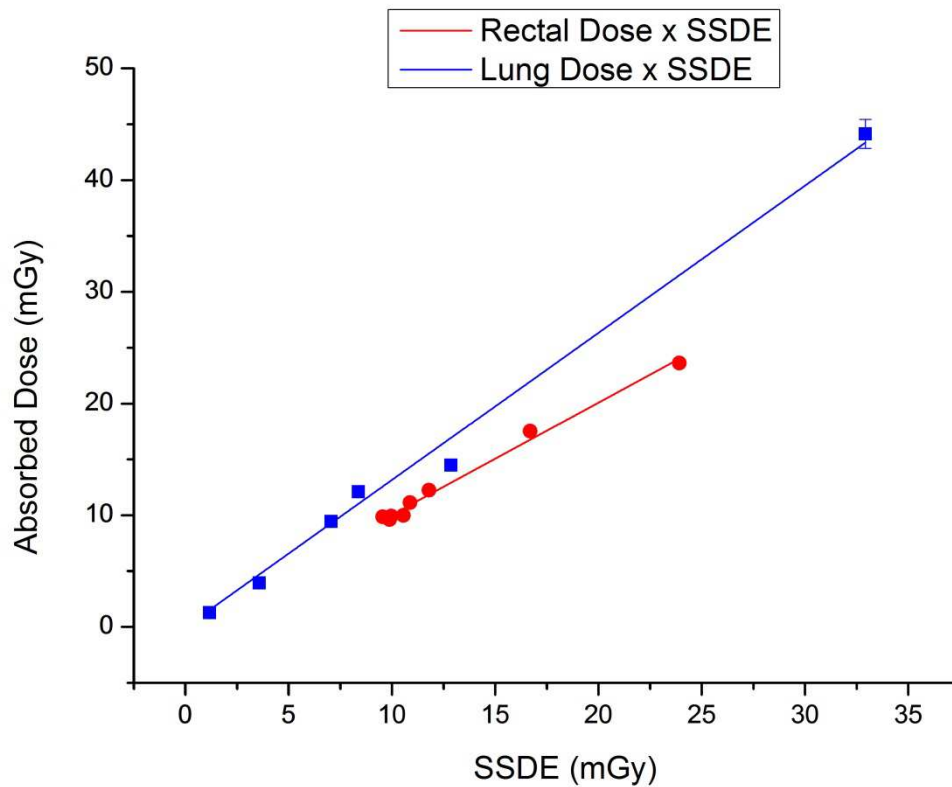


Figure 35 - Linear fit performed with the results for rectal doses obtained from Mueller et al¹¹⁰ (red curve), and from the present study for lung doses (blue curve). The curves suggest a linear dependence between both organ doses estimated with TLDs, and SSDE estimated with patients' effective diameter and CTDI_{vol} value displayed by the scanner. Linear fit was performed using the plotting and data analysis software Origin® (OriginLab Co., MA, USA). Fitting parameters are 1.004(12) for angular coefficient, $R^2 = 0.999$ (for rectal doses); and 1.331(37) for angular coefficient, $R^2 = 0.996$ (for lung doses). Linear coefficient was set zero in both cases. The estimated uncertainties for lung dose values are within 3 %.

Analysis of Figure 35 may suggest that organ absorbed doses are linearly related to SSDE values, with the angular coefficient being organ-specific. To verify this assumption further investigations on organ doses shall be performed: different organs must be considered, different protocols and different anthropomorphic phantoms. If this assumption is proven to be true, then estimation of organ absorbed doses could, in principle, be performed quickly and directly prior to a CT examination.

5. CONCLUSIONS

With the increasing application of computed tomography as a diagnostic technique, the concern with patient's absorbed doses has gained attention from the international scientific and medical communities. Many researches defend that the best indicator of the patient's radiation dose delivered by CT is based on organ absorbed doses, therefore different methodologies have been developed to establish the estimation of organ dose in routine dosimetry.

The present work describes a methodology to experimentally estimate lung absorbed doses to patients submitted to seven different CT scan protocols, by means of thermoluminescent dosimeters and anthropomorphic adult RANDO phantom. Seven different CT scan protocols were analyzed, based especially on their relevance regarding frequency of performance and promising possibility for dose reduction: one total body protocol, one double SPR, three thorax protocols with constant tube current and two thorax protocols with tube current modulation. Two from those are new protocols aiming dose optimization, proposed in a partnership with an experienced team of radiologists. The dose reduction achieved with the "Low Dose" and "Ultra Low Dose" protocols is remarkable, being more significant than for protocols with tube current modulation.

The dose estimates obtained with the proposed methodology are in good agreement with similar studies published in literature and also with estimates performed with different methodologies, when available. The proposed methodology proved to be efficient for lung doses and for thorax protocols, but its applicability to different situations must be evaluated:

- A comprehensive study involving different organs from the adult anthropomorphic RANDO phantom could validate the methodology for estimating absorbed doses for a variety of organs of interest;
- Analysis of different CT protocols, together with an investigation regarding image quality, could provide different possibilities for dose optimization;
- Studies with pediatric anthropomorphic phantoms are already being performed, in order to extend the methodology to dose estimates of infant patients submitted to CT exams;

- Dose estimates based on the proposed methodology could be validated to different dosimeter types, such as optically stimulated luminescence dosimeters (OSLDs).

Direct estimation of patient's absorbed dose is a crucial step towards dose optimization, and developing a methodology that relates organ doses with well established dosimetric quantities seems to be a good path to follow. Moreover, a better estimation could be obtained if new proposed metrics, considering patient's characteristics, are employed.

The relationship between lung absorbed doses and SSDE were analyzed for all the protocols in the present study, except for the double SPR irradiation. The results suggest a linear dependence tendency between experimentally estimated lung absorbed doses and SSDE values. Results obtained from literature comparing in vivo rectal absorbed doses and SSDE have exhibited the same behavior. Such analyses suggest a linear behavior between organ absorbed doses and SSDE values, with organ-specific linear coefficients. Further investigations in organ doses are necessary to validate or negate this assumption: a comprehensive study shall be performed involving different organs, different CT clinical protocols and different anthropomorphic phantoms. If this hypothesis is proven to be true, a major advance in patient's dosimetry could be achieved, as it would be possible to estimate organ doses prior to CT examinations.

REFERENCES

- 1 INTERNATIONAL COMMISSION ON RADIOLOGICAL PROTECTION, ICRP. **Managing Patient Dose in Computed Tomography**. Ann. ICRP 30 (4), 2000. (ICRP publication 87).
- 2 BUSHBERG, J. T.; SEIBERT, J. A.; LEIDHOLDT JR., E. M.; BOONE, J. M. **The Essential Physics of Medical Imaging**. 3rd edition. Philadelphia: Lippincott Williams & Wilkins, 2012.
- 3 BUZUG, T. M. **Computed Tomography: From Photon Statistic to Modern Cone-Beam CT**. Berlin: Springer, 2008.
- 4 KALENDER, W. A. **Computed Tomography: Fundamentals, System Technology, Image Quality, Applications**. 3rd edition. Erlanger: Publics Publishing, 2011.
- 5 BUNGE, R. E.; HERMAN, C. L. Usage of diagnostic imaging procedures: a nationwide hospital study. **Radiology**, v. 163, n. 2, p. 569-573, 1987.
- 6 METTLER, F. A. et al. Use of radiology in U.S. general short-term hospitals: 1980–1990. **Radiology**, v. 189, n. 2, p. 377-380, 1993.
- 7 INTERNATIONAL MARKETING VENTURES. **2014 CT Market Outlook Report**. International Marketing Ventures, Des Plaines: International Marketing Ventures, 2015. Available at: <<http://www.imvinfo.com/>> in: 10 August 2015.
- 8 NICKOLOFF, E. L.; ALDERSON, P. O. Radiation Exposure to Patients from CT: Reality, Public Perception, and Policy. **Am J Roentgenol.**, v. 177, n. 2, p. 285-287, 2001.
- 9 METTLER, F. A. et al. Radiologic and Nuclear Medicine Studies in the United States and Worldwide: Frequency, Radiation Dose, and Comparison with Other Radiation Sources – 1950-2007. **Radiology**, v. 253, n. 2, p. 520-531, 2009.
- 10 BUNDESAMT FÜR STRAHLENSCHUTZ, BFS. **Jahresbericht 1999**. SALZGITTER, 2000. Available at: <https://doris.bfs.de/jspui/bitstream/urn:nbn:de:0221-2015031112672/1/BfS_Jahresbericht_1999.pdf> in: 11 August 2015.
- 11 BUNDESAMT FÜR STRAHLENSCHUTZ, BFS. **Jahresbericht 2008**. SALZGITTER, 2009. Available at: <https://doris.bfs.de/jspui/bitstream/urn:nbn:de:0221-201004291811/1/BfS%20_2009_JB2008.pdf> in: 11 August 2015.

-
- 12 GUDJÓNSDÓTTIR, J.; WEEN, B.; OLSEN, D. R. Optimal Use of AEC in CT: A Literature Review. **Radiol Technol.**, v. 81, n. 4, p. 309-317, 2010.
- 13 BRASIL. MINISTÉRIO DA SAÚDE. **DATASUS**: Informações de Saúde (TABNET). Available at: <<http://www2.datasus.gov.br/DATASUS/index.php?area=02>>. In: 15 December 2015.
- 14 TAMM, E. P. et al. Quality Initiatives: CT Radiation Dose Reduction: How to Implement Change without Sacrificing Diagnostic Quality. **RadioGraphics**, v. 31, p. 1823-1832, 2011.
- 15 KALENDER, W. A. Dose in x-ray computed tomography. **Physics in Medicine and Biology**, v. 59, n. 3, p. 129-150, 2014.
- 16 BRENNER D. J.; HALL, E. J. Computed tomography: An increasing source of radiation exposure. **The New English Journal of Medicine**, v. 357, n. 22, p. 2277-2284, 2007.
- 17 BOONE J. M. et al. Radiation exposure from CT scans: how to close out knowledge gaps, monitor and safeguard exposure – Proceedings and recommendations of the dose summit, sponsored by NIBIB, February 24-25, 2011. **Radiology**, v. 265, n. 2, p. 544-554, 2012.
- 18 GRIGLOCK, T. M. et al. Determining Organ Doses from CT with Direct Measurements in Postmortem Subjects: Part 1 – Methodology and validation. **Radiology**, v. 277, n. 2, p. 463-470, 2015.
- 19 WEBB, S. **From the watching of shadows**: the origins of radiological tomography. New York: IOP Publishing, 1990.
- 20 ULZHEIMER, S.; FLOHR, T. Multislice CT: Current Technology and Future Developments. In: REISER, M. F.; BECKER, C. R.; NIKOLAOU, K.; GLAZER, G. **Multislice CT**. Berlin: Springer, 2009, p. 3-23.
- 21 PLATTEN, D. **Multi-slice helical CT physics and technology**. London: ImPACT, 2003. Available at: <<http://www.impactscan.org/slides/eanm2002/sld001.htm>>. In: 15 August 2015.
- 22 AMIS, E. S. CT Radiation Dose: Trending in the Right Direction. **Radiology**, v. 261, n. 1, p. 5-8, 2011.
- 23 BEISTER, M.; KOLDITZ, D.; KALENDER, W. A. Iterative reconstruction techniques in X-ray CT. **Physica Medica**, v. 28, p. 94-108, 2012.

-
- 24 MAYO-SMITH, W. W. et al. How I do it: Managing Radiation Dose in CT. **Radiology**, v. 273, n. 3, p. 657-672.
- 25 MCCOLLOUGH, C. H.; BRUESEWITZ, M. R.; KOFLER JR., J.M. CT Dose reduction and dose management tools: overview of available options. **RadioGraphics**, v. 26, n. 2, p. 503-512, 2006.
- 26 ALLIANCE FOR RADIATION SAFETY IN PEDIATRIC IMAGING. **Image Gently Development of Pediatric CT Protocols**. Available at: <<http://www.imagegently.org/Portals/6/Procedures/IG%20CT%20Protocols%20111714.pdf>>. In: .28 October 2015.
- 27 SCHARDT, P. et al. New x-ray tube performance in computed tomography by introducing the rotating envelope technology. **Medical Physics**, v. 31, n. 9, p. 2699-2706, 2004.
- 28 SIEMENS HEALTHCARE GmbH. **SOMATOM Sessions Online**: Answers for life in Computed Tomography - STRATON X-ray tube. Available at: <https://health.siemens.com/ct_applications/somatomsessions/index.php/straton-x-ray-tube/>. In: 30 October 2015.
- 29 FOSBINDER, R.; ORTH, D. **Essentials of Radiologic Science**. Philadelphia: Lippincott Williams & Wilkins, 2011.
- 30 IMPACT. **CT Scanner Acceptance Testing**. Information Leaflet no.1, version 1.02. London: ImPACT, 2001. Available at: <<http://www.impactscan.org/download/acceptancetesting.pdf>>. In: 20 August 2015.
- 31 BRASIL. MINISTÉRIO DA SAÚDE. **Ambiente digital didático para técnico em radiologia**. Available at: <<http://rle.dainf.ct.utfpr.edu.br/hipermidia/>>. In: 31 October 2015.
- 32 DEANS, S. R. **The Radon Transform and Some of Its Applications**. New York: Dover Publications, 2007.
- 33 DENDY, P.P.; HEATON, B. **Physics for Diagnostic Radiology**. 3rd edition. London: CRC Press, 2011.
- 34 FELDKAMP, L. A.; DAVIS, L. C.; KRESS J. W. Practical cone-beam algorithm. **Journal of optical society of america** v. 1, n. 6, p. 612-619, 1984.
- 35 COSTA, P. R.; ARAÚJO, E. C. A. Application of the FDK algorithm for multi-slice tomographic image reconstruction. **Revista Brasileira de Engenharia Biomédica**, v.26, n. 2, p. 105-120, 2010.

-
- 36 SHOPE T. B; GAGNE, R. M.; JOHNSON G. C. A method for describing the doses delivered by transmission x-ray computed tomography. **Medical Physics**, v. 8, n. 4, p. 488-495, 1981.
- 37 MCCOLLOUGH, C. H. et al. CT dose index and patient dose: they are not the same thing. **Radiology**, v. 259, n. 2, p. 311-316, 2011.
- 38 AMERICAN ASSOCIATION OF PHYSICISTS IN MEDICINE, AAPM. **The measurement, reporting, and management of radiation dose in CT**. AAPM Task Group 23, 2008. (AAPM Report No. 96).
- 39 COSTA, P. R. Computer Tomography Phantom Applications. In: DEWERD, L. A.; KISSICK, M. **The Phantoms of Medical and Health Physics: Devices for Research and Development**. New York: Springer, 2014, p. 123-142.
- 40 AMERICAN ASSOCIATION OF PHYSICISTS IN MEDICINE, AAPM. **Size-specific dose estimates (SSDE) in pediatric and adult body CT examinations**. AAPM Task Group 204, 2011. (AAPM Report No. 204).
- 41 DIXON, R. L. A new look at CT dose measurement: Beyond CTDI. **Medical Physics**, v. 30, n. 6, p. 1272-1280, 2003.
- 42 BOONE, J. M. The trouble with CTDI100. **Medical Physics**, v. 34, n. 4, 1364-1371, 2007.
- 43 AMERICAN ASSOCIATION OF PHYSICISTS IN MEDICINE, AAPM. **Comprehensive Methodology for the Evaluation of Radiation Dose in X-ray Computed Tomography**. AAPM Task Group 111: The Future of CT Dosimetry, 2010. (AAPM Report No. 111).
- 44 DIXON, R. L.; BOONE, J. M.; KRAFT, R. A. Dose equations for shift-variant CT acquisition modes using variable pitch, tube current, and aperture, and the meaning of their associated CTDI(VOL). **Medical Physics**, v. 41, n. 11, p. 111906/1 – 111906/11, 2014.
- 45 LI, X.; ZHANG, D.; LIU, B. Radiation dose calculations for CT scans with tube current modulation using the approach to equilibrium function. **Medical Physics**, v. 41, n. 11, p. 111910/1-111910/15, 2014.
- 46 BRENNER D. J.; HALL, E. J. Computed tomography: An increasing source of radiation exposure. **The New English Journal of Medicine**, v. 357, n. 22, p. 2277-2284, 2007.
- 47 BOONE J. M. et al. Radiation exposure from CT scans: how to close out knowledge gaps, monitor and safeguard exposure – Proceedings and

-
- recommendations of the dose summit, sponsored by NIBIB, February 24-25, 2011. **Radiology**, v. 265, n. 2, p. 544-554, 2012.
- 48 GRIGLOCK, T. M. et al. Determining Organ Doses from CT with Direct Measurements in Postmortem Subjects: Part 1 – Methodology and validation. **Radiology**, v. 277, n. 2, p. 463-470, 2015.
- 49 TURNER, A. C., et al. The feasibility of a scanner-independent technique to estimate organ dose from MDCT scans: Using CTDIvol to account for differences between scanners. **Medical Physics**, v. 37, n. 4, p. 1816-1825, 2010.
- 50 Castellano, I. A. **Personal Communication**. 22 October 2015.
- 51 LI, X. et al. Patient-specific radiation dose and cancer risk estimation in CT: Part I. Development and validation of a Monte Carlo Program. **Medical Physics**, v. 38, n. 1, p. 397-407, 2011.
- 52 LI, X. et al. Patient-specific radiation dose and cancer risk estimation in CT: Part II. Application to patients. **Medical Physics**, v. 38, n. 1, p. 408-419, 2011.
- 53 LEE, C. et al. Organ doses for reference adult male and female undergoing computed tomography estimated by Monte Carlo simulations. **Medical Physics**, v. 38, n. 3, p. 1196-1206, 2011.
- 54 PENG, G. et al. Organ dose evaluation for multi-slice spiral CT scans based on China Sichuan chest anthropomorphic phantom measurements. **Radiation Protection Dosimetry**, v. 150, n. 3, p. 292-297, 2012.
- 55 HUDA, W. et al. Organ doses to adult patients for chest CT. **Medical Physics**, v. 37, n. 2, p. 842-847, 2010.
- 56 BANKIER, A. A.; TACK, D. Dose reduction strategies for thoracic multidetector computed tomography. background, current issues, and recommendations. **Journal of Thoracic Imaging**, v. 25, n. 4, p. 278-288, 2010.
- 57 KHAWAJA, R. D. A.. et al. Ultra-low dose abdominal MDCT: using a knowledge-based iterative Model Reconstruction technique for substantial dose reduction in a prospective clinical study. **European Journal of Radiology**, v. 84, n. 1, p. 2-10, 2015.
- 58 POLETTI, P. A. et al. Low-dose versus standard-dose CT protocol in patients with clinically suspected renal colic. **American Journal of Roentgenology**, v. 188, n. 4, p. 927-933, 2007.

-
- 59 NAGATANI, Y. et al. Lung nodule detection performance in five observers on computer tomography (CT) with adaptive iterative dose reduction using three-dimensional processing (AIDR 3D) in a Japanese multicenter study: Comparison between ultra-low-dose CT and low-dose CT by receiver-operating characteristic analysis. **European Journal of Radiology**, v. 84, n. 4, p. 1401-1412, 2015.
- 60 WIDMANN, G. et al. Ultralow-dose computed tomography imaging for surgery of midfacial and orbital fractures using ASIR and MBIR. **International Journal of Oral and Maxillofacial Surgery**, v. 44, n. 4, p. 441-446, 2015.
- 61 MULKENS, T. H. et al. Use of an automatic exposure control mechanism for dose optimization in multi-detector row CT examinations: Clinical evaluation. **Radiology**, v. 237, n. 1, p. 213-223, 2005.
- 62 VAN STRATEN, M. et al. The effect of angular and longitudinal tube current modulation on the estimation of organ and effective doses in x-ray computed tomography. **Medical Physics**, v. 36, n. 11, p. 4881-4889, 2009.
- 63 PADAPAKIS, A. E.; PERISINAKIS, K; DAMILAKIS, J. Automatic exposure control in pediatric and adult multidetector CT examinations: A phantom study on dose reduction and image quality. **Medical Physics**, v. 35, n. 10, p. 4567-4576, 2008.
- 64 BANKIER, A. A.; KRESSEL, H. Y. Through the Looking Glass revisited: the need for more meaning and less drama in the reporting of dose and dose reduction in CT. **Radiology**, v. 265, n. 1, p. 4-8, 2012.
- 65 GIES, M. et al. Dose reduction in CT by anatomically adapted tube current modulation. I. Simulation studies. **Medical Physics**, v. 26, n. 11, p. 2235-2247, 1999.
- 66 KALRA, M. K. et al. Computed tomography radiation dose optimization: scanning protocols and clinical applications of automatic exposure control. **Current Problems in Diagnostic Radiology**, v. 34, n. 5, p. 171-181, 2005.
- 67 REINA, T. R. **Evaluation of automatic exposure control systems in computed tomography: avaliação de sistemas de controle automático de exposição em tomografia computadorizada**. (Dissertação de Mestrado). Universidade de São Paulo, Instituto de Física, Departamento de Física Nuclear, São Paulo, 2014.
- 68 MEDICINE AND HEALTH CARE PRODUCTS REGULATORY AGENCY, MHRA. **CT scanner automatic exposure control systems**. London: MHRA, 2005. (MHRA Report 05016).

-
- 69 MCKEEVER, S. W. S. **Thermoluminescence of Solids** – Cambridge Solid State Science Series. Cambridge: Cambridge University Press, 1985.
- 70 YUKIHARA, E. G.; MCKEEVER, S. W. S. **Optically Stimulated Luminescence: Fundamentals and Applications**. Chichester: Wiley, 2011.
- 71 WINSLOW, J. F. et al. Construction of anthropomorphic phantoms for use in dosimetry studies. **Journal of Applied Clinical Medical Physics**, v. 10, n. 3, p. 2986, 2009.
- 72 INTERNATIONAL COMMISSION ON RADIOLOGICAL PROTECTION, ICRP. **Report of the task group on Reference Man**. Ann. ICRP. Oxford, p. 1-480, 1975. (ICRP Publication No. 23).
- 73 ARCHER, B. B. Dosimeter placement in the Rando phantom. *Medical Physics*, v. 4, n. 4, p. 315-318, 1977.
- 74 THE PHANTOM LABORATORY. **RAN 100 and RAN 110 datasheet brochure**. Salem, The Phantom Laboratory, 2012. Available at: <http://www.phantomlab.com/library/pdf/rando_datasheet.pdf>. In: 25 August 2015.
- 75 HUDA, W.; SANDISON, G. A. Estimation of mean organ doses in diagnostic radiology from Rando phantom measurements. **Health Physics**, v. 47, n. 3, p. 463-467, 1984.
- 76 GOLIKOV, V. Y.; NIKITIN, V. V., Estimation of the mean organ doses and the effective dose equivalent from RANDO phantom measurements. **Health Physics**, v. 56, n. 1, p. 111-115, 1989.
- 77 DTU NUTECH. **Guide to “The Risø TL/OSL Reader”** Model DA-20. Denmark: DTU-Nutech, 2014.
- 78 FURETTA, C. **Questions and Answer on Thermoluminescence (TL) and Optically Stimulated Luminescence (OSL)**. Singapore: World Scientific Publishing, 2008.
- 79 FURETTA, C. **Handbook of Thermoluminescence**. 2nd edition. Singapore: World Scientific Publishing, 2010.
- 80 OKUNO, E.; YOSHIMURA, E. M. **Física das Radiações**. 1st edition. São Paulo: Oficina de Textos, 2010.

-
- 81 NATIONAL INSTITUTE OF STANDARDS AND TECHNOLOGY, NIST. **Composition of Materials used in STAR Database.** Available at: <<http://physics.nist.gov/cgi-bin/Star/compos.pl>>. In: 25 July 2015.
- 82 INTERNATIONAL ATOMIC ENERGY AGENCY, IAEA. **Dosimetry in Diagnostic Radiology:** An international Code of Practice. Viena, 2007. (Technical Report Series No. 457).
- 83 VUOLO, J. H. **Fundamentos da Teoria de Erros.** 2nd edition. São Paulo: Blucher, 1996.
- 84 GONZAGA, N. B. et al. Organ equivalent doses of patients undergoing chest computed tomography: Measurements with TL dosimeters in an anthropomorphic phantom. **Applied Radiation and Isotopes**, v. 83, p. 242-244, 2014.
- 85 NATIONAL INSTITUTE OF STANDARDS AND TECHNOLOGY, NIST. **XCOM:** Photon Cross Sections Database. Available at: <<http://physics.nist.gov/PhysRefData/Xcom/html/xcom1.html>>. In: 15 April 2015.
- 86 NATIONAL INSTITUTE OF STANDARDS AND TECHNOLOGY, NIST. **XCOM:** X-Ray Mass Attenuation Coefficient. Available at: <<http://physics.nist.gov/PhysRefData/XrayMassCoef/tab2.html>>. In: 12 April 2015.
- 87 INTERNATIONAL COMMISSION ON RADIATION UNITS AND MEASUREMENTS, ICRU. **Tissue Substitutes in Radiation Dosimetry and Measurement.** Bethesda, 1989. (ICRU Report No. 44).
- 88 Fuchs's Radiographic exposure, processing and quality control. 6th edition. Quinn B. Carroll. Charles C NThomas Publisher LTD. Springfield Illinois, 1998.
- 89 BRASIL. MINISTÉRIO DA SAÚDE. SECRETARIA DE ATENÇÃO À SAÚDE. **A Situação do Câncer no Brasil.** Rio de Janeiro: Instituto Nacional do Câncer, INCA, 2006. 117 p. Available at: <<http://www.inca.gov.br/situacao/>>. In: 25 October 2015.
- 90 WORLD HEALTH ORGANIZATION. **IARC Cancer Base Series and Related Publications.** Lyon: International Agency for Research on Cancer (IARC), 2014. Available at: <<http://www.iarc.fr/en/publications/eresources/cancerbases/>>. In: 20 October 2015.
- 91 BOSTANI, M. et al. Accuracy of Monte Carlo simulations compared to in-vivo MDCT dosimetry. **Medical Physics**, v. 42, n. 2, p. 1080-1086, 2015.

-
- 92 DEMARCO, J. J. et al. A Monte Carlo based method to estimate radiation dose from multidetector CT (MDCT): cylindrical and anthropomorphic phantoms. **Physics in Medicine and Biology**, v. 50, n. 17, p. 3989–4004, 2005.
- 93 KHATONABADI, M. et al. A comparison of methods to estimate organ doses in CT when utilizing approximations to the tube current modulation function. **Medical Physics**, v. 39, n. 8, p. 5212-5228, 2012.
- 94 MINI, R. L. et al. Radiation exposure of patients who undergo CT of the trunk. **Radiology**, v. 195, n. 2, p. 557-562, 1995.
- 95 THE NATIONAL LUNG SCREENING TRIAL RESEARCH TEAM, NLST. Reduced lung-cancer mortality with low-dose computed tomography screening. **The New England Journal of Medicine**, v. 365, p. 395-409, 2011
- 96 METTLER, F. A. et al. Effective doses in radiology and diagnostic nuclear medicine: a catalog. **Radiology**, v. 248, n. 1, p. 254-263, 2008.
- 97 FREITAS, M. B. **Doses Absorvidas pelos Pacientes submetidos a Radiografias Torácicas em Hospitais do Município de São Paulo**. (Dissertação de Mestrado). Universidade de São Paulo, Instituto de Física, Departamento de Física Nuclear, São Paulo, 2000.
- 98 KAY, F. U. Personal Communication. 14 October 2015.
- 99 SABARUDIN, A. et al. Radiation dose reduction in thoracic and abdomen-pelvic CT using tube current modulation: a phantom study. **Journal of Applied Clinical Medical Physics**, v. 16, n. 1, p. 319-28, 2015.
- 100 LONG, D. J. et al. Monte Carlo simulations of adult and pediatric computed tomography exams: Validation studies of organ doses with physical phantoms. **Medical Physics**, v. 40, n. 1, p. 013901/1-013901/10, 2013.
- 101 ANGEL E. et al. Radiation dose to the fetus for pregnant patients undergoing multidetector CT imaging: Monte Carlo simulations estimating fetal dose for a range of gestational age and patient size. **Radiology**, v. 249, n.1, p. 220-227, 2008..
- 102 DEMARCO, J. J. et al. Estimating radiation doses from multidetector CT using Monte Carlo simulations: effects of different size voxelized patient models on magnitudes of organ and effective dose. **Physics in Medicine and Biology**, v. 52, n. 9, p. 2583-2597, 2007.
- 103 STAMM, G.; NAGEL, H. D. CTExpo: A novel program for dose evaluation in CT. **Röfo**, v. 174, n. 2, p. 1570-1576, 2002.

-
- 104 LEWIS, M. CTDOsimetry: ImPACT spreadsheet for calculating organ and effective doses from CT exams. London: ImPACT, 2004. Available at: <<http://www.impactscan.org/slides/ctdosimetrydenmark/>>. In: 15 October 2015.
- 105 JONES, D.G.; SHRIMPTON, P.C. **Survey of the practice in the UK. III. Normalized organ doses calculated using Monte Carlo techniques.** Chilton: National Radiological Protection Board (NRPB R-250), 1991.
- 106 ZANKL, M.; PANZER, W.; DREXLER, G. **The Calculation of Dose from External Photon Exposures Using Reference Human Phantoms and Monte Carlo Methods, Part VI: Organ Doses From Computed Tomographic Examinations.** Neuherberg: Gesellschaft für Strahlen und Umweltforschung mbH, 1991.
- 107 ZANKL, M.; PANZER, W.; DREXLER, G. **Tomographic Anthropomorphic Models. Part II: Organ Doses From Computed Tomographic Examinations in Paediatric Radiology.** Neuherberg: Gesellschaft für Strahlen und Umweltforschung mbH, 1993.
- 108 AMERICAN ASSOCIATION OF PHYSICISTS IN MEDICINE, AAPM. **Use of water equivalent diameter for calculating patient size and size-specific dose estimates (SSDE) in CT.** AAPM Task Group 220, 2014. (AAPM Report No. 220).
- 109 BOSTANI, M. et al. Attenuation-based size metrics for estimating organ dose to patients undergoing tube current modulated CT exams. **Medical Physics**, v. 42, n. 2, p. 958-968, 2015.
- 110 MUELLER, J. W. et al. In vivo CT dosimetry during CT colonography. **American Journal of Roentgenology**, v. 202, n. 4, p. 703-710, 2014.

ANNEXX A – Conversion factors for SSDE determination.

To calculate the Size Specific Dose Estimates, conversion factors must be applied to the $CTDI_{vol}$ value displayed by the scanner console. The size of the dosimetric PMMA phantom have to be correctly considered. Table A1 gives the correction factors for SSDE for $CTDI_{vol}$ based on the use of the body 32-cm diameter PMMA phantom, as a function of the effective diameter³⁶. Table A2 gives the correction factors for SSDE for $CTDI_{vol}$ based on the use of the head 16-cm diameter PMMA phantom, as a function of the effective diameter³⁶.

Table A1 - Conversion factors for SSDE, as a function of effective diameter for $CTDI_{vol}$ based on the use of 32-cm diameter body dosimetry PMMA phantom³⁶.

Effective Diameter (cm)	Conversion Factor	Effective Diameter (cm)	Conversion Factor
8	2.76	27	1.37
9	2.66	28	1.32
10	2.57	29	1.28
11	2.47	30	1.23
12	2.38	31	1.19
13	2.30	32	1.14
14	2.22	33	1.10
15	2.14	34	1.06
16	2.06	35	1.02
17	1.98	36	0.99
18	1.91	37	0.95
19	1.84	38	0.92
20	1.78	39	0.88
21	1.71	40	0.85
22	1.65	41	0.82
23	1.59	42	0.79
24	1.53	43	0.76
25	1.48	44	0.74
26	1.43	45	0.71

Table A2 - Conversion factors for SSDE, as a function of effective diameter for CTDIvol based on the use of 16-cm diameter body dosimetry PMMA phantom³⁶.

Effective Diameter (cm)	Conversion Factor	Effective Diameter (cm)	Conversion Factor
6	1.49	31	0.56
7	1.43	32	0.54
8	1.38	33	0.52
9	1.32	34	0.50
10	1.27	35	0.48
11	1.22	36	0.47
12	1.18	37	0.45
13	1.13	38	0.43
14	1.09	39	0.41
15	1.05	40	0.40
16	1.01	41	0.38
17	0.97	42	0.37
18	0.93	43	0.35
19	0.90	44	0.34
20	0.86	45	0.33
21	0.83	46	0.32
22	0.80	47	0.30
23	0.77	48	0.29
24	0.74	49	0.28
25	0.71	50	0.27
26	0.69	51	0.26
27	0.66	52	0.25
28	0.63	53	0.24
29	0.61	54	0.23
30	0.59	55	0.22

ANNEX B – Uncertainty estimation

The uncertainties considered to calculate the overall uncertainties of lung absorbed dose estimates are summarized in Figure 33. σ_{M_Q} is the uncertainty in the ionization chamber reading (in Coulombs) for a X-ray beam quality Q, $\sigma_{N_{k,Q_0}}$ is the uncertainty of the calibration coefficient given by the IC calibration report, $\sigma_{k_{Q,Q_0}}$ refers to the correction factor for a radiation beam quality Q regarding the calibration beam quality Q_0 , $\sigma_{k_{TP}}$ is due to the correction factor for temperature and pressure, $\sigma_{K_{Air}}$ is the composed uncertainty for air kerma values, σ_n is the is the uncertainty of the TL values from TLDs, σ_a refers to the calibration curve of TL values and air kerma and finally $\sigma_{D_{Lungs}}$ is the overall uncertainty to the lung dose estimates. Confidence level considered is 68.3 %.

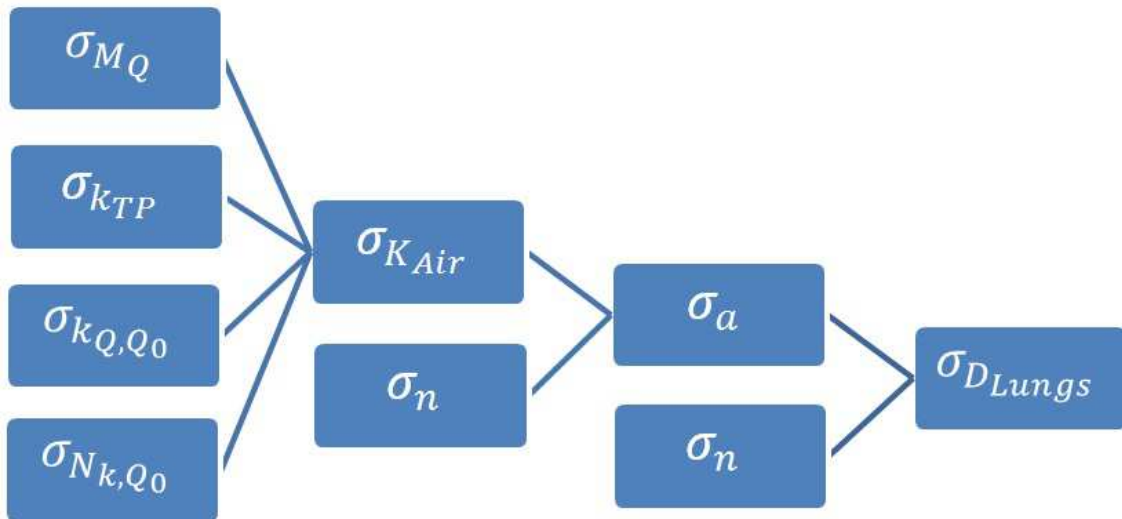


Figure B1 – Scheme illustrating all the uncertainties used to the overall uncertainty for lung absorbed dose estimation.